SLAC-R-512
UC-414

Generation and Characterization of Superradiant Undulator Radiation*

David Bocek

Stanford Linear Accelerator Center
Stanford University
Stanford, CA 94309

SLAC-Report-512
June 1997

Prepared for the Department of Energy
under contract number DE-AC03-76SF00515

Printed in the United States of America. Available from the National Technical Information Service, U.S. Department of Commerce, 5285 Port Royal Road, Springfield, VA 22161.

---

*Ph.D. thesis, Stanford University, Stanford, CA 94309.

Abstract

High-power, pulsed, coherent, far-infrared (FIR) radiation has many scientific applications [1], such as pump-probe studies of surfaces, liquids, and solids, studies of high-T_c superconductors, biophysics, plasma diagnostics, and excitation of Rydberg atoms. Few sources of such FIR radiation currently exist. Superradiant undulator radiation produced at the SUNSHINE (**S**tanford **UN**iversity **SH**ort **IN**tense **E**lectron-source) is such a FIR source.

First proposed in the mm-wave spectral range by Motz [2], superradiant undulator radiation has been realized in the 45 μm to 300 μm spectral range by using sub-picosecond electron bunches [3] produced by the SUNSHINE facility. The experimental setup and measurements of this FIR radiation are reported in this thesis.

In addition to being a useful FIR source, the superradiant undulator radiation produced at SUNSHINE is an object of research in itself. Measured superlinear growth of the radiated energy along the undulator demonstrates the self-amplification of radiation by the electron bunch. This superlinear growth is seen at 47 μm to 70 μm wavelengths. These wavelengths are an order of magnitude shorter than in previous self-amplification demonstrations [4,5].

Acknowledgements

Many people have helped me with this thesis work. I am grateful to all of them. I thank my thesis advisor Prof. Helmut Wiedemann for suggestions and guidance in this project, and for creation of a stimulating environment for a wide range of technical work at SUNSHINE. I am grateful to Prof. Todd I. Smith and Prof. Herman Winick for their efforts in reading and correcting this thesis.

This project would not have been possible without use of the undulator and other components from the Stanford Synchrotron Radiation Laboratory as authorized by Prof. Arthur Bienenstock. Prof. Richard Pantell contributed rf equipment and over a year of uninterrupted beam time. David Gough, Jim Sebek, and Ramona Theobald of SSRL gave assistance with electronics, and Jim Weaver and Harold Morales fixed the rf gun after the cathode burnt out. The Hansen Experimental Physics Laboratory administration and staff provided infrastructure — electricity, water, and Internet access.

My colleagues Pamela H. Kung and Hung-chi Lihn did much of the initial work upon which this project was based, as did Michael Borland. Michael Hernandez, Jim Sebek, and Chitrlada Settakorn provided help and constructive suggestions. William Lavender contributed his code to calculate the undulator radiation spectrum and Eric Crosson provided access to the HITRAN atmospheric absorption database.

Finally, and most importantly, I thank my wife Renee Shakerin for her encouragement, patience, and support.

Contents

List of Tables

List of Figures

Chapter 1

Introduction

This thesis presents an experimental investigation of the superradiant FIR (far-infrared) radiation generated by passing a relativistic electron beam through a magnetic undulator. By "superradiant" it is meant that the radiation is due to the high degree of phase coherence between the radiating electrons [6, page 548]. The superradiant emission is both spatially and temporally coherent, and its intensity is proportional to the square of the number of radiating electrons. In itself, this radiation is of value as a tool for physics, biology, and chemistry, and in the future the SUNSHINE (**S**tanford **U**niversity **SH**ort **IN**tense **E**lectron source) facility, where this work was done, is intended to be offered to the scientific community as a light source. Therefore this thesis (specifically Chapter 5) describes the measured energy spectral density, spatial distribution, polarization, and time structure of the radiation so that the potential user will understand the capabilities of the SUNSHINE facility.

Additionally this experiment observes gain in the radiated power as the electron beam traverses the undulator. This process is often referred to as SASE (Self-Amplified Spontaneous Emission), and is crucial to the development of X-ray FELs (Free-Electron Lasers) which depend on such a mechanism to achieve lasing. Self-amplification has been seen previously in mm-waves [4] down to 600 μm [5]. In this

	wavelength range	molecular significance
near infrared	0.7 to 3 μm	electronic transitions
mid infrared	3 to 40 μm	vibrational modes
far infrared	40 to 1000 μm	rotational modes

Table 1.1: Definition of various IR bands.

experiment self-amplification is observed for the first time at wavelengths as short as 47 μm.

The structure of this thesis follows the pattern of overview (Chapter 1), theory (Chapters 2 and 3), experimental setup (Chapter 4), measurements (Chapters 5 and 6), discussion (Chapter 7), and summary (Chapter 8). Chapters 1, 4, and 8 are self-explanatory. Chapter 2 describes the theory and computation of superradiant undulator radiation, which was the expected result of this experiment. Chapter 3 describes single-pass FEL theory, which predicts self-amplification from a sufficiently intense electron beam[1]. Chapter 5 describes measurements characterizing the FIR radiation, and may be of particular interest to potential users of the radiation. Chapter 6 describes measurements of self-amplification (gain). Finally, Chapter 7 describes the effects of the non-ideal nature of the electron beam and instrumentation.

1.1 Far Infrared Radiation

In infrared science a typical division of the electromagnetic spectrum is shown in Table 1.1. Although the division is somewhat arbitrary, the various sub-bands correspond to qualitatively different molecular processes as shown [7]. The superradiant undulator radiation at SUNSHINE is tunable from 45 μm to 300 μm, hence falls into the far-infrared (FIR) band.

---

[1] The single-pass FEL theory predicts self-amplification at the levels observed in this experiment. However since 3-dimensional effects ignored in the theory are expected to reduce the self-amplification, the low or zero-gain limit of the theory, which is the superradiance described in Chapter 2, was the expected experimental result.

1.1.1 Applications of FIR sources

There are many applications of pulsed high-power FIR such as that produced at SUNSHINE. These include, for example:

- pump-probe surface science,
- pump-probe studies of gases, liquids, and solids,
- non-linear solid state physics,
- studies of carrier dynamics of high-T_c superconductors,
- studies of modes of large bio-molecules,
- plasma diagnostics, and
- excitation of Rydberg atoms.

In fact, the 1994 free electron laser study by the National Research Council concluded that, "The scientific case for a tunable, short-pulse (picosecond) source in the far infrared is compelling..." [1].

1.1.2 Operational Facilities

High-power, pulsed FIR sources are rare; there are only a few FEL user facilities in the far-infrared range. They and their output powers are listed in Table 1.2, as are the SUNSHINE parameters, for comparison.

1.1.3 Superradiant Undulator Radiation as a FIR Source

Superradiant undulator radiation has many desirable features as a FIR source. It is temporally and spatially coherent, polarized, intense, and at SUNSHINE it is pulsed in picosecond-long bursts. Achieved parameters of the radiation are listed in Table 1.3.

facility	wavelength tunability	micropulse power	macropulse power	average power	ref
UCSB FIRFEL	63 to 338	1–6	1–6	500 @ 4	[8]
SUNSHINE	45 to 300	10–40	0.2–1.5	3–50 @ 30	
FIREFLY	19 to 65	300	0.004	400 @ 20	[9]
FELIX	5 to 110	~1000	10	500 @ 5	[10]
units	μm	kW	kW	mW @ Hz	

Table 1.2: Power output at operating far-infrared facilities.

It is useful to compare the brightness of the SUNSHINE undulator radiation with that of a 2000 K blackbody, which approximates the commonly-used Globar source. From the listed parameters, the *average* brightness of the undulator radiation at $\approx 50\ \mu$m is

$$\frac{3 \times 10^{-3}\mathrm{W}/16\%\mathrm{bandwidth}}{\pi(3 \times 10^{-3}m)^2\pi(5 \times 10^{-3}\mathrm{rad})^2} = \frac{8 \times 10^6\ [\mathrm{W}]}{[\mathrm{m}^2][\mathrm{sr}][100\%\mathrm{bandwidth}]}, \tag{1.1}$$

and at $\approx 200\ \mu$m

$$\frac{50 \times 10^{-3}\mathrm{W}/16\%\mathrm{bandwidth}}{\pi(3 \times 10^{-3}m)^2\pi(20 \times 10^{-3}\mathrm{rad})^2} = \frac{9 \times 10^6\ [\mathrm{W}]}{[\mathrm{m}^2][\mathrm{sr}][100\%\mathrm{bandwidth}]}. \tag{1.2}$$

The brightness of the 2000 K blackbody is given by the Planck distribution as [7]

$$B(\nu, T)\left(\frac{[\mathrm{W}]}{[\mathrm{m}^2][\mathrm{sr}][100\%\mathrm{bandwidth}]}\right) = \frac{2h\nu^4}{c^2}\frac{1}{e^{h\nu/kT}-1} \approx \frac{2\nu^3 kT}{c^2}, \tag{1.3}$$

which gives 1.3×10^2 [W/m^2/sr/100%bandwidth] at 50 μm (6.0 THz) and 2.1×10^0 [W/m^2/sr/100%bandwidth] at 200 μm (1.5 THz). The *average* SUNSHINE undulator radiation is thus 4–6 orders of magnitude brighter than the blackbody source, and the *peak* SUNSHINE brightness is 10–12 orders of magnitude brighter than the blackbody source.

Parameter	Value
Wavelength tunability	45 to 300 μm
Micropulse power	10–40 kW (50–200 μm)
Macropulse power	0.2–1.6 kW (50–200 μm)
Average power	3–50 mW (50–200 μm)
Angular divergence	5–20 mrad (50–200 μm)
Effective source size	3 mm $1/e^2$ radius
Polarization	80 % linear
Micropulse length	26 radiation wavelengths
Micropulse separation	350 ps
Macropulse length	0.7–1.1 μs (50–200 μm)
Macropulse repetition rate	4–30 Hz
Macropulse linewidth	12–20% FWHM

Table 1.3: Parameters of superradiant undulator radiation at SUNSHINE.

1.2 Self-Amplification

Self-amplified spontaneous emission[2] (SASE) refers to a process by which an electron beam, spontaneously radiating as it travels through an undulator magnet, can bunch itself as a result of energy modulation caused by the spontaneous emission [11]. This bunching leads to greater emission, which leads to more bunching. A signature of this process is exponential increase of the radiated power along the length of the undulator: $P = P_0 e^{N/N_g}$, where N_g is the gain length and N is distance in number of oscillation periods along the undulator.

Figure 1.1 shows measurements both of gain and no gain, and Fig. 1.2 summarizes gain length measurements at several different wavelengths. In these figures, the fit function is not a pure exponential, but instead is of the form $y(N) = m1 \times (e^{N/N_g} - 1)$. This is a modification of the exponential that goes linearly to zero as N approaches zero, as discussed in Chapter 6.

---

[2] For the purposes of this thesis, it is assumed the term "SASE" applies to self-amplification arising from either shot-noise in the electron beam distribution, or, as is the case in this experiment, from coherent structure in the electron beam distribution.

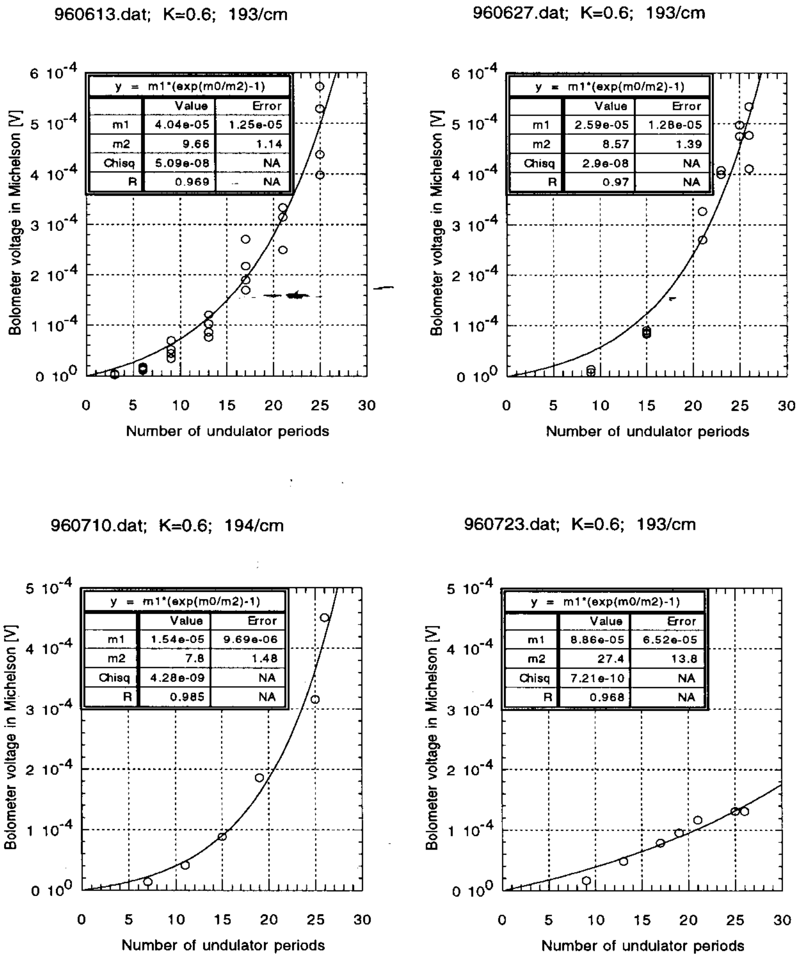

960613.dat; K=0.6; 193/cm

y = m1*(exp(m0/m2)-1)

	Value	Error
m1	4.04e-05	1.25e-05
m2	9.66	1.14
Chisq	5.09e-08	NA
R	0.969	NA

960627.dat; K=0.6; 193/cm

y = m1*(exp(m0/m2)-1)

	Value	Error
m1	2.59e-05	1.28e-05
m2	8.57	1.39
Chisq	2.9e-08	NA
R	0.97	NA

960710.dat; K=0.6; 194/cm

y = m1*(exp(m0/m2)-1)

	Value	Error
m1	1.54e-05	9.69e-06
m2	7.8	1.48
Chisq	4.28e-09	NA
R	0.985	NA

960723.dat; K=0.6; 193/cm

y = m1*(exp(m0/m2)-1)

	Value	Error
m1	8.86e-05	6.52e-05
m2	27.4	13.8
Chisq	7.21e-10	NA
R	0.968	NA

Figure 1.1: Gain measurements at short wavelengths. The dates of the measurements and wavelengths are indicated in the graph titles. The gain length in units of undulator periods is the quantity m2 in the equation tables of the graphs. The graph in the lower right-hand corner is the condition before optimization.

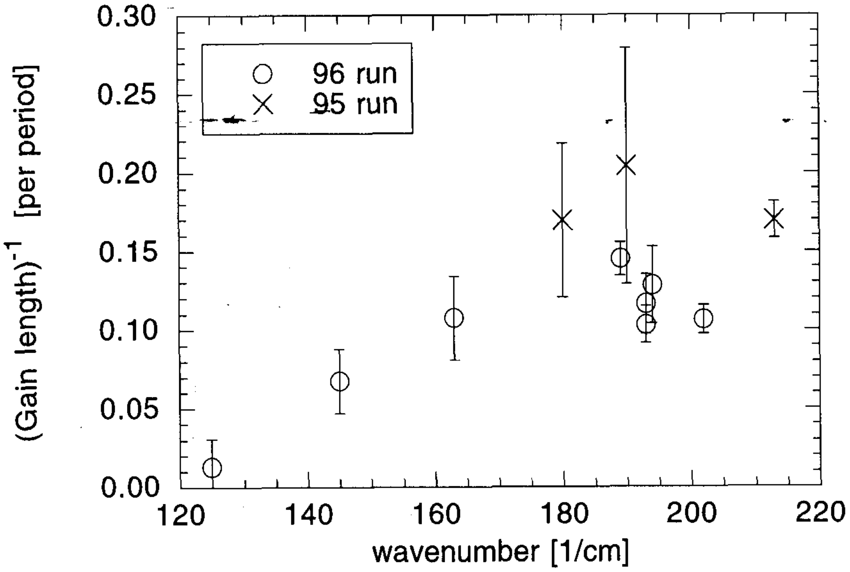

Figure 1.2: Summary of gain measurements. The fit gain coefficient, defined as the reciprocal of the gain length, is plotted as a function of the radiated wavenumber. The crosses indicate measurements from 1995, the circles are from 1996. The errors from the gain length fits give the error bars.

1.2.1 SASE experiments

Table 1.4 summarizes the parameters of the two previous SASE experiments along with the results of the SUNSHINE experiment. The SUNSHINE data are discussed in detail in Chapters 4–6 of this thesis. Some differences between the SUNSHINE experiment and the other two in the table are:

- SUNSHINE experiment is at much shorter wavelength,
- electron source is a short pulse beam (rf-bunched),
- SUNSHINE electron beam emittance is much lower,
- SUNSHINE SASE can start up from strong coherent structure of the electron beam,
- short-pulse effects may be important as the bunch length is only at most 4–5 radiation wavelengths long, and
- the radiation wavelength is 1/30 to 1/200 of the chamber radius so free-space propagation is expected rather than waveguide modes.

experiment	Livermore	MIT	SUNSHINE	units
reference	[4]	[5]	[Chapters 4–6]	
e-beam parameters:				
energy	3.6 + 0.5	2.0 + 0.5	15	MeV
Lorentz factor γ	8.0	4.9	29.4	
energy spread		0.2–0.4	0.8	%
current	450	780	53	A
pulse length	15	30	0.0006	ns
normalized emittance	4.7×10^{-3} *edge*	5.2×10^{-4}	2.0×10^{-5}	π m-rad
radius	8	3–4	1	mm
ρ-parameter	0.063	0.029	0.0092	
undulator parameters:				
geometry	planar	helical	planar	
length	3	1.5	2	m
period	9.8	3.1	7.7	cm
field	4.8	1.3	0.8	kG
K	4.4	0.5	0.6	
chamber cross-section	2.9 by 9.8	0.4 radius	1.0 radius	cm
radiation parameters:				
wavelength	8700	800	50	μm
mode	TE$_{01}$	TE$_{11}$	over-moded	
measured gain length	3.3	2.1	4 to 5	periods

Table 1.4: Comparison of SASE experiments.

Chapter 2

Theory of Superradiant Undulator Radiation

A unique feature of the SUNSHINE facility is its ability to generate sub-picosecond pulses of relativistic electrons. A typical pulse lasts about 600 fs which corresponds to 180 μm. If radiation at wavelengths much greater than 180 μm can be generated by the undulator, the electrons will radiate in phase, the field will be proportional to the number of electrons, and the power will be proportional to the square of the number of electrons [2]. This superradiance also occurs at wavelengths of the order of and less than the pulse length, although at reduced amplitude due to destructive interference between some of the radiating electrons. For wavelengths much less than the bunch length the phase between radiating electrons becomes random and the radiated power becomes proportional to the number of electrons, not the number squared. This incoherent radiation cannot be observed in this experiment because the sensitivity of the detectors used requires the large (typically $\sim 10^8$) coherent enhancement of superradiance in order to have a measurable signal.

In its simplest form the undulator is a device that makes the electron follow a sinusoidal trajectory. Although the trajectory is simple, relativistic effects make the

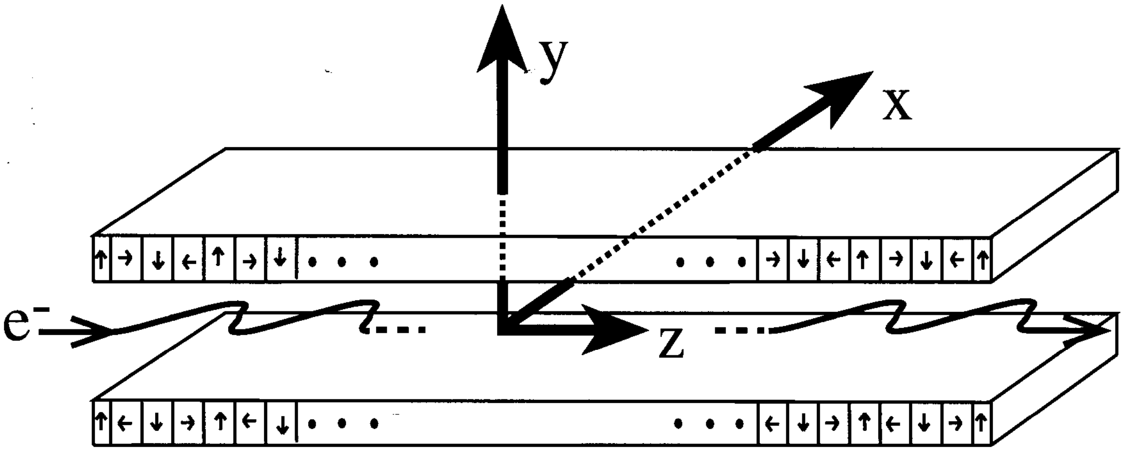

Figure 2.1: Schematic of the undulator showing the xyz coordinate system, orientation of the permanent magnets, and trajectory of the electron beam.

computation of the radiation distribution somewhat involved. In this chapter the well-known quantitative results of the theory of undulator radiation from a single electron are presented, and the effect of coherent enhancement is discussed.

2.1 Undulator Radiation Theory

As at SUNSHINE, consider a planar undulator (as shown schematically in Fig. 2.1) with magnetic field $\vec{B}$ which is entirely in the y direction and which varies sinusoidally in the z direction with period λ_0:

$$\vec{B}(z) = B_0 \cos(2\pi z/\lambda_0)\hat{\mathbf{y}}, \tag{2.1}$$

and consider an electron that enters the undulator at $z = 0$ with velocity $\vec{v} = v\hat{\mathbf{z}}$, where the notation $\hat{\mathbf{z}}$ denotes a unit vector in the z direction. If the deflection of the electron by the magnetic field is small enough so that its velocity in the z direction can be taken to be constant and equal to the speed of light c, then the trajectory followed by the electron can be found from the Lorentz force law to be sinusoidal:

$$\frac{\mathrm{d}x}{\mathrm{d}z} = \frac{K}{\gamma}\sin(2\pi z/\lambda_0) \tag{2.2}$$

where

$$K = \frac{qB_0\lambda_0}{2\pi mc} \tag{2.3}$$

is the undulator strength parameter, q is the magnitude of the electron charge, m is the electron mass, and γ = (electron energy)/mc^2 is the Lorentz factor for the electron. Here, as everywhere else in this thesis, SI units (rationalized MKSA [12] units) are used.

2.1.1 The Analytical Formula for Undulator Radiation

Once the trajectory is known, the spectral and spatial distribution of radiation from a single electron traversing a planar undulator is calculated from the Liénard-Weichert potentials [13–15, for example] with the following result [14]:

$$\frac{\mathrm{d}^2 I}{\mathrm{d}\Omega\mathrm{d}\omega} = \frac{q^2\gamma^2 N^2}{4\pi\epsilon_0 c}\sum_{n=1}^{\infty} G_n(K,\gamma\theta,\phi)H_n(K,\gamma\theta,\omega), \tag{2.4}$$

where

$$H_n(K,\gamma\theta,\omega) = \left\{\frac{\sin[N\pi(\omega/\omega_1 - n)]}{\pi N(\omega/\omega_1 - n)}\right\}^2, \tag{2.5}$$

$$G_n(K,\gamma\theta,\phi) = \frac{4n^2}{A^2}\left\{\left[S_1\alpha\cos\phi - \left(S_1 + \frac{2}{n}S_2\right)\frac{A}{2\alpha\cos\phi}\right]^2 + S_1^2\alpha^2\sin^2\phi\right\}, \tag{2.6}$$

$$S_1 = \sum_{k=-\infty}^{+\infty} J_k(n\xi_z)J_{2k+n}(n\xi_x), \tag{2.7}$$

$$S_2 = \sum_{k=-\infty}^{+\infty} kJ_k(n\xi_z)J_{2k+n}(n\xi_x), \tag{2.8}$$

$$\xi_z = \frac{K^2}{4A}, \quad \xi_x = \frac{2K\alpha\cos\phi}{A}, \quad A = 1 + \alpha^2 + \frac{K^2}{2}, \quad \alpha = \gamma\theta, \tag{2.9}$$

$$\omega_1 = \frac{2\gamma^2\omega_0}{1+\gamma^2\theta^2+K^2/2}, \quad \omega_0 = \frac{2\pi c}{\lambda_0}, \tag{2.10}$$

and

$I =$ radiated energy,

$\Omega =$ solid angle,

$\omega =$ angular frequency,

$N =$ number of undulator periods,

$\epsilon_0 =$ permittivity of free space,

$\theta =$ angle with respect to the undulator axis ($\theta = 0$ in the forward direction),

$\phi =$ angle about undulator axis ($\phi = 0$ in the xz plane),

$J_n =$ the Bessel function of the first kind of order n.

In the forward direction (*i.e.* $\theta = 0$) with the fundamental frequency,

$$\omega_{10} = \frac{2\gamma^2\omega_0}{1 + K^2/2}, \tag{2.11}$$

the Eqs. (2.4)–(2.10) simplify to:

$$\left.\frac{\mathrm{d}^2 I}{\mathrm{d}\Omega \mathrm{d}\omega}\right|_{\theta=0} = \frac{q^2\gamma^2N^2}{4\pi\epsilon_0 c} F_n(K) \left\{ \frac{\sin[N\pi(\omega/\omega_{10} - n)]}{\pi N(\omega/\omega_{10} - n)} \right\}^2, \tag{2.12}$$

where

$$F_n(K) = \begin{cases} \frac{K^2n^2}{(1+K^2/2)^2} \times \left[J_{\frac{n+1}{2}}\left(\frac{nK^2/4}{1+K^2/2}\right) - J_{\frac{n-1}{2}}\left(\frac{nK^2/4}{1+K^2/2}\right)\right]^2 & \text{if } n = 1, 3, 5, \ldots \\ 0 & \text{otherwise} \end{cases} . \tag{2.13}$$

2.1.2 Discussion of the Undulator Radiation Formula

Some comments can be made about the physical interpretation of the above formulas. The frequency distribution at a particular observation angle θ is determined by

Eq. (2.5), which is a sharply peaked function that actually becomes a δ-function for an infinitely long undulator [14]:

$$\lim_{N\to\infty} H_n(K,\gamma\theta,\omega) = \lim_{N\to\infty}\left\{\frac{\sin[N\pi(\omega/\omega_1 - n)]}{\pi N(\omega/\omega_1 - n)}\right\}^2 = \frac{1}{N}\delta\left(\frac{\omega}{\omega_1} - n\right). \tag{2.14}$$

For example, when $\theta = 0$ and $n = 1$ Eq. (2.14) is non-zero only when

$$\omega_{10} = 2\gamma^2\omega_0/(1 + K^2/2),$$

which is the formula for the fundamental wavelength of undulator radiation:

$$\lambda = \frac{\lambda_0}{2\gamma^2}\left(1 + \frac{K^2}{2}\right). \tag{2.15}$$

For a finite-N-period undulator with $\theta = 0$ and $n = 1$ then Eq. (2.5) is recognizable as the square of the Fourier transform of an N-period sinusoid at the fundamental wavelength.

The fundamental wavelength and other properties of undulator radiation can be understood by considering that the radiated field measured by an observer is proportional to the *apparent transverse acceleration* [16] of the electron as viewed by the observer. Consider an observer on the z axis. The electron trajectory is periodic with period λ_0, but because the electron is moving almost as fast as the radiation, the pulses from successive periods will appear to the observer time-compressed by a factor of

$$(1 - \beta) \approx \frac{1}{2\gamma^2}, \tag{2.16}$$

where $\beta = v/c$ is the velocity of the electron relative to the velocity of light. This gives the first term in Eq. (2.15). Because it follows a sinusoidal trajectory with amplitude proportional to $K/\gamma \ll 1$, the electron travels further than the radiation by an amount proportional to K^2/γ^2, which gives the second term in Eq. (2.15).

As θ increases from zero in the xz plane, the time-compression seen by the observer decreases, so the observed wavelength increases, as seen in the decrease of ω_1

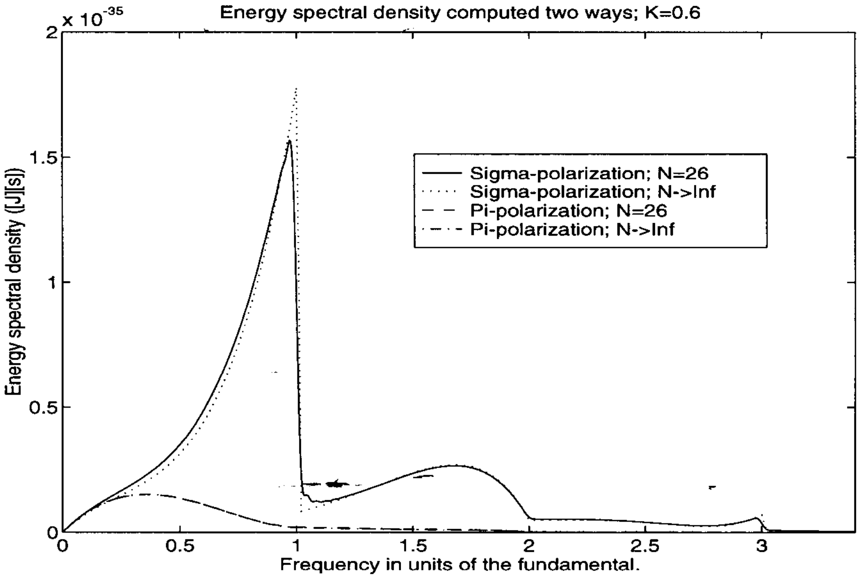

Figure 2.2: Angle-integrated energy spectral density. This figure demonstrates that the $N \longrightarrow \infty$ approximation used in calculating the undulator radiation energy spectral density agrees well with the more accurate $N = 26$ calculation. Also noteworthy is that the radiation is dominated by the horizontally-polarized (σ-polarization) component.

with θ in Eq. (2.10). Additionally, the magnitude of the apparent transverse acceleration decreases, dropping to zero near $\theta = K/\gamma$, where the observer's line-of-sight is tangent to the zero-crossings of the sinusoidal trajectory (there is no bending, so no acceleration at these points). So the observer measures radiation out to about $\theta = K/\gamma$ (in the xz plane). Finally, because the apparent acceleration is mainly in the xz plane, the observer measures radiation mainly polarized in the xz plane. The polarization terms appear in Eq (2.6), where $\left[S_1\alpha\cos\phi - \left(S_1 + \frac{2}{n}S_2\right)\frac{A}{2\alpha\cos\phi}\right]^2$ refers to the horizontal polarization (σ-mode) and $S_1^2\alpha^2\sin^2\phi$ refers to the vertical polarization (π-mode).

2.1.3 Numerical Evaluation

In order to numerically evaluate Eqs. (2.4)-(2.10), it is convenient to take advantage of the δ-like nature of Eq. (2.5) by assuming it *is* a δ-function and doing the integral with respect to $\sin\theta \mathrm{d}\theta$, thus avoiding the computational expense associated with integrating across a sharply-peaked function. This approach has been shown to give good results for large N [17, pages 60–65]. The resulting equation for the energy spectral density of undulator radiation is [17]

$$\frac{\mathrm{d}I}{\mathrm{d}\omega} = \frac{q^2\gamma^2 N}{4\pi\epsilon_0 c}\frac{\omega_0}{\omega}\int_0^{2\pi}\sum_{n=1}^{\infty} G_n(K, \gamma\theta_n, \phi)\mathrm{d}\phi, \tag{2.17}$$

where

$$\theta_n = \sqrt{\frac{2n\omega_0}{\omega} - \frac{(1+K^2/2)}{\gamma^2}}. \tag{2.18}$$

Equations (2.17) and (2.18) are used to compute the expected radiation from one electron passing through a $K = 0.6$ undulator, which is of relevance to the experimental results of this thesis. The computational method is as follows:

- For the frequency ω, find the minimum postive integer n_{min}, if it exists, such that θ_n is real.
- If n_{min} exists then find the maximum positive integer n_{max} such that θ_n is within an acceptance angle θ_a.
- If $n_{max} \geq n_{min}$, then evaluate Eq. (2.17) for the frequency ω where the sum within the integral becomes $\sum_{n=n_{min}}^{n_{max}}$.

Figure 2.2 shows $\frac{\mathrm{d}I}{\mathrm{d}\omega}$ computed from Eqs. (2.17) and (2.18) and also from Eqs. (2.4)-(2.10), with a $10/\gamma$ acceptance angle [18]. This demonstrates that the approximation of Eqs. (2.17) and (2.18) is sufficiently accurate for the purposes of this project.

Applying Eqs. (2.17) and (2.18) to understand the spectral and spatial distribution of the radiation gives Fig 2.3, which shows the energy spectral density of undulator

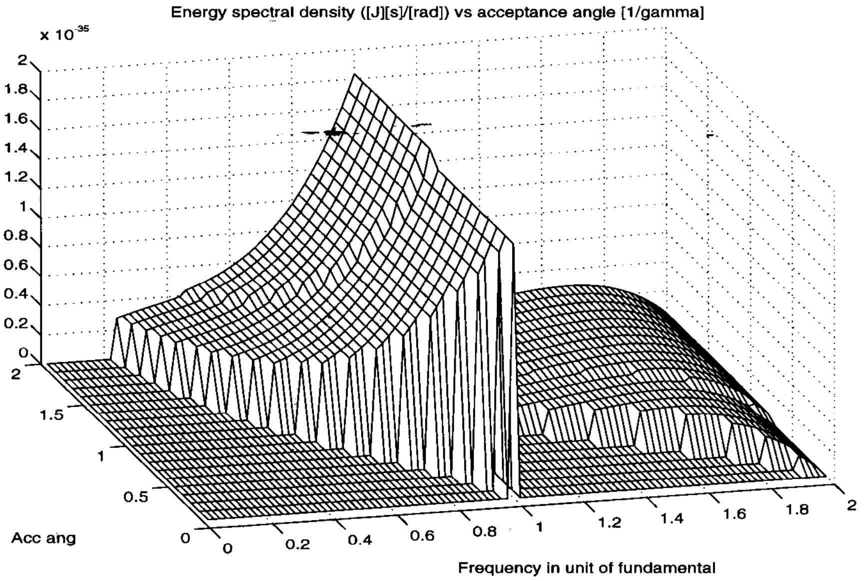

Figure 2.3: Angle-integrated energy spectral density as a function of acceptance angle. As the angular acceptance θ_a, measured as the half-angle of a cone, increases, substantial radiation appears at frequencies below the fundamental. (This calculation is done for $K = 0.6$ using the $N \to \infty$ approximation.)

radiation for $K = 0.6$ as the acceptance angle θ_a is increased. It is worth noting that as the acceptance angle increases, very much radiation appears at angles greater than the so-called 'opening angle' [19, Sec. 4, Eq. (15)] of

$$\theta_{open} = \frac{1}{\gamma}\sqrt{\frac{(1+K^2/2)}{2N}} = \sqrt{\frac{\lambda}{N\lambda_0}}, \tag{2.19}$$

which is the 'opening angle' only for the radiation within a relative frequency band of $\pm\frac{1}{N}$ of the fundamental frequency; that is, it is the opening angle for which the linewidth is not significantly broadened beyond the minimum natural linewidth. If *all* frequencies are considered, then the spatial distribution appears as in Fig. 2.4, which shows Eqs. (2.17) and (2.18) evaluated for $n = 1$, and clearly exhibits substantial radiated energy out to angles $\sim \frac{1}{\gamma}$.

2.2 Coherent Enhancement: the Form Factor

The formalism for calculating the coherent radiation from a bunched beam was worked out by Nodvick and Saxon [20] by adding the radiated fields from each electron in the bunch. Following this approach, consider N_e electrons travelling through an undulator, entering at times t_j and transverse offsets $\vec{r}_{j\perp}$. Assume the electrons have the same injection angle —so that they follow parallel trajectories— and assume that they have the same energy. Then for radiation at frequency ω in direction $\hat{\mathbf{n}}$ the observer will see a field $\vec{E}_{tot}(\vec{k})$ equal to the sum of the fields from each electron:

$$\vec{E}_{tot}(\vec{k}) = \vec{E}_{1e}(\vec{k})\sum_{j=1}^{N_e} e^{i(\omega t_j + \vec{k}\cdot\vec{r}_{j\perp})}. \tag{2.20}$$

Here $\vec{E}_{1e}(\vec{k})$ is the field radiated by a single electron and $\vec{k} = \hat{\mathbf{n}}\omega/c$ is the wavevector to the observer, where $\hat{\mathbf{n}}$ is a (constant) unit vector from the undulator to the observer. Equation (2.20) can be written more simply by relating time and transverse postion coordinates to, for example, the first electron entering the the undulator. The other

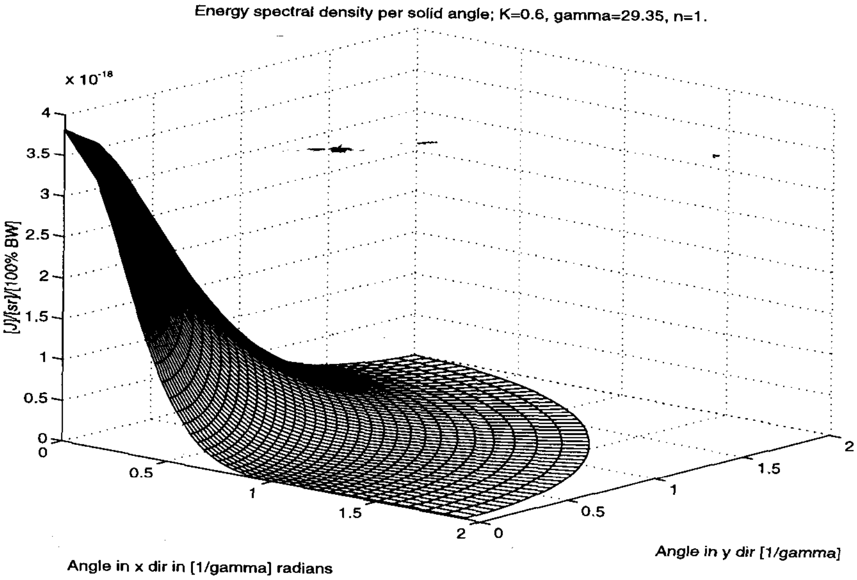

Figure 2.4: Peak energy spectral density as a function of angle. The peak energy spectral density (energy spectral density at $\omega = \omega_1$) per solid angle evaluated for $K = 0.6$, $N = 26$, $\gamma = 29.35$, and $n = 1$ shows that the radiation does not drop to zero until $\theta > \frac{1}{\gamma}$. The $n = 1$ term accounts for over 60% of the radiated power when K=0.6.

electrons will then enter at times $t_j = z_j/c$ and Eq. (2.20) becomes

$$\vec{E}_{tot}(\vec{k}) = \vec{E}_{1e}(\vec{k}) \sum_{j=1}^{N_e} e^{i\vec{k}\cdot\vec{r}_j}, \tag{2.21}$$

where $\vec{r}_j = \vec{r}_{j\perp} + z_j\hat{\mathbf{z}}$ locates the j-th electron with respect to the first electron. The power radiated is proportional to the square of the field so

$$P_{tot}(\vec{k}) = P_{1e}(\vec{k}) \left| \sum_{j=1}^{N_e} e^{i\vec{k}\cdot\vec{r}_j} \right|^2 . \tag{2.22}$$

In the continuum limit one defines a probability distribution $S(\vec{r})$for the charge density of the electron bunch:

$$1 = \int S(\vec{r})\mathrm{d}^3 r, \tag{2.23}$$

and the total power (at the frequency $\omega = ck$ in direction $\hat{\mathbf{k}}$) then can be expressed as

$$P_{tot}(\vec{k}) = P_{1e}(\vec{k}) N_e^2 \left| \int S(\vec{r}) e^{i\vec{k}\cdot\vec{r}_j} \mathrm{d}^3 r \right|^2 . \tag{2.24}$$

Thus coherent enhancement, and in fact the entire effect of the bunch structure, is characterized by the form factor $f(\vec{k})$ defined as

$$f(\vec{k}) = \left| \int S(\vec{r}) e^{i\vec{k}\cdot\vec{r}_j} \mathrm{d}^3 r \right|^2 , \tag{2.25}$$

which is the square of the 3-dimensional Fourier transform of the bunch distribution. In this derivation the only assumptions are equal and constant particle energies and parallel trajectories (that is, equal injection angles); the form factor then just follows from the principle of superposition.

With the form factor and total power defined in this way, a random N_e-particle distribution has a form factor of $1/N_e$, as is familiar from the random walk problem for example, and thus Eq. (2.24) shows that the incoherent radiated power is proportional to the number of electrons. If all the electrons are at an identical phase with respect to $\vec{k}$, then the form factor has its maximum value of one, which is the case of maximum coherent enhancement.

2.3 Coherent Enhancement of Undulator Radiation

A possible point of confusion is that the form factor can show coherent enhancement from electrons that are causally separated. For example consider the forward radiation from two electrons, separated by an integer $M > N$ fundamental wavelengths, travelling through an N-period undulator. Then the form factor is one, and Eq. (2.24) predicts the maximum coherent enhancement—yet the observer sees just two N-period wave-packets completely separated in time/space, so there can be *no* coherent enhancement in the radiated energy. If one realizes that $\vec{E}(\omega)$ in the derivation is really the *Fourier amplitude* of the field, and therefore $P(\omega)$ is the power *spectral density*, then the apparent contradiction is resolved: there is coherent enhancement of the energy spectral density at the fundamental, but there is no coherent enhancement of the total energy because the bandwidth of the radiation has been reduced exactly enough so that the total energy is just the sum of the energies in the two causally separated wave-packets. Since this example is of fundamental importance in calculating coherent enhancement of undulator radiation, a mathematical demonstration is now presented.

2.3.1 Coherent Enhancement in the Forward Direction

Consider an undulator which causes an electron to radiate an N-period sine wave in the forward direction at the fundamental frequency ω_{10}. The Fourier transform of the radiated field is then [1]

$$E_{1e}(\omega) \propto \int_0^{2\pi N/\omega_{10}} e^{i\omega_{10}t} e^{-i\omega t} \mathrm{d}t = \frac{2\pi N}{\omega_{10}} \left(e^{-i\pi N \frac{\omega-\omega_{10}}{\omega_{10}}} \right) \left[\frac{\sin(\pi N \frac{\omega-\omega_{10}}{\omega_{10}})}{\pi N \frac{\omega-\omega_{10}}{\omega_{10}}} \right], \qquad (2.26)$$

---

[1] here units are dropped as they are irrelevant to the argument.

so the energy spectral density from one electron is

$$\left(\frac{\mathrm{d}I}{\mathrm{d}\omega}\right)_{1e} \propto \left(\frac{2\pi N}{\omega_{10}}\right)^2 \left[\frac{\sin(\pi N \frac{\omega-\omega_{10}}{\omega_{10}})}{\pi N \frac{\omega-\omega_{10}}{\omega_{10}}}\right]^2 . \tag{2.27}$$

The energy radiated by one electron will then be the integral over frequency of Eq. (2.27) which gives

$$I_{1e} \propto \frac{4\pi^2 N}{\omega_{10}}, \tag{2.28}$$

that is, the total energy is proportional to the number of oscillations multiplied by the period of the oscillations. Now consider 2 electrons separated by M fundamental wavelengths. The form factor of this 'bunch' is then

$$f(\omega) = \left| \int_{-\infty}^{+\infty} \left(\frac{\delta(t) + \delta(t + 2\pi M/\omega_{10})}{2}\right) e^{-i\omega t} \mathrm{d}t \right|^2 = \cos^2\left(\pi M \frac{\omega}{\omega_{10}}\right), \tag{2.29}$$

and the energy spectral density will be given by

$$\left(\frac{\mathrm{d}I}{\mathrm{d}\omega}\right)_{tot} \propto 2^2 \cos^2\left(\pi M \frac{\omega}{\omega_{10}}\right) \left(\frac{2\pi N}{\omega_{10}}\right)^2 \left[\frac{\sin(\pi N \frac{\omega-\omega_{10}}{\omega_{10}})}{\pi N \frac{\omega-\omega_{10}}{\omega_{10}}}\right]^2 , \tag{2.30}$$

by application of Eq. (2.24). Defining the variable $u = \pi(\omega - \omega_{10})/\omega_{10}$ leads to

$$I_{tot} \propto \int_{-\infty}^{\infty} \left(\frac{\mathrm{d}I}{\mathrm{d}\omega}\right)_{tot} \mathrm{d}\omega = \frac{16\pi}{\omega_{10}} 2 \int_0^{\infty} \frac{\cos^2(Mu)\sin^2(Nu)}{u^2} \mathrm{d}u, \tag{2.31}$$

and using integral tables [21, Eq. (3.828.11)]

$$I_{tot} \propto \begin{cases} \frac{8\pi^2}{\omega_{10}} N & \text{if } M > N \\ \frac{16\pi^2}{\omega_{10}}(N - M) & \text{if } M \leq N \end{cases} . \tag{2.32}$$

So, as expected, when the wave-packets do not overlap ($M > N$) the energy from two electrons is twice the energy from one, that is there is no coherent enhancement of the energy. But as the electrons move together so that the radiated wave-packets overlap the energy increases proportionally to the overlap, reaching a maximum of 4 times the single-electron energy when the two electrons are at the same location ($M = 0$), also as expected.

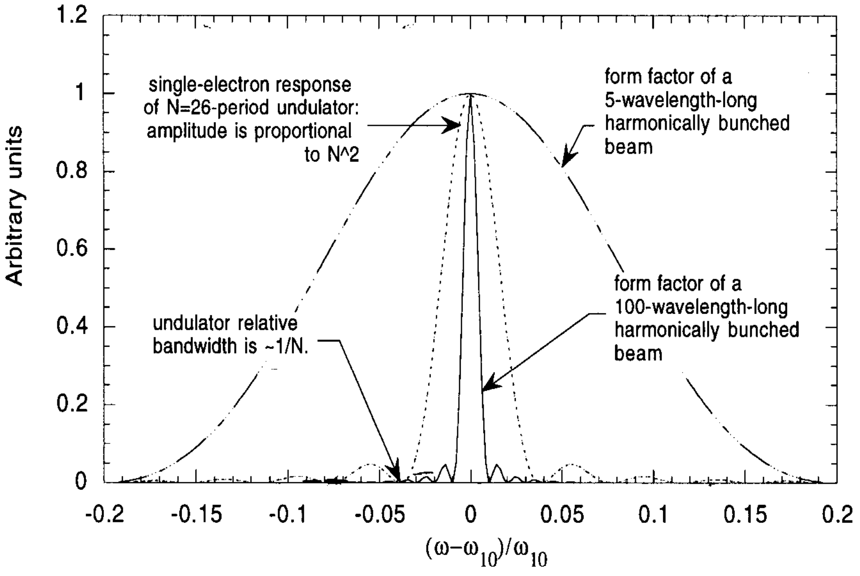

Figure 2.5: Long bunch vs. short bunch form factors. The form factor for a long harmonically bunched beam is δ-like, compared to the undulator response, while that of a shorter bunch is wide.

This shows that the form factor, after integration over frequency, correctly handles arbitrarily long or short bunches. This is important at SUNSHINE, where the undulator operates in the short-bunch regime: typically $M < 5$ and $N = 26$ and similarly to the above development it is expected that the radiated energy is proportional to the number of undulator periods N.

In contrast to the short-bunch regime at SUNSHINE, the FEL community often works with bunches much longer than N radiation wavelengths, having density modulation at the radiation wavelength. In such a case the form factor becomes very narrow in frequency space, much narrower than the bandwidth of the single-electron response of Eq. (2.5). Thus when the frequency integral of Eq. (2.24) is taken, the total energy is determined by the amplitude of the single-electron energy spectral density at the radiation wavelength, which, according to Eq. (2.4) is proportional to

N^2, the *square* of the number of undulator periods. This is *not* the case at SUNSHINE, where the form factor of the electron bunch is usually much broader than the single-electron response. At SUNSHINE, when the frequency integral of Eq. (2.24) is taken, the $1/N$ bandwidth of the single-electron response applies and makes the expected energy proportional only to N, *not* N^2. The diagram of Fig. 2.5 illustrates this.

2.3.2 Coherent Enhancement in Arbitrary Direction

The same principles of coherent enhancement discussed for the forward direction of course apply to any direction. The 3-dimensional form factor is defined in $\vec{k}$-space and together with the $\vec{k}$-space distribution of the radiation from a single electron (*i.e.*, the impulse response of the undulator) completely characterizes the radiation from the bunch. To get the total energy radiated by the bunch one simply multiplies the form factor by the single-electron response and integrates the result (which is Eq. (2.24)) over $\vec{k}$-space.

To model the electron beam distribution, it is reasonable to use a uniform-density cylinder. Of course real bunches do not follow such a hard-edge distribution, but their basic shapes agree with this model. The sharp edges of the cylinder may produce more high-frequency components than are present in the real bunch; an alternate model, that avoids this, is the much smoother Gaussian distribution. The measured longitudinal distribution at SUNSHINE has been found to be somewhere between these two models, tending to be closer to the uniform-density distribution [22, page 96] than to the Gaussian distribution.

The form factor of a uniform-density cylindrical electron bunch can be found easily in cylindrical coordinates:

$$f(\vec{k}) = \left(\frac{1}{\pi r_{max}^2 l}\right)^2 \left| \int_{-l/2}^{+l/2} \int_0^{2\pi} \int_0^{r_{max}} e^{i\vec{k}\cdot\vec{r}} r \mathrm{d}r \mathrm{d}\phi \mathrm{d}z \right|^2 \qquad (2.33)$$

where l is the bunch length and r_{max} is the bunch radius. Since there is cylindrical symmetry $\vec{k} \cdot \vec{r}$ can be evaluted in the yz plane (with the correct final result) giving

$$\vec{k} \cdot \vec{r} = k_{\perp} r \sin\phi \hat{\mathbf{y}} + k_z z \hat{\mathbf{z}}$$

where $k_{\perp}$ is the magnitude of the component of $\vec{k}$ in the xy plane. Then

$$f(\vec{k}) = \left(\frac{1}{\pi r_{max}^2 l}\right)^2 \left| \int_{-l/2}^{+l/2} e^{ik_z z} \mathrm{d}z \int_0^{r_{max}} \left(\int_0^{2\pi} e^{ik_{\perp} r \sin\phi} \mathrm{d}\phi \right) r \mathrm{d}r \right|^2$$

which evaluates to

$$f_{uniform}(\vec{k}) = \left[\frac{\sin(k_z l/2)}{k_z l/2}\right]^2 \left[\frac{2J_1(r_{max} k_{\perp})}{r_{max} k_{\perp}}\right]^2. \tag{2.34}$$

The first term in brackets is recognized as the Fraunhofer diffraction pattern of a slit of width l in the $\hat{\mathbf{z}}$-direction, and the second term in brackets is recognized as the Fraunhofer diffraction pattern of a circular aperture of radius r_{max}. (This is not suprising since the Fraunhofer diffraction pattern of an aperture can be calculated from Huygens' principle by considering the aperture to be filled with radiating sources, in the same way that the form factor of an electron bunch is calculated.) The first term has a maximum of one if $k_z \to 0$ and falls to zero when $k_z = 2\pi/l$ while the second term has a maximum of one if $k_{\perp} \to 0$ and falls to zero when $k_{\perp} = 3.832/r_{max}$.

If the beam distribution is Gaussian in each of the three dimensions with standard deviations σ_x, σ_y, and σ_z respectively, then each of the three rectangular coordinates are independent. In the $\hat{\mathbf{z}}$-direction,

$$f(k_z) = \left[\frac{1}{\sqrt{2\pi}\sigma_z} \int_{-\infty}^{+\infty} e^{-\frac{z^2}{2\sigma_z^2}} e^{ik_z z} \mathrm{d}z\right]^2.$$

This evaluates to

$$f(k_z) = e^{-\sigma_z^2 k_z^2},$$

and so overall

$$f_{Gauss}(\vec{k}) = e^{-\sigma_x^2 k_x^2} e^{-\sigma_y^2 k_y^2} e^{-\sigma_z^2 k_z^2}. \tag{2.35}$$

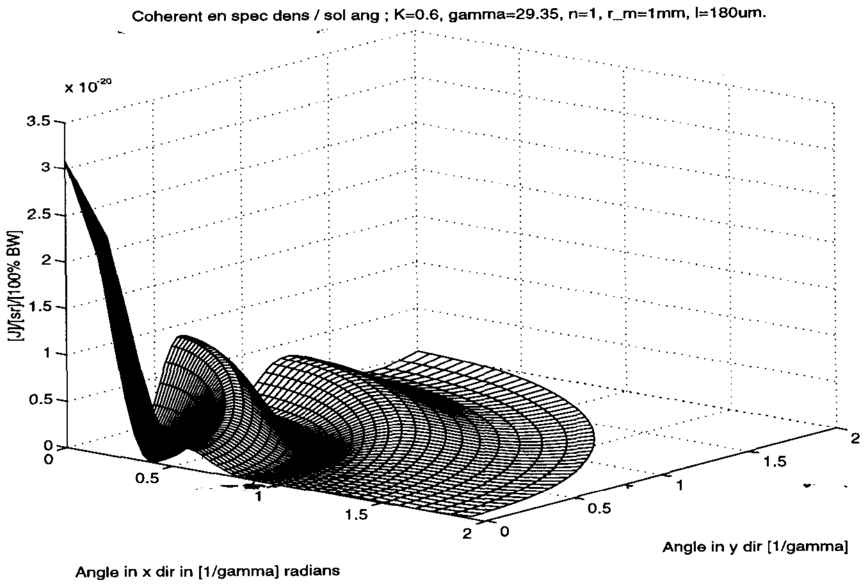

Figure 2.6: Peak energy spectral density vs. angle with form factor effect. The form factor of a 1 mm radius, 180 μm long bunch multiplies the incoherent radiation distribution to produce the coherent distribution. The parameters of this calculation are $N = 26$, $K = 0.6$, $\gamma = 29.35$, and $n = 1$. This figure can be compared directly with Fig. 2.4.

2.3.3 Numerical Evaluation of Superradiant Undulator Radiation

The expected superradiant undulator radiation from SUNSHINE can now be calculated. The undulator strength is taken to be $K = 0.6$ as in many of the experiments discussed later in this thesis, and the electron bunch is modeled as a uniform-density cylinder of 1 mm radius and 180 μm length.

To visualize the coherently-enhanced spatial distribution the $n = 1$ term in G_n of Eq. (2.6) is computed with a resulting single-electron spatial distribution of peak energy spectral density as shown in Fig. 2.4. By 'peak' energy spectral density is meant the energy spectral density at ω_1 for the given angle θ. The $n = 1$ term shown in the figure includes over 60% of the total radiation for $K = 0.6$. In Fig. 2.4 each direction corresponds to a specific frequency of radiation which allows straightforward application of the form factor for a cylindrical bunch of radius $r_{max} = 1$mm and length 180μm, giving Fig. 2.6.

Figure 2.6 shows the effect of shape of the bunch in the ripples. The zero at angle $0.4/\gamma$ is because angle $0.4/\gamma$ corresponds to radiation at frequency 60 μm, which is at a zero of the 180 μm uniform distribution form-factor. The zero at $\gamma\theta = 1$ is the first zero of $J_1(u)/u$. At larger angles, the increase in (relative) intensity compared to the single-electron distribution of Fig. 2.4 is a consequence of the lower frequency of the large-angle radiation, which allows more coherent enhancement. At angles greater than the $2/\gamma$ shown even lower frequencies become enhanced but these angles are well outside of the acceptance of the experimental apparatus used in this project.

To visualize the effect of the coherent enhancement on the observable energy spectral density, the form-factor-enhanced version of the single-electron distribution of Fig. 2.3 is displayed in Fig. 2.7, showing that some of the lower frequencies are enhanced by the coherent effect while others are cancelled.

Finally, for future reference, Table 2.1 tabulates the radiated energy in Joules expected from a single electron in each polarization mode (second and third columns), then the same quantities after including the form factor (fourth and fifth columns), as a function of increasing values of acceptance angle (first column). Note that at $3/\gamma$ acceptance the total energy for a single electron is tabulated as 3.06×10^{-22} J, which agrees well with the formula:

$$E_{tot} = \frac{\pi q^2}{3\epsilon_0}\frac{N\gamma^2 K^2}{\lambda_0} = 3.18 \times 10^{-22}\ \text{J}. \tag{2.36}$$

(The missing 4% appears at angles greater than $3/\gamma$.)

While Table 2.1 uses the $N \rightarrow \infty$ approximation, Eq. (2.12) is more accurate (in the $\theta = 0$ direction) and predicts the forward energy into an accepting solid

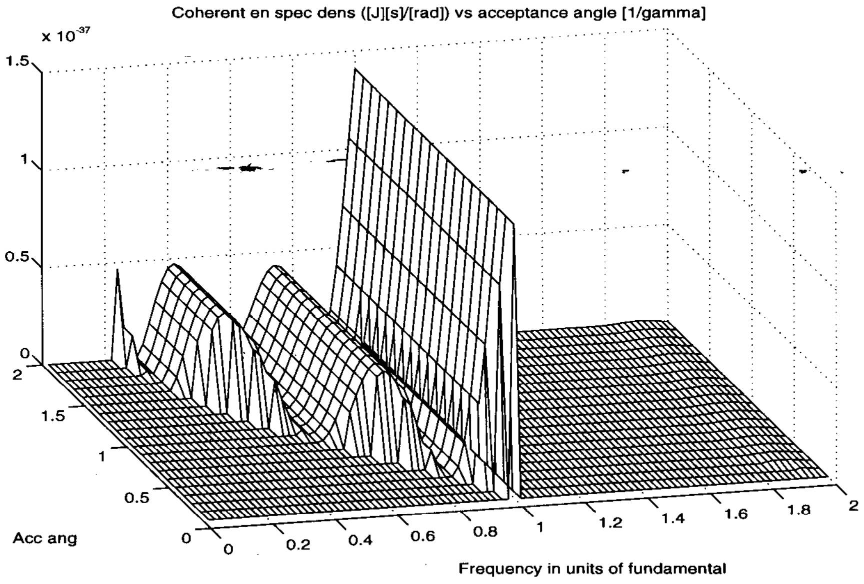

Figure 2.7: Coherently-enhanced energy spectral density as acceptance angle is increased. The acceptance angle is measured in units of $1/\gamma$ and the frequency is measured in units of the fundamental frequency $\omega_{10} = 3.57 \times 10^{13}$ rad/s. The parameters for this calculation are $K = 0.6$, $N = 26$, $\gamma = 29.35$, $l = 180$ μm, and $r_{max} = 1$ mm. The $N \rightarrow \infty$ approximation is used, with $n = 1$ to 15. This figure can be directly compared with Fig. 2.3.

angle of $\pi\theta_a^2 = \pi(\frac{0.1}{\gamma})^2 = 3.646 \times 10^{-5}$, over a relative bandwidth of $1/N$, will be 5.356×10^{-24} J, which is close to the 6.866×10^{-24} J obtained (in the $N \rightarrow \infty$ monochromatic approximation) in the first row of Table 2.1. The discrepancy is due to the finite step size of integration used in computing Table 2.1 (a step of 0.5% of the fundamental frequency was used) which creates some error with the extremely sharp frequency spectrum that occurs at small opening angles in the $N \rightarrow \infty$ approximation. Table 2.1 rapidly becomes more accurate at larger opening angles.

$\alpha = \gamma\theta_a$	σ_{1e}	π_{1e}	σ_{coh}	π_{coh}
0.1	6.866e-24	3.738e-27	4.873e-26	3.052e-30
0.2	2.357e-23	5.659e-26	1.434e-25	7.434e-29
0.3	4.907e-23	2.593e-25	2.193e-25	3.027e-28
0.4	7.717e-23	7.092e-25	2.34e-25	4.059e-28
0.5	1.091e-22	1.539e-24	2.451e-25	6.442e-28
0.6	1.406e-22	2.815e-24	3.08e-25	3.126e-27
0.7	1.682e-22	4.504e-24	3.917e-25	9.051e-27
0.8	1.911e-22	6.623e-24	4.411e-25	1.477e-26
0.9	2.09e-22	9.013e-24	4.5e-25	1.627e-26
1	2.225e-22	1.157e-23	4.53e-25	1.713e-26
1.1	2.33e-22	1.436e-23	4.756e-25	2.514e-26
1.2	2.403e-22	1.688e-23	5.115e-25	4.085e-26
1.3	2.462e-22	1.948e-23	5.552e-25	6.352e-26
1.4	2.505e-22	2.184e-23	5.892e-25	8.385e-26
1.5	2.541e-22	2.418e-23	6.107e-25	9.826e-26
1.6	2.565e-22	2.593e-23	6.169e-25	1.028e-25
1.7	2.59e-22	2.789e-23	6.179e-25	1.036e-25
1.8	2.606e-22	2.923e-23	6.194e-25	1.048e-25
1.9	2.62e-22	3.05e-23	6.271e-25	1.116e-25
2	2.633e-22	3.168e-23	6.472e-25	1.296e-25
2.1	2.642e-22	3.259e-23	6.746e-25	1.549e-25
2.2	2.65e-22	3.342e-23	7.158e-25	1.937e-25
2.3	2.658e-22	3.421e-23	7.737e-25	2.492e-25
2.4	2.664e-22	3.472e-23	8.229e-25	2.97e-25
2.5	2.67e-22	3.541e-23	9.137e-25	3.862e-25
2.6	2.675e-22	3.587e-23	9.862e-25	4.582e-25
2.7	2.679e-22	3.629e-23	1.068e-24	5.403e-25
2.8	2.681e-22	3.652e-23	1.113e-24	5.851e-25
2.9	2.685e-22	3.689e-23	1.208e-24	6.819e-25
3	2.687e-22	3.709e-23	1.259e-24	7.338e-25

Table 2.1: The angle-integrated frequency-integrated radiated energy in the 2 polarizations. The acceptance angle (first column) is measured in units of $1/\gamma$. The radiated energy is measured in Joules. The first and second columns are the results for one electron, the third and fourth columns are the one electron results multiplied by the form factor. The parameters for this calculation are $K = 0.6$, $N = 26$, $\gamma = 29.35$, $l = 180$ μm, and $r_{max} = 1$ mm. The $N \to \infty$ approximation is used, with $n = 1$ to 15.

Chapter 3

Theory of Self-Amplified Spontaneous Emission

The key assumptions in deriving the superradiant undulator radiation formulas of the preceding chapter were that the electrons had equal energies and followed parallel trajectories. One consequence of these assumptions is that the bunch emerges from the undulator with the same shape as it had when it entered. If the bunch does change shape, for example due to different electrons radiating different amounts of energy and following slightly different trajectories, then large changes in the radiated energy may be seen due to the powerful effect of coherent enhancement. To model this type of behavior, theory must account for the effect of the radiation on the bunch dynamics.

High-gain FEL theory is concerned with this bunch/radiation dynamics. When there is no external (seed) radiation field, the high-gain FEL dynamics is referred to as SASE (Self-Amplified Spontaneous Emission) [31, for example].

The basic physics involves the interaction between the radiated field, the energy distribution of the electron beam, and the charge density of the electron beam. In a typical FEL the beam enters the undulator randomly bunched. The individual electrons radiate at the fundamental frequency but with random phases, creating radiation at the fundamental frequency with power proportional to the current. As the beam continues to propagate, electrons which radiate in phase with the spontaneous field do work on it and lose energy, and consequently take a longer path through the undulator. Other electrons gain energy from the field and take shorter paths through the undulator. This energy-dependent path length provides a mechanism whereby the beam can become bunched at the radiation wavelength thus greatly increasing the radiated power, and is the source of gain in a single-pass FEL.

In a low-gain FEL an external field at frequency somewhat lower than the fundamental frequency is amplified because particles that lose energy spend more time in phase with the field, causing them to lose more energy, whereas particles at a phase to gain energy spend less time at that phase and tend to move to a phase in which they lose energy. Thus the particles tend to bunch at the radiation frequency, at a phase in which they amplify the field. In a high-gain FEL bunching can occur at the fundamental frequency because the radiation is slowed down by the beam where it is being amplified [23, page 53].

3.1 Single-Pass FEL Theory

The simplest single-pass FEL model to examine computationally is a one dimensional model. This provides insight into the physics and a quantitative prediction of radiation gain that can be compared with experiment. The theoretical literature on high-gain FELs is voluminous [24–29,11,30,31, for example] including review articles [23,32, for example] and even books [33, for example]. For the purposes of this project linearized, scaled FEL equations [11] are applied as these permit a straightforward analytical formulation covering the cases of no-gain, low-gain, and high-gain operation. The no-gain limit corresponds to the coherently-enhanced undulator radiation discussed in the previous chapter, and was originally the expected behavior for this experiment.

There exists a one-dimensional theory specifically describing the short-pulse superradiant regime [34], but to the author's knowledge this theory has not been formulated in a manner that covers the low and zero-gain limit, nor does it include the effects of energy modulation of the initial electron bunch. Therefore, the theory of Ref. [34] is not applied in this thesis.

3.1.1 Mathematical Formulation

Qualitatively, it is expected that the radiation field is mathematically related to the bunching and energy modulation of the beam. In a linear model therefore one would expect three equations relating the development of the three quantities (field, bunching, and energy modulation), with particular solutions depending on the initial conditions of the three quantities. Such a model exists and is documented in many places [11,35, for example]. A review article by Murphy and Pellegrini [23] is the reference for this section. A definition of variables used in the mathematical formulation is given in Table 3.1.

Table 3.1: Definition of SASE parameters

Definition of SASE parameters			
τ	$=$	$2\omega_0\rho\frac{\gamma_R^2}{\gamma_0^2}t$	normalized time
ω_0	$=$	$2\pi c/\lambda_0 \;=\; k_0 c$	undulator frequency
ρ	$=$	$\left(\frac{(K/\sqrt{2})[JJ]\gamma_0\Omega_p}{4\gamma_R^2\omega_0}\right)^{2/3}$	Pierce parameter
γ_R^2	$=$	$\frac{k_r(1+(K/\sqrt{2})^2)}{2k_0}$	resonant energy
k_r			radiation wavenumber
γ_0			initial energy of beam

Continued on the next page

Definition of SASE parameters, continued

$[JJ]$	$=$	$J_0\left(\frac{K^2/4}{1+K^2/2}\right)-J_1\left(\frac{K^2/4}{1+K^2/2}\right)$	planar undulator coupling correction
Ω_p	$=$	$\left(\frac{n_e q^2}{\epsilon_0 m\gamma_0}\right)^{1/2}$	relativistic plasma frequency
n_e			number density of electron bunch
X	$=$	$q\alpha_0^{i\dot{\theta}_0 t}\frac{(K/\sqrt{2})}{4mc^2\gamma_R^2 k_0\rho^2}$	normalized slowly varying amplitude
α_0	$=$	$-iE_{r0}e^{i\psi_{r0}}$	slowly varying amplitude
$\lvert X\rvert^2$	$=$	$\frac{\epsilon_0\lvert E_r\rvert^2}{mc^2\rho\gamma_0 n_e}$	
$\dot{\theta}_0$	$=$	$\omega_0\left(1-\frac{\gamma_r^2}{\gamma_0^2}\right)$	
Y	$=$	$\left\langle e^{-i\psi_{0j}}\theta_j\right\rangle$	bunching parameter
$\langle\cdot\rangle$	$=$	$\frac{1}{N_e}\sum_{j=1}^{N_e}(\cdot)$	averaging
j	$=$	$1,2,\ldots N_e$	indexing
ψ_{0j}	$=$	$2\pi(j-1)/N_e$	reference phase
θ_j	$=$	$\psi_{0j}-\psi_j$	phase perturbation
Z	$=$	$\left\langle\frac{e^{-i\psi_{0j}}\eta_j}{\rho}\right\rangle$	normalized energy distribution
η_j	$=$	$\frac{\gamma_j-\gamma_0}{\gamma_0}$	relative energy deviation
σ^2	$=$	$4\rho^2\frac{(1+(\frac{K}{\sqrt{2}})^2)}{(\frac{K}{\sqrt{2}})^2}$	space charge parameter
δ	$=$	$\frac{\gamma_0^2-\gamma_R^2}{2\gamma_R^2\rho}$	detuning parameter

The three equations which describe the interaction between the radiated field X, the bunching parameter Y, and the energy distribution Z in the linear model are derived in the reference [23]:

$$\dot{X}-i(\delta-\frac{1}{2}\sigma^2)X+iY+\rho Z=0, \tag{3.1}$$

$$-i\rho X+\dot{Y}-Z=0, \tag{3.2}$$

$$X+\frac{\sigma^2}{\rho}Y+\dot{Z}=0. \tag{3.3}$$

The solution of these equations (3.1-3.3), including the effects of the initial conditions, can be found by taking their Laplace transforms, defined by

$$\mathcal{X}(s) = \int_0^\infty X(\tau) e^{-s\tau} \mathrm{d}\tau.$$

This gives

$$\begin{pmatrix} s - i(\delta - \frac{1}{2}\sigma^2) & i & \rho \\ -i\rho & s & -1 \\ 1 & \frac{\sigma^2}{\rho} & s \end{pmatrix} \begin{pmatrix} \mathcal{X}(s) \\ \mathcal{Y}(s) \\ \mathcal{Z}(s) \end{pmatrix} = \begin{pmatrix} X_0 \\ Y_0 \\ Z_0 \end{pmatrix}, \tag{3.4}$$

where X_0, Y_0, and Z_0 are the initial conditions. Setting determinant of the matrix to zero gives the poles (natural response, homogeneous solutions) of the system via the dispersion relation:

$$\left[s - i\left(\delta - \frac{1}{2}\sigma^2\right)\right]\left(s^2 + \frac{\sigma^2}{\rho}\right) - 2\rho s - i\rho\sigma^2 - i = (s - s_1)(s - s_2)(s - s_3) = 0, \tag{3.5}$$

where s_1, s_2, s_3 are of course the solutions of the dispersion relation. The solution for the Laplace transform of the field variable, $\mathcal{X}(s)$, is

$$(s - s_1)(s - s_2)(s - s_3)\mathcal{X}(s) = \det \begin{vmatrix} X_0 & i & \rho \\ Y_0 & s & -1 \\ Z_0 & \frac{\sigma^2}{\rho} & s \end{vmatrix} \tag{3.6}$$

so

$$\mathcal{X}(s) = \frac{X_0(s^2 + \frac{\sigma^2}{\rho}) - Y_0(is - \sigma^2) - Z_0(\rho s + i)}{(s - s_1)(s - s_2)(s - s_3)}. \tag{3.7}$$

After partial fraction expansion and transformation back to the τ domain the result for the field as a function of τ is

$$\begin{aligned} X(\tau) &= \left(\frac{X_0(s_1^2 + \frac{\sigma^2}{\rho}) - Y_0(is_1 - \sigma^2) - Z_0(\rho s_1 + i)}{(s_1 - s_2)(s_1 - s_3)}\right) e^{s_1\tau} \\ &+ \left(\frac{X_0(s_2^2 + \frac{\sigma^2}{\rho}) - Y_0(is_2 - \sigma^2) - Z_0(\rho s_2 + i)}{(s_2 - s_1)(s_2 - s_3)}\right) e^{s_2\tau} \\ &+ \left(\frac{X_0(s_3^2 + \frac{\sigma^2}{\rho}) - Y_0(is_3 - \sigma^2) - Z_0(\rho s_3 + i)}{(s_3 - s_1)(s_3 - s_2)}\right) e^{s_3\tau}. \end{aligned} \tag{3.8}$$

Equation (3.8) includes the effect of initial perturbations in the field, bunching, and energy modulation via the three initial conditions X_0, Y_0, and Z_0. The author has not found inclusion of the energy modulation terms elsewhere in the literature. Typically it is assumed that $Z_0 = 0$, when Eq. (3.8) can be shown to give the correct low gain and zero gain limits [23].

As a simple example of the solution of Eq. (3.8) consider the case of small δ, σ, and ρ. Then Eq. (3.5) becomes

$$s^3 = i$$

which has solutions

$$s_{1,2,3} = e^{i\pi/6},\ e^{i5\pi/6},\ e^{i9\pi/6} = (\sqrt{3}/2 + i/2), (-\sqrt{3}/2 + i/2), (-i).$$

and so in Eq. (3.8)

$$X(\tau) = \left(\frac{s_1^2 X_0}{(s_1 - s_2)(s_1 - s_3)} \right) e^{(\sqrt{3}/2 + i/2)\tau} + \cdots.$$

The $e^{(\sqrt{3}/2)\tau}$ term gives exponential growth of the field as $e^{2\pi\sqrt{3}\rho N}$ and thus exponential growth of the radiated energy as e^{N/N_g} where

$$N_g = \frac{1}{4\pi\sqrt{3}\rho} \tag{3.9}$$

is the energy gain length in terms of the number of undulator periods N. After several gain lengths the exponential growing term will dominate, but at the beginning of the undulator the exponentially damped and the oscillating terms must also be considered.

Along with Eq. (3.8) for the field variable, similar expressions can be derived for the bunching parameter Y

$$\begin{aligned} Y(\tau) &= \frac{X_0(i\rho s_1 - 1) + Y_0(s_1^2 - is_1(\delta - \frac{\sigma^2}{2}) - \rho) + Z_0(s_1 - i(\delta - \frac{\sigma^2}{2}) - i\rho^2)}{(s_1 - s_2)(s_1 - s_3)} \\ &\times \ e^{s_1\tau} \\ &+ \ \text{similar terms for } e^{s_2\tau} \text{and } e^{s_3\tau} \end{aligned} \tag{3.10}$$

and for the energy modulation Z

$$\begin{aligned} Z(\tau) &= \frac{X_0(-i\sigma^2 - s_1) - Y_0(\frac{\sigma^2}{\rho}(s_1 - i(\delta - \frac{\sigma^2}{2})) - i) + Z_0(s_1^2 - is_1(\delta - \frac{\sigma^2}{2}) - \rho)}{(s_1 - s_2)(s_1 - s_3)} \\ &\times \ e^{s_1\tau} \\ &+ \ \text{similar terms for } e^{s_2\tau} \text{and } e^{s_3\tau}. \end{aligned} \tag{3.11}$$

The slowly-varying envelope approximation used in obtaining the above formulas assumes the radiation field can be written in the form

$$E(z,t) = E_r(z,t)e^{i\psi_r(z,t)}e^{i(k_r z - \omega_r t)} \tag{3.12}$$

where the time (and spatial) variation of E_r and ψ_r are much slower than ω_r (and k_r). Thus Eq. (3.8) describes the development of the Fourier amplitude X corresponding to a particular radiation frequency ω_r. To get the complete solution $X_{\omega_r}(\tau)$ is computed for each frequency ω_r of interest. These X_{ω_r} give the radiated energy spectral density per solid angle in the forward direction as a function of undulator length.

To link the theory to experiment, the initial conditions X_0, Y_0, and Z_0 for the field, bunching, and energy modulation must be specified. The initial field X_0 is simply zero. The bunching parameter is defined in Table 3.1:

$$Y = \left\langle e^{-i\psi_{0j}}\theta_j \right\rangle. \tag{3.13}$$

For the purposes of determining the inital condition Y_0 for continuous finite-length distributions, the definition

$$Y = \int_0^l e^{-ikz} S(z) \mathrm{d}z, \tag{3.14}$$

where l is the bunch length and $S(z)$ is the longitudinal particle density normalized to one, is used. This gives a non-zero value for a rectangular distribution ($S(z) = 1/l$) if it is not an integral number of wavelengths long:

$$Y_0 = e^{-i\pi l/\lambda_r} \frac{\sin \pi l/\lambda_r}{\pi l/\lambda_r}, \tag{3.15}$$

which is the square root of the form factor (see the first factor in Eq. 2.34) up to a phase factor.

Similarly, the initial condition for the energy modulation due to a linear energy chirp from γ_0 to γ_{max} occurring over the bunch length l is with

$$\delta E = \frac{\gamma_{max} - \gamma_0}{\gamma_0}, \tag{3.16}$$

$$Z_0 = \frac{1}{l}\int_0^l e^{-ikz}\frac{\delta E z}{l}\mathrm{d}z. \tag{3.17}$$

This evaluates to

$$Z_0 = \frac{i\delta E}{2\rho\pi l/\lambda_r} e^{-i\pi l/\lambda_r}\left(e^{-i\pi l/\lambda_r} - \frac{\sin \pi l/\lambda_r}{\pi l/\lambda_r}\right), \tag{3.18}$$

which will be used later in analyzing the experimental data.

Another step in linking the one-dimensional theory to experiment is to convert the one-dimensional solution to three-dimensions. One way to do this [30] is to consider that the theory has found a Fourier amplitude E_{r0} for a particular frequency ω_r, which can be interpreted in three-dimensional Fourier space by considering the solution to be in the volume occupied by the beam, with periodic boundary conditions. Then Parseval's theorem will give

$$\mathcal{E} = \epsilon_0 \int |E(\vec{k})|^2 \frac{V}{(2\pi)^3}\mathrm{d}^3k = \epsilon_0 \frac{V}{(2\pi c)^3}\int |E(\vec{k})|^2\omega^2 \mathrm{d}\omega \mathrm{d}\Omega_{\vec{k}}, \tag{3.19}$$

where $\mathcal{E}$ is the volume energy density in beam volume V and $V/(2\pi)^3$ is the density of states in k-space. In the forward direction then,

$$\left.\frac{\mathrm{d}^2 I}{\mathrm{d}\Omega \mathrm{d}\omega}\right|_{\theta=0} = \epsilon_0 \frac{V^2}{(2\pi c)^3}\omega^2 |E(\omega)|^2, \tag{3.20}$$

where $|E(\omega)|^2$ is given by the one-dimensional theory. This allows comparison with the coherently-enhanced version of Eq. 2.12:

$$\left.\frac{\mathrm{d}^2 I}{\mathrm{d}\Omega \mathrm{d}\omega}\right|_{\theta=0} = N_e^2 f(\hat{\mathbf{z}}\omega/c)\frac{q^2\gamma^2N^2}{4\pi\epsilon_0 c}F_n(K)\frac{\sin^2[N\pi(\omega/\omega_{10} - n)]}{\pi^2N^2(\omega/\omega_{10} - n)^2} \tag{3.21}$$

where $n = 1, 3, 5\ldots$ is the harmonic number. The low particle density ($\rho \to 0$) limit of the FEL equations (3.8) agrees with Eq. (3.21) with $n = 1$ [30].

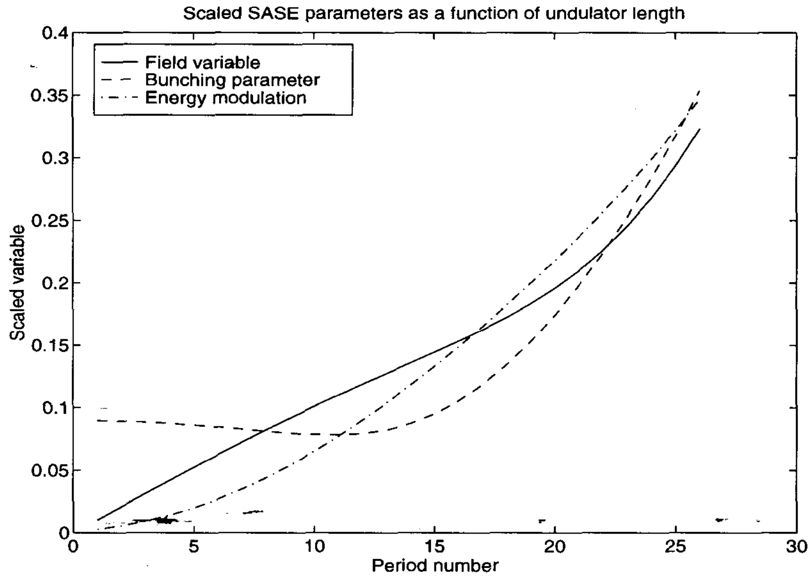

Figure 3.1: Calculated magnitude of variables X, Y, and Z vs. undulator length at the resonant wavelength. The bunch is of length 180 μm and radius 1 mm and contains 2×10^8 electrons of energy $\gamma_0 = 29.35$. The wiggler is at strength $K = 0.6$ and has 26 periods each of length $\lambda_0 = 0.077$ m. The initial conditions are that $Z_0 = 0$ and $X_0 = 0$; Y_0 is the square root of the form factor at the radiation frequency ω_r.

3.1.2 Numerical Evaluation

The theory can now be evaluated for the SUNSHINE experiment, and its output compared with the superradiant formulas of the preceding chapter. As in the previous chapter, numerical calculations are made for a cylindrical bunch of length 180 μm and radius 1 mm. The bunch contains 2×10^8 electrons of energy $\gamma_0 = 29.35$. The wiggler is at strength $K = 0.6$ and has 26 periods each of length $\lambda_0 = 0.077$ m. The initial conditions are that $Z_0 = 0$ and $X_0 = 0$; Y_0 is taken from the form factor at the radiation frequency ω_r as $Y_0 = \sqrt{f(\omega_r/c\hat{\mathbf{z}})}$. The scaling parameters at frequency ω_{10} are $\delta = 0$, $\rho = 0.009423$, $\sigma = 0.04825$, $\tau = 0$ to 3.079 over 26 periods of undulator, $X_0 = 0$, $Y_0 = 0.08986$, and $Z_0 = 0$. The resulting behavior of the SASE variables X, Y, and Z is shown in Fig. 3.1.

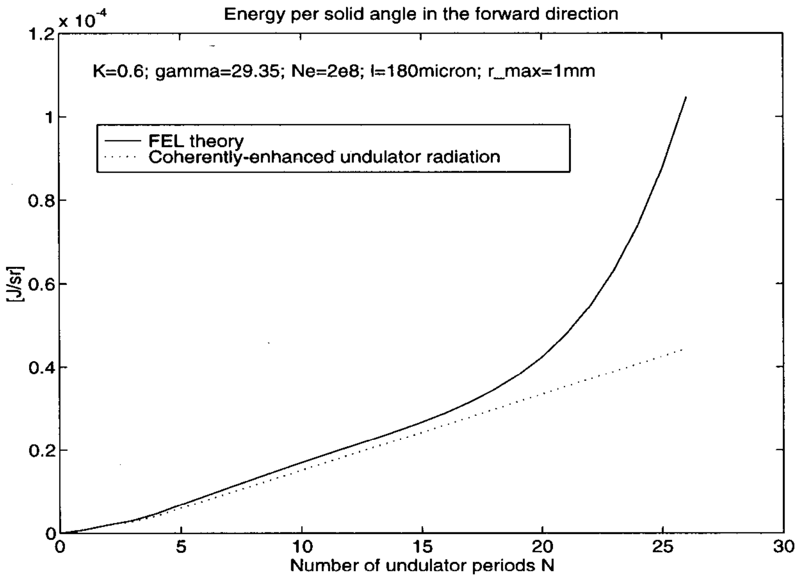

Figure 3.2: Frequency-integrated energy per solid angle radiated in the forward direction as a function of undulator length calculated from Eq. (3.8) compared with coherently-enhanced undulator radiation calculated from Eq. (3.21) with n=1. The non-linearities for $N < 5$ occur because when the undulator is short the radiation spectrum becomes dominated by the form factor of the bunch rather than the undulator response, as discussed in Section 2.3.1.

The calculated energy per solid angle in the forward direction, after integrating over frequency, is plotted in Fig. 3.2, along with the coherently-enhanced Eq. (3.21). The FEL theory agrees with the superradiant calculation at the beginning of the undulator, but diverges from it and predicts exponential increase in energy towards the end of the undulator.

Chapter 4

Experimental Setup

The previous two chapters have described the simplest theory of what might happen as a short bunch travels through the undulator: one expects to see superradiant coherent emission depending linearly on the length of the undulator, and possibly the startup of the SASE process which would give a measurable greater-than-linear radiated energy versus length. The present chapter describes the setup of the experiment and the properties of the electron beam.

4.1 The SUNSHINE facility

The SUNSHINE facilty consists of the following main components, as shown in Fig. 4.1:

- A thermionic-cathode rf gun [36] provides a 2.5 MeV electron beam.
- An alpha magnet bends the beam about 270 degrees and allows energy collimation via beam scrapers at the high-dispersion point.
- A SLAC 10-foot linac section is phased to accelerate the beam to about 15 MeV for undulator radiation, although up to about 32 MeV is possible.

- A planar 26-period permanent magnet undulator creates superradiant radiation.
- Immediately after the undulator, an Al screen reflects the undulator radiation out of the vacuum chamber to allow measurements of the spatial diatribution.
- Downstream of the electron beam dump, an Al-coated Mylar film reflects the radiation into a Michelson interferometer for spectral analysis.

The thermionic rf gun, electron-beam optics, alpha magnet, linac, and the beam dynamics of bunch compression are discussed at length in the references by Borland [36] and Kung [37]. In particular reference [36] describes the experimental setup in detail. Articles [38] and [39] also discuss the facility.

4.1.1 Rf Gun and Alpha Magnet

The features necessary to produce short bunches begin with the rf gun which is adjusted (run at about 2 MW input power) to produce an ≈ 2.5 MeV beam in which there is a strong, almost linear, energy-time correlation, with first particles exiting having the highest energy. The alpha magnet makes the higher energy particles travel longer paths and reverses the energy-time correlation so that the higher energy particles are later in time. As the beam drifts, the higher energy particles eventually catch up to the lower-energy particles and a short bunch is formed. Energy collimation in the alpha magnet removes particles which do not contribute to the short bunch. The rf gun and the longitudinal dynamics of the beam have been extensively simulated by Michael Borland [36] and Pam Kung [37], using MASK to model the gun and then using `elegant` [36] or `longi` [37] to track the MASK output particles through the rest of the beam line. The simulation results of `longi` shown in Figure 4.2 illustrate the bunching process — note the change of scale in the figure.

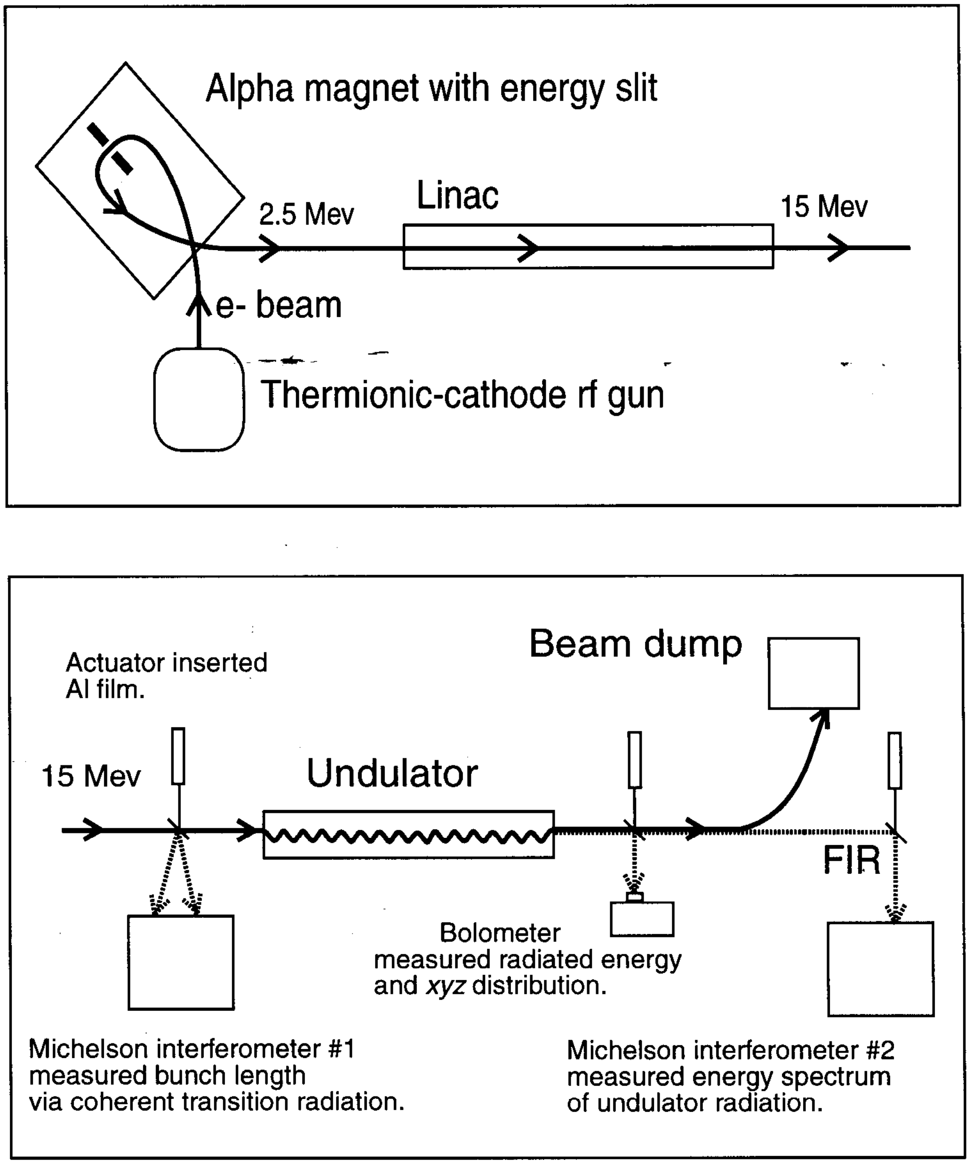

Figure 4.1: Block diagram of the SUNSHINE facility.

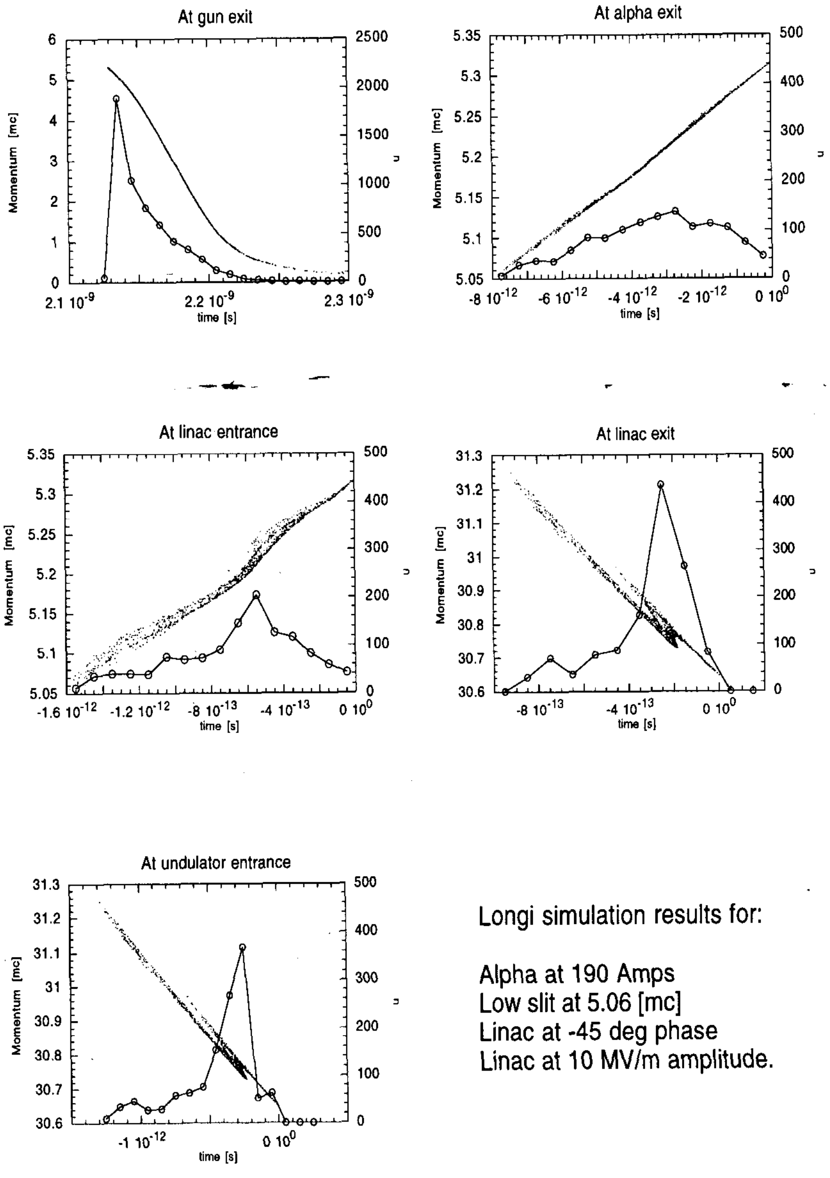

Longi simulation results for:

Alpha at 190 Amps
Low slit at 5.06 [mc]
Linac at -45 deg phase
Linac at 10 MV/m amplitude.

Figure 4.2: Simulation of bunch compression for superradiant undulator radiation at SUNSHINE. The dots show the energy vs. time distribution of the simulation macro-particles. The solid line with circles shows the projection onto the time axis.

4.1.2 Linac

The beam can be accelerated up to as much as about 32 MeV in the linac section, which is a standard SLAC 10-foot section [40] powered by about 14 MW of 2856 MHz rf power. There are two effects which must be considered concerning the high-current non-ultra-relativistic beam from the rf gun. First, since the beam has some velocity spread upon entering the linac and the acceleration is not infinite within the linac, the longitudinal dynamics of the beam becomes important, particularly when the beam is run far off the crest of the rf, as is necessary to achieve low energies. Secondly, since the linac requires a finite time to fill with rf energy, which the beam can remove almost instantaneously, beam-loading effects are important. The first effect causes bunch lengthening/compression and energy spread within the micropulse. The second effect causes a large energy spread across the macropulse.

4.1.3 Undulator

The undulator used in this experiment is a planar 26-period permanent magnet design with an adjustable gap. The samarium-cobalt ($SmCo_5$) permanent magnets are arranged in a $M = 4$ block per period Halbach configuration [41] with filling factor $\epsilon = 1$, as shown in Fig. 2.1. The magnetic field has the form [41]

$$-B_z + iB_y = 2iB_r \sum_{\mu=0}^{\infty} \cos\left[mk_0(z+iy)\right] e^{-mk_0 g/2} \left(1 - e^{-mk_0 h}\right) \frac{\sin(m\epsilon\pi/M)}{m\pi/M} \ , \quad (4.1)$$

where g is the (full) gap distance, $h = \lambda_0/4$ is the height of the permanent magnets, B_r is the remnant field of a single magnet, and $m = 1 + \mu M$. The vertical field due to the dominant $\mu = 0$ term is

$$B_y = 1.4263 B_r e^{-\pi g/\lambda_0} \cosh(k_0 y) \cos(k_0 z) \quad (4.2)$$

which in the $y = 0$ plane simplifies to

$$B_y = B_0 \cos(k_0 z). \quad (4.3)$$

As shown in Fig. 2.1, the undulator begins with a half-block at the phase of maximum field. Defining $z = 0$ at this point and neglecting fringe-field effects, the field does indeed depend on z as $B_y = B_0 \cos(k_0 z)$.

For the SUNSHINE undulator [17]

$$B_0 = 13.1 e^{-\pi g/\lambda_0} \text{ [kG]}, \tag{4.4}$$

the period is $\lambda_0 = 7.7$ cm and the gap is adjustable from 8 cm to 2.5 cm, so B_0 varies from 0.050 kG to 4.72 kG. The strength parameter K, given in practical units by

$$K = 0.0934 B[\text{kG}]\lambda_u[\text{cm}] \ , \tag{4.5}$$

can be varied from 0.36 to 3.4.

In order that the undulator introduce no change in angle or transverse position of the beam exiting the undulator as compared with entering the undulator, the following conditions must be met:

$$\int_0^L B_y(z)\mathrm{d}z = 0 \quad \text{and} \quad \int_0^L \left[\int_0^z B_y(u)\mathrm{d}u\right] \mathrm{d}z = 0. \tag{4.6}$$

The first condition guarantees that the change angle is zero, the second that the change in offset (*ie* the integral of the angle) is zero. The condition of no net angle is met by using an integral number of undulator periods as then obviously

$$\int_0^{N\lambda_0} B_0 \cos(k_0 z + \phi_0) dz = 0.$$

Here ϕ_0 is the phase of the undulator where the beam enters. The condition of no net offset is met by having the beam enter at the phase of field maximum (*ie* $\phi_0 = 0$) as then

$$\begin{aligned}
\int_0^{N\lambda_0} \int_0^u B_0 \cos(k_0 z) \mathrm{d}z \mathrm{d}u &= \int_0^{N\lambda_0} \frac{B_0}{k_0} \left[\sin(k_0 u) - \sin(0)\right] \mathrm{d}u \\
&= \int_0^{N\lambda_0} \frac{B_0}{k_0} \sin(k_0 u) \mathrm{d}u \\
&= 0,
\end{aligned}$$

as is true for the SUNSHINE undulator, when fringe-field effects are negligible.

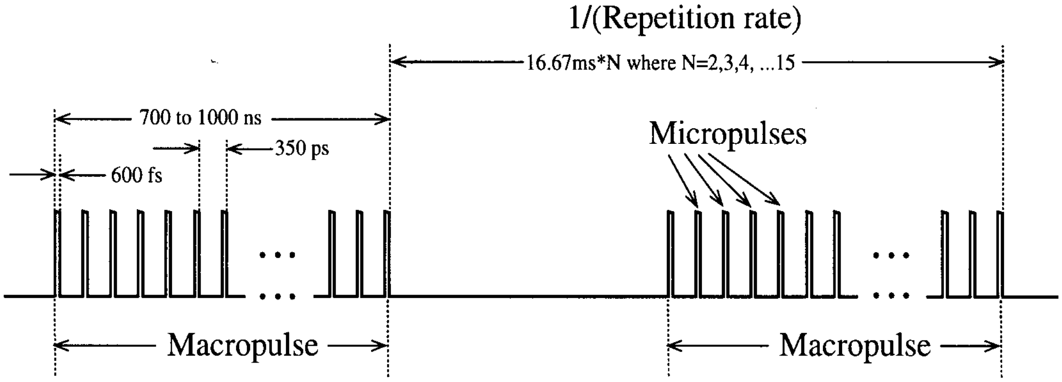

Figure 4.3: The time format of the SUNSHINE electron beam.

4.2 The Electron Beam

The properties of the electron beam are typically separated into logitudinal and transverse categories where the momentum (or energy) and z-position, or equivalently time, are the longitudinal variables and the offsets and angles are the transverse variables.

4.2.1 Time Format

The time format of the electron beam produced at SUNSHINE for the superradiant undulator work is shown in Fig. 4.3. The beam consists of an ≈ 1 μs long macropulse at a repetition rate of from 4 Hz to 30 Hz. The repetition rate is determined by dividing the 60 Hz power-line frequency, to which the beam pulse is synchronized, by an integer from 2 to 15. The repetition rate was 15 Hz for much of the superradiant undulator work.

Each macropulse consists of a set of microbunches spaced at 350 ps (1/2856 MHz). The microbunches are not necessarily equally populated, as seen in Figure 4.4, which illustrates the measured macropulse current at the undulator. The measurement used the induced current in a ferrite-core toroid encircling the electron beam.

The superradiant emission is proportional to $\sum_j N_{ej}^2$, where N_{ej} is the number of

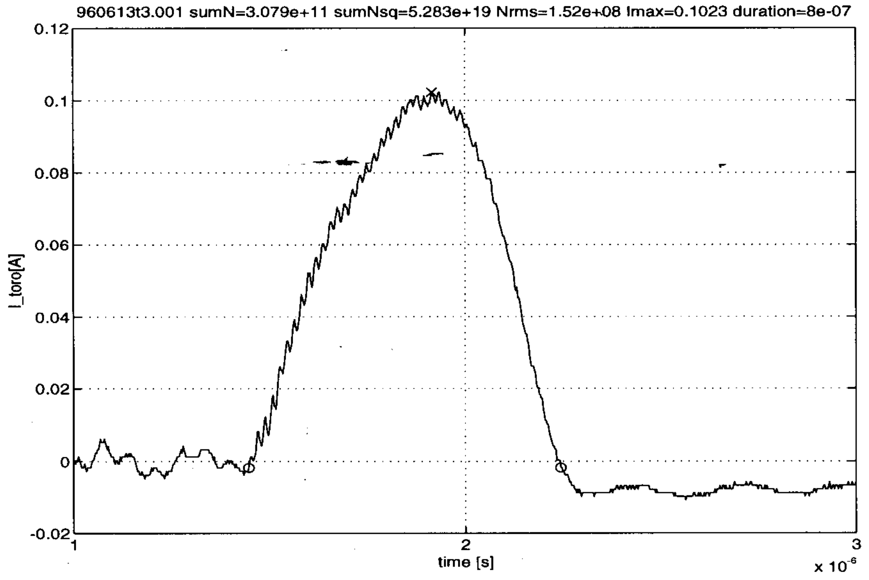

Figure 4.4: A measured SUNSHINE electron beam macropulse for superradiant undulator radiation. The parameters of this pulse are $\sum N_e = 3.08 \times 10^{11}$, $\sum N_e^2 = 5.28 \times 10^{19}$, $N_{rms} = 1.52 \times 10^8$, pulse duration = 800 ns, maximum current = 102 mA. There is electronic noise evident as the slight sawtooth on the leading edge of the waveform. The small circles denote the time window over which the pulse parameters were calculated, the small 'x' is the peak current.

electrons in the jth microbunch, and where the sum is over all the microbunches. Therefore the macropulse is characterized in this thesis by either $\sum_j N_{ej}^2$, or by the rms (root-mean-square) current value.

4.2.2 Bunch Form Factor

The microbunches have a time structure of their own, which is measured at SUNSHINE by interferometry of coherent transition radiation [3,42,22]. It is of course this structure that provides the superradiance and the seed for SASE. The references [42,22] describe the bunch-length-measuring system in detail. Here, the principles relevant to this thesis are briefly discussed.

The bunch structure is obtained from transition radiation that occurs when the electron bunch strikes a conductor. Imagining a single electron striking a perfect conductor, one sees that the (backward) transition radiation is mathematically equivalent to the radiation from the instantaneous longitudinal decceleration of the image charge, and is thus a δ-function in time. From the many electrons in a bunch the radiation would then be the sum of many such δ-functions leading to the conclusion that *the transition radiation is the time-replica of the electron bunch.*

Thus by optical methods applied to the transition radiation, the bunch structure can be determined. At SUNSHINE, a Michelson interferometer is used to study the transition radiation. The interferometer consists of a beam-splitter that creates two pulses whose relative times-of-arrival at the detector are adjusted by a moving mirror. The detector responds to the energy it receives, which is proportional to the square of the magnitude of the electric field; the phase information is lost. Therefore in principle, one cannot say with certainty what the bunch shape is from the interferogram, but it can be shown that (within a constant factor) *the Fourier transform of the interferogram is the form factor of the bunch.*

Figure 4.5 shows the measured and simulated form factors. The essential feature

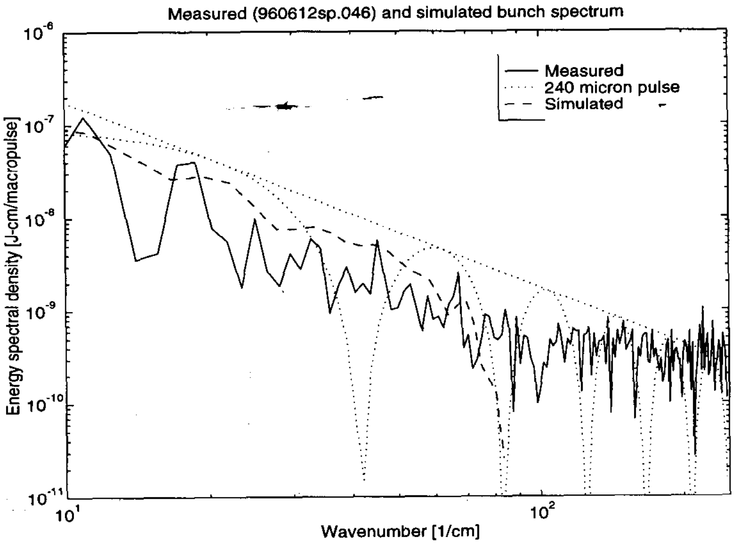

Figure 4.5: The measured and simulated bunch spectrum are compared to the spectrum expected from a 240-μm rectangular bunch. The envelope of the 240-μm bunch, defined as $\left(\frac{\lambda}{\pi l}\right)^2$ where $l \geq \lambda/2$, is a convenient approximation of the measured form factor.

is that the form factor falls off rapidly with wavenumber (wavenumber is defined as 1/wavelength), at a rate of about 20 dB/decade. That is, the form factor falls 2 orders of magnitude with every one order of magnitude increase in wavenumber. The simulated form factor at the undulator entrance, shown in Fig. 4.2, agrees with the main feature of the measurement: the form factor rolls off at about 20 dB/decade. This is what would be expected from an approximately rectangular pulse, and in fact a 240 μm rectangular pulse describes the measured form factor well, provided the zeros of the rectangular pulse's form factor are removed by taking only the envelope. This does not mean that the pulse is 240 μm long, but rather this is a simple approximation which describes the measured form factor:

$$f(k\hat{\mathbf{z}}) = (\frac{\lambda}{\pi l})^2 \text{ for } l \geq \lambda/2, \tag{4.7}$$

and

$$f(k\hat{\mathbf{z}}) = \frac{sin^2(\frac{\pi l}{\lambda})}{(\frac{\pi l}{\lambda})^2} \text{ for } l \leq \lambda/2, \tag{4.8}$$

where $l = 240$ μm.

It is also helpful to have a simple approximation of the bunch structure in the spatial domain. At SUNSHINE it is assumed that the bunch is either Gaussian or rectangular, making it possible to estimate its length from the FWHM (full-width half-maximum) of the interferogram. Assuming a rectangular distribution, the bunch length estimated from the FWHM of the interferogram is 180 μm. The difference between this number and the 240 μm above is easily explained as due to the non-rectangular shape of the real bunch, which may resemble the simulation shown in Fig. 4.2. As pointed out earlier, the spatial structure cannot be uniquely determined from the measured interferogram, but the form factor, as approximated in Eq. (4.7), is a reliable measurement.

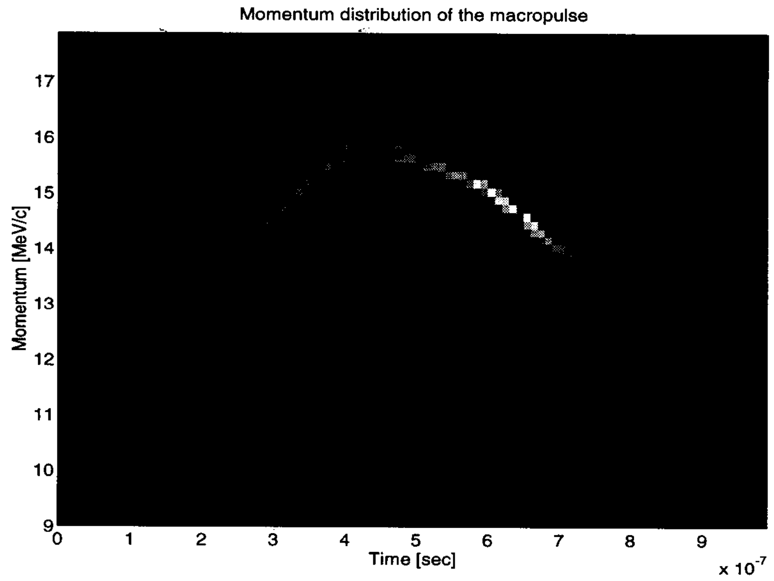

Figure 4.6: The measured energy versus time distribution of the SUNSHINE electron beam macropulse.

4.2.3 Energy

The energy spread of the beam over the macropulse is greatly affected by transient beam loading. The rf gun starts emitting before the linac has filled, so there is an energy ramp up at the beginning of the macropulse. Then the beam current draws energy from the linac and causes an energy droop at the end of the macropulse. The linac-filling time constant is about 800 ns, whereas the beam can extract energy almost instantaneously, so one expects that a constant current is required for several 800 ns fill times to achieve equilibrium. However, the SUNSHINE macropulse, as shown in Fig. 4.4, has large current variation within 800 ns, and therefore the macropulse has a large energy variation, as shown in the measurement of Fig. 4.6.

Figure 4.6 shows 'ghosts' at lower and higher energies than the real beam. These ghosts result from gaps at the edges of the energy collimator such that when the beam is directed towards the edge of the collimator, about 20% of the current finds its way to

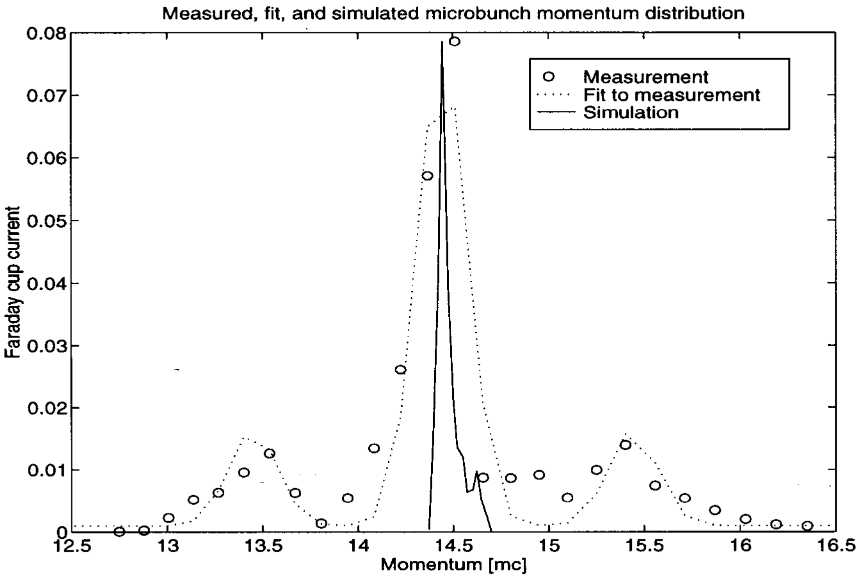

Figure 4.7: The energy versus time distribution of the SUNSHINE electron beam micropulse has $\sigma_{\delta E/E} = 0.9\%$. The measured satellites are an artifact of the momentum collimator. The simulated energy spread is the energy-shifted version of Fig. 4.2, and has $\sigma_{\delta E/E} = 0.2\%$.

the Faraday cup that measures the transmitted current. The ghosts can be eliminated from the data by fitting each time slice of data with a Gaussian distribution having two satellite Gaussians of 20% amplitude shifted in energy by ±7%. The standard deviation of the fit Gaussian then characterizes the energy spread of the microbunch.

Figure 4.7 displays the Gaussian plus satellites fit for the time slice with the highest peak current. This 10 ns time slice has a standard deviation of energy of 0.9%, which includes broadening due to the ±0.5% aperture of the collimator. Taking the collimator as a Gaussian aperture of $\sigma_{eff} = 1\%/\sqrt{2\pi}$ gives $\sigma_E = \sqrt{0.9^2 - 0.4^2} = 0.8\%$ as the measured energy spread of the micropulse. This measurement is an overestimate since the collimation is not perfect and appears to let twice as much current to the Faraday cup than would be expected from a hard-edge collimator model.

The measured energy spread is much larger than the about 0.2% simulated energy spread. It is not possible to say from the measurement whether the micropulse energy spread is correlated or random, but simulations suggest a correlated energy spread.

4.2.4 Transverse Emittance

At the time of writing the transverse structure is the least-measured feature of the SUNSHINE electron beam. This is because the large variation in energy over the macropulse (see Fig. 4.6) makes it difficult to interpret measurements made with the relatively slow phosphor screens [1]. However previous measurements done on a similar setup at SSRL have shown a normalized 1-σ emittance of the microbunch of about 20π mm-mrad [36].

In this thesis, simulation results combined with phosphor screen measurements before and after the undulator are used to characterize the transverse size of the bunch through the undulator. Despite the above 20π mm-mrad emittance measurement at SSRL, TRANSPORT runs corresponding to a 5π mm-mrad [37] microbunch yield reasonable agreement with the observed beam sizes at the entrance and exit of the SUNSHINE undulator. This may be because large offset particles are being scraped within the linac section, effectively reducing the emittance of the transmitted beam.

The measured electron beam transverse full widths were 2.9 mm horizontal and 2.5 mm vertical at the phosphor screen before the undulator and 4.5 mm horizontal and 1.9 mm vertical at the screen after the undulator, which are comparable to 4σ where σ is from TRANSPORT output shown in Figs. 4.8 and 4.9. From TRANSPORT, the average transverse sizes of the beam within the undulator are about $\sigma_x = 0.6$ mm and $\sigma_y = 0.4$ mm. Taking $\sigma_r = 0.5$ mm, the beam can be modelled as a cylinder with a

---

[1] Work is underway on a wire-scanner system that will be able to resolve the details of the microbunch at SUNSHINE.

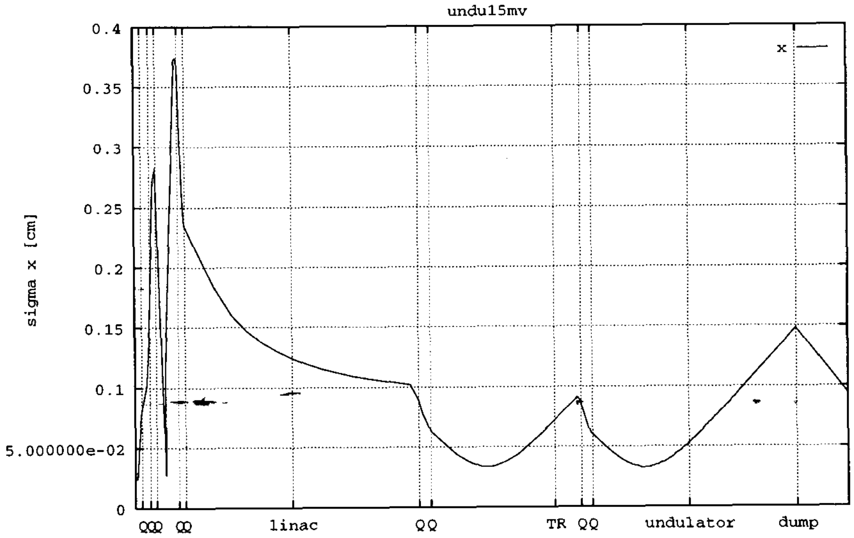

Figure 4.8: Transport simulation of σ_x.

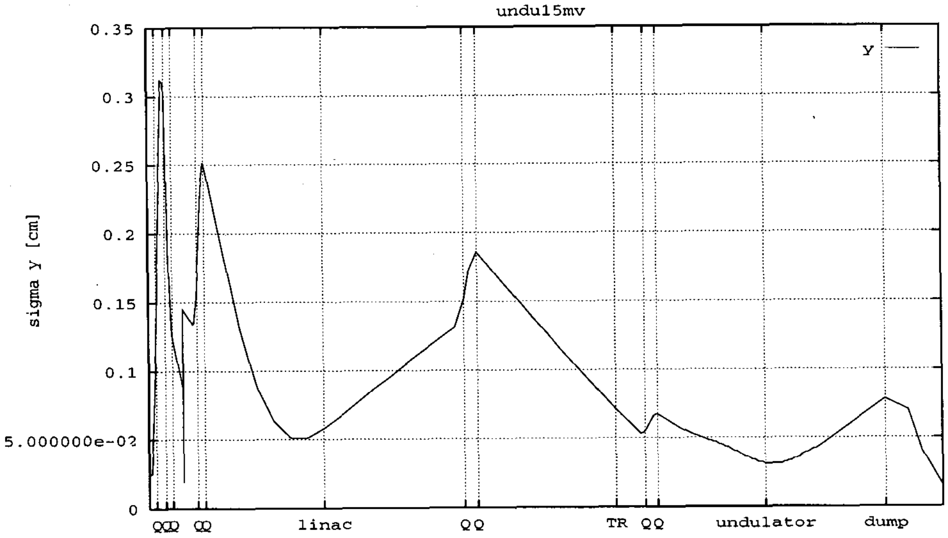

Figure 4.9: Transport simulation of σ_y.

radially Gaussian density distribution where the distance from the center (maximum density) to the $1/e^2$ point is 1 mm. This 1 mm radius contains 86% of the electron beam. The average angular spreads from TRANSPORT are $\sigma_{x'} = 0.5$ mrad and $\sigma_{y'} = 0.5$ mrad.

4.3 Instrumentation

A detailed schematic of the setup to measure the undulator radiation is shown in Fig. 4.10. Starting from the undulator itself (17), the first feature is a travelling steering magnet (18) to kick the beam out of the undulator chamber and thus allow measurements of the radiated energy as a function of effective undulator length. The magnet consists of two air-core coils of about 100 turns powered at 5 amps and producing a measured $\int Bdl$ of 2 kG-cm (integrated over about 20 cm) at the center of the undulator chamber. This is enough to kick the beam by an angle of $1/\gamma$, and thus separates the beam and the radiation by the end of the corrector. In this project the beam is considered dumped at the downstream end of the corrector. The corrector location is monitored by a TV camera (19) and the position is changed remotely by an electric motor.

The undulator is immediately followed by a screen that reflects the radiation out of the vacuum chamber (22), through a high-density polyethelyne (HDPE) window, and finally to a pyroelectric detector ('bolometer') mounted on a 3-dimensional translation stage (20) capable of over 1 m of longitudinal motion, approximately 4 inches of horizontal motion, and 2 inches of vertical motion. This allows measurement of the spatial distribution and divergence of the radiation.

In the forward direction after the undulator, the dump magnet (25) bends the electron beam down to the Faraday cup and the undulator radiation continues to an

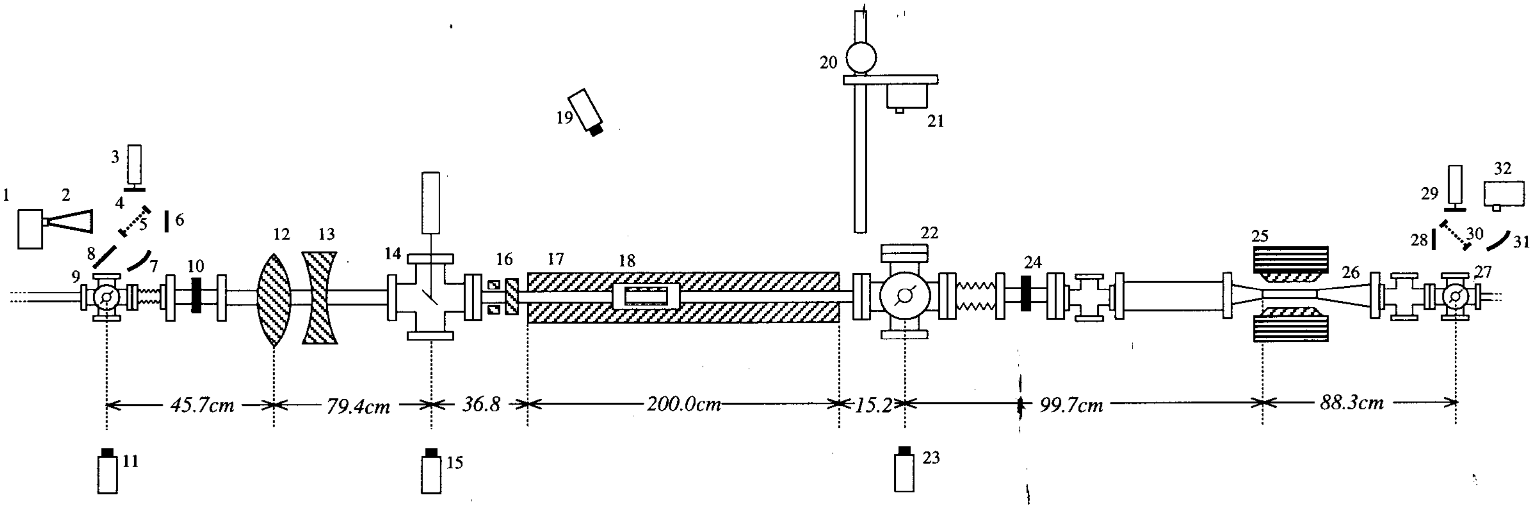

Component list:

1 - Bolometer.
2 - Copper condensing cone.
3 - Precision translation stage.
4 - Moving mirror.
5 - Mylar beam-splitter.
6 - Stationary mirror.
7 - Paraboloidal mirror.
8 - Flat mirror.
9 - 5-way cross allows insertion of transition radiator and phosphor screen. Light exits out a 3/4 inch diameter 1mm thick high-density polyethlyene (HDPE) window.
10- Toroid 3 current monitor.
11- TV camera.
12- Q8 focussing quadrapole.
13- Q9 defocussing quadrapole.
14- 4-cross allows insertion of phosphor screen.
15- TV camera.
16- WV1 vertical and WH1 horizontal steering magnets.
17- 26-period 2-m long undulator.
18- Travelling horizontal steering magnet.
19- TV camera monitors postion of travelling steering magnet.
20- *XYZ* translation stage.
21- Bolometer.
22- 5-way cross allows insertion of mirror and phosphor screen. Light exits out a 1-1/4 inch diameter, 1mm thick HDPE window.
23- TV camera.
24- Toroid 4 current monitor.
25- Dump magnet deflects beam down to faraday cup dump/current monitor.
26- Dump chamber.
27- 5-way cross allows insertion of Al-coated Mylar film. Light exits out a 3/4 inch diameter 1mm thick HDPE window.
28- Stationary mirror.
29- Precision translation stage and moving mirror.
30- Mylar beam-splitter.
31- Parabaloidal mirror.
32- Bolometer.

Some relevant dimensions:

From radiator to HDPE window in cross (9):	7.3 cm
Optical path length from HDPE window in (9) to bolometer (1):	57.2 cm
Inner radius of undulator chamber:	1.0 cm
From radiator to HDPE window in cross (22):	13.7 cm
Dump chamber horizontal aperture:	2.5 cm
From radiator to HDPE window in cross (27):	7.3 cm
Optical path length from HDPE window in (27) to bolometer (32):	32.4 cm

Superradiant Undulator Radiation Experimental Setup June-Aug. 96

This drawing is not to scale.

Figure 4.10: Detailed schematic of the superradiant undulator radiation setup.

aluminum-coated Mylar film (27) which reflects the light into a Michelson interferometer (28–32), discussed in the next section. At this point there can be no interference from transition radiation and there is very little acceptance of synchrotron radiation from the dump magnet. Thus this Michelson is ideal for measuring the radiated energy as a function of undulator length.

Not shown in the figure is another screen 2 m downstream of the dump Michelson which was used for interferometry and xy measurements at various stages of the investigation.

4.3.1 Pyroelectric Detector and Electronics

The superradiant undulator radiation was measured using Molectron P1-65 room-temperature pyroelectric bolometers. These devices consist of a 5 mm active diameter $LiTaO_3$ crystal which expands when it absorbs energy. The crystal has net electric polarization, which changes as the crystal expands, giving a AC signal which is amplified by electronics [22] having a gain of from 1 up to 200 into a 50 Ω load and from 2 up to 400 into a high-impedance load. The relative spectral response of the detector is flat from at least 3 μm to about 100 μm according to the Molectron data sheet.

The responsivity of the detector is quoted by the manufacturer to be typically 25 V/W at 25 Hz at 632.8 nm and is measured by the manufacturer to be between 28 and 32 V/W at 15 Hz at 632.8 nm for the devices used in this work. In the factory calibration mode the response of the detector is given as

$$R_v[\mathrm{V/W}] = \alpha R_i \frac{R_E}{1 + j2\pi f R_E C_T} \frac{j2\pi f R_T H}{1 + j2\pi f R_T H} \tag{4.9}$$

where

R_i = current responsivity in A/W

α = absorption coefficient (assumed = 1 in calibration)

R_E = load resistor or feedback resistor in ohms ($10^8\Omega$)

f = frequency in Hz (15 Hz for factory calibration)

$C_T = C_D + C_{amp}$ in F in voltage mode (75 pF) and C_f in current mode

H = heat capacity in $J/{}^0$C ($R_T H = 1/\pi$ s)

R_T = thermal resistance in ^{0}C/W

Putting in the numbers at 15 Hz gives the calibration value of

$$(\alpha R_i)_{factory} = 0.37 \pm 0.02 \ [\mu\text{A/W}]$$

for the uncoated detectors used in this experiment, and

$$(\alpha R_i)_{cc,factory} = 0.61[\mu\text{A/W}]$$

for the detector equipped with a black absorbing coating. The manufacturer also directly quotes the typical current responsivity as

$$(R_i)_{datasheet} = 0.25 \ [\mu\text{A/W}]$$

so there are some discrepancies.

In any case it is necessary to calibrate the response of the entire detection system including electronics and cables, as the responsivity can easily be degraded by stray capacitance, and the electronic amplification can be degraded by the high output impedance of the FET included with the detector.

In this experiment the detectors respond to a 1 μs macropulse of radiation, which is much faster than the $R_E C_T = 10^8 \times 75 \times 10^{-12} = 7.5$ ms time constant. The

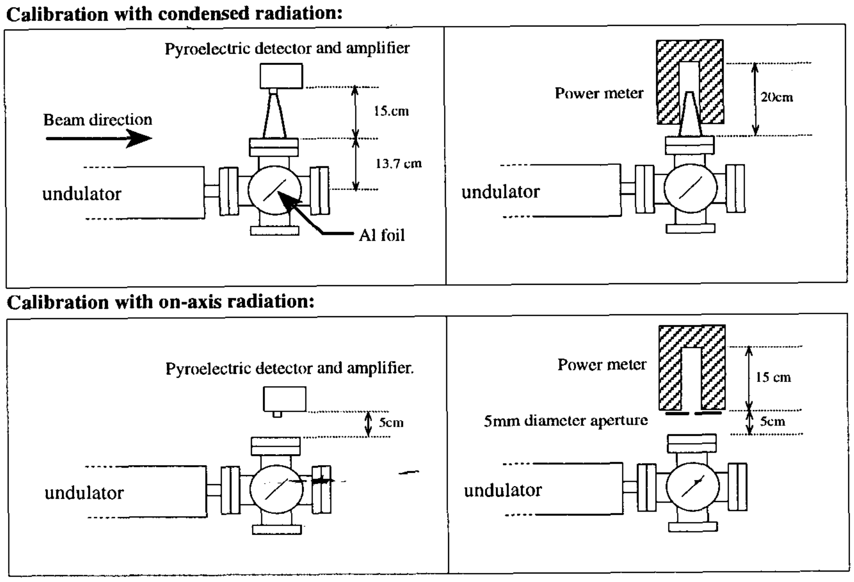

Figure 4.11: Detector system calibration setup.

response is then that the detector integrates the input radiation pulse over the entire macropulse with a voltage responsivity of

$$\begin{aligned}(R_V)_{factory} &= \frac{(\alpha R_i)}{C_T} \\ &= \frac{0.37 \times 10^{-6}}{75 \times 10^{-12}} \\ &= (4.9 \pm 0.3) \times 10^3 \text{ [V/J]}\end{aligned}$$

for the uncoated detector and

$$(R_V)_{cc,factory} = 8.1 \times 10^3 \text{ [V/J]} \tag{4.10}$$

for the coated detector according to the manufacturer's calibration at 632.8 nm, and 3.2×10^3 [V/J] if the manufacturer's data sheet number for the current responsivity is used.

The calibration was done at FIR wavelengths by comparing the signal from the pyroelectric detector and its electronics with the response of a Scientech laser power

170 μm	on-axis radiation	condensed rad.	units
power meter voltage	46.8 ± 1.5	558 ± 16	[μV]
power meter average power	0.498 ± 0.016	5.87 ± 0.17	[mW]
avg. energy per macropulse	49.8 ± 1.6	587 ± 17	[μJ]
uncoated pyroelectric	$(1.99 \pm 0.04)/20$	$(1.12 \pm 0.07)/1$	[V]/(amp gain)
coated pyroelectric	$(1.94 \pm 0.04)/20$	$(2.03 \pm 0.13)/2$	[V]/(amp gain)
uncoated calibration	2.00 ± 0.10	1.91 ± 0.17	[V/mJ]
coated calibration	1.95 ± 0.10	1.73 ± 0.16	[V/mJ]
overall calibration	1.9 ± 0.1		[V/mJ]

Table 4.1: Detector system calibration with 170 μm undulator radiation.

meter. The Scientech is basically a thermopile detector which has a quoted response of 93 μV/mW input power. That is, the Scientech produces 93 μV when it absorbs 1 mW of average power. This response was checked by inputting a known amount of electrical power, and measuring the Scientech's output. This calibration gave 95 μV/mW, verifying the Scientech was working correctly.

The undulator and beamline were set up to produce an $\approx$ 2 V/macropulse signal at $\sim$ 170 μm with the pyroelectric detector electronics at a gain of 2. The detector system was calibrated in two different ways with two different pyroelectric elements. The two calibration methods are shown in Fig. 4.11.

The first method was to use the high average power, at 170 μm, collected by a condensing cone, to compare the Scientech power meter measurement to the average power measured by the detector system (the macropulse energy multiplied by the repetition rate, which was 10 Hz for the calibration).

The second method did not use the cone; the power propagating directly to the 5-mm diameter active surface of the pyroelectric element was compared with the power allowed through a 5-mm diameter aperture to the power meter. The two pyrolelectric elements were a standard P1-65 detector and a P1-65 detector with a black absorbing coating.

The results of the calibration measurements at 170 μm are shown in Table 4.1

and show an overall responsivity of

$$(R_V)_{170\mu\mathrm{m}} = 1.9 \pm 0.1 \text{ [V/mJ]} \tag{4.11}$$

for the entire detection system using the nominal gain of the electronics. This is about a factor of two less responsive than would be expected from the manufacturer's claims for the uncoated detector, and a factor of four less than the claims for the coated detector.

The explanation for this discrepancy is that the detectors, and in particular the coated detector, are less sensitive to long (*ie* > 10 μm) wavelengths than to the optical wavelengths at which the manufacturer calibrates the device. A calibration done at 50 μm (Table 4.2) showed a much greater

$$(R_V)_{cc,50\mu\mathrm{m}} = 4.3 \pm 0.3 \text{ [V/mJ]} \tag{4.12}$$

responsivity for the coated bolometer, which is more consistent with the data sheet and with the 632.8 nm calibration. Calibrating the uncoated bolometer with respect to the coated one gives

$$(R_V)_{50\mu\mathrm{m}} = 2.5 \pm 0.5 \text{ [V/mJ]} \tag{4.13}$$

as the responsivity of the uncoated bolometer at 50 μm.

Neither of these calibrations is corrected for atmospheric absorption, which is assumed zero, or for the absorptivity of the Scientech power meter, which is assumed perfectly absorbing. Both of these factors reduce the amount of power the Scientech receives with respect to the pyroelectric, and thus make the pyroelectric appear more sensitive than it really is. Consequently the calibration numbers quoted in Table 4.1 and Table 4.2 represent upper limits on the responsivity of the pyroelectric detector. The calibrations do account for electronic effects, such as cable attenuation and scope calibration.

Typically the coated bolometer was used for forward and total power measurements while the uncoated bolometer was used in the Michelson interferometer. When

50 μm	condensed rad.	units
power meter voltage	51.8 ± 3.6	[μV]
power meter average power	0.546 ± 0.038	[mW]
equiv. energy per macropulse	54.6 ± 3.8	[μJ]
coated pyroelectric	$(4.65 \pm 0.24)/20$	[V]/(amp gain)
coated calibration	4.3 ± 0.3	[V/mJ]
uncoated calibration	2.5 ± 0.5	[V/mJ]

Table 4.2: Detector system calibration with 50 μm undulator radiation.

results are expressed "in bolometer volts", what is meant is that the measured voltage has been divided by the nominal gain of the electronics. The calibrated energy is recovered from "bolometer volts" by dividing by the calibration factor 4.3 ± 0.3 [V/mJ] for the coated detector and 2.5 ± 0.5 [V/mJ] for the uncoated when the wavelength is ≈ 50 μm, or by 1.9 ± 0.1 [V/mJ] when the wavelength is ≈ 170 μm.

4.3.2 Michelson Interferometer

To measure the frequency spectrum of the FIR radiation a Michelson interferometer was employed. The interferometer consisted of 1/4-mil Mylar beam splitter, a stationary Al-coated front-surface mirror, a moving Al-coated front-surface mirror stepped by a Newport motion-control system capable of sub-micron steps, and a paraboloidal mirror that focussed the re-combined light into the P1-65 detector. Since it had less frequency dependence, the uncoated detector was used in the Michelson.

The interferometer was not directly calibrated. However, the expected interferometer efficiency can be calculated from the optical properties of the Mylar beam-splitter. The effect of the beam splitter is calculated from the index of refraction of the Mylar, assuming no absorption in its 1/4 mil thickness. The energy, given unit incident intensity, transmitted to the detector when the two arms of the interferometer differ in path length by phase δ is given by [43]

$$I(\delta) = \frac{4\,(1+\cos\delta)\,(1-\cos\alpha)\,r^2\,(1-r^2)^2}{(1-r^2 2\cos\alpha + r^4)^2}\ , \tag{4.14}$$

with

$$r = r_{\perp} = \frac{\cos\theta_i - n_m\cos\theta_m}{\cos\theta_i + n_m\cos\theta_m} \tag{4.15}$$

for radiation polarized perpendicular to the plane of incidence with respect to the beam-splitter, and

$$r = r_{\parallel} = \frac{n_m\cos\theta_i - \cos\theta_m}{\cos\theta_i + n_m\cos\theta_m} \tag{4.16}$$

for radiation polarized parallel to the plane of incidence. Here $n_m = 1.61$ is the index of refraction of the Mylar as given by the manufacturer (Goodfellow), $l_m = 6.35 \times 10^{-6}$ m its thickness, and

$$\alpha = \frac{4 l_m \pi}{\lambda}\left(\frac{n_m}{\cos\theta_m} - \tan\theta_m\cos\theta_i\right)\ , \tag{4.17}$$

where $\theta_i = \pi/4$ is the angle of incidence and $\theta_m = \sin^{-1}(\sin\theta_i/n_m) = 0.454$ is the angle of transmission within the Mylar.

When $\delta = \pi$ the detector receives no energy, when $\delta = 0$ it receives the maximum, which is two times the efficiency of the interferometer M_{eff}. If a pure frequency sine wave is input into the Michelson then as the moving arm goes from $\delta = 0$ to $\delta = \pi$ the detected energy varies from 0 to $2M_{eff}$. That is

$$I(\delta) = 2M_{eff}\cos^2(\delta/2) = M_{eff}(1+\cos(\delta)), \tag{4.18}$$

where half of the energy in the interferogram is in the DC component, and the other half of the energy is in the harmonic component, and the efficiency is defined in terms of the harmonic component.

Figure 4.12 shows the interferometer efficiency including the beam splitter effect. Since the undulator radiation is polarized horizontally and the beam splitter is reflecting it horizontally, the radiation is polarized parallel to the plane of incidence

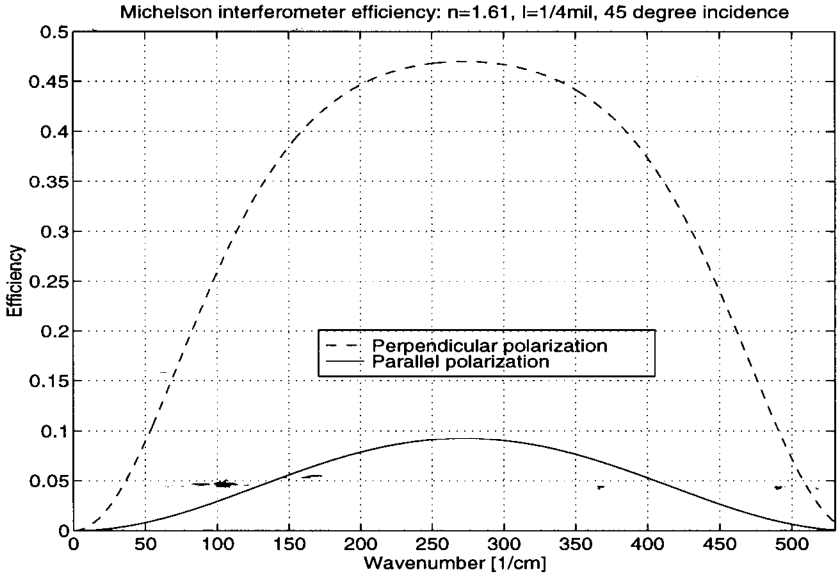

Figure 4.12: Michelson interferometer efficiency. The undulator radiation is polarized parallel to the plane of incidence, so the lower curve applies.

(the xz plane in this case) and so the lesser of the two curves shown applies, giving a maximum efficiency of less than 0.10.

Chapter 5

Characterization of Superradiant Undulator Radiation

The intent of the present chapter is to provide a reference of the FIR radiation properties which may be of interest to a potential user. This chapter catalogs the measured properties of the superradiant undulator radiation at SUNSHINE, beginning with proof of superradiance (and therefore coherence), and continuing with the energy spectral density, spatial distribution, angular divergence, and polarization. The time format of the radiation follows that of the electron beam as illustrated in Fig. 4.3.

5.1 Demonstration of Superradiance

In principle the demonstration of superradiance is straightforward: measure the radiated energy as a function of e-beam current and show that the radiated energy varies as the square of the charge. At SUNSHINE the only complication is that the device used to reduce the current is the energy collimator in the alpha magnet, which can potentially change the bunch structure by scraping off particles of a particular

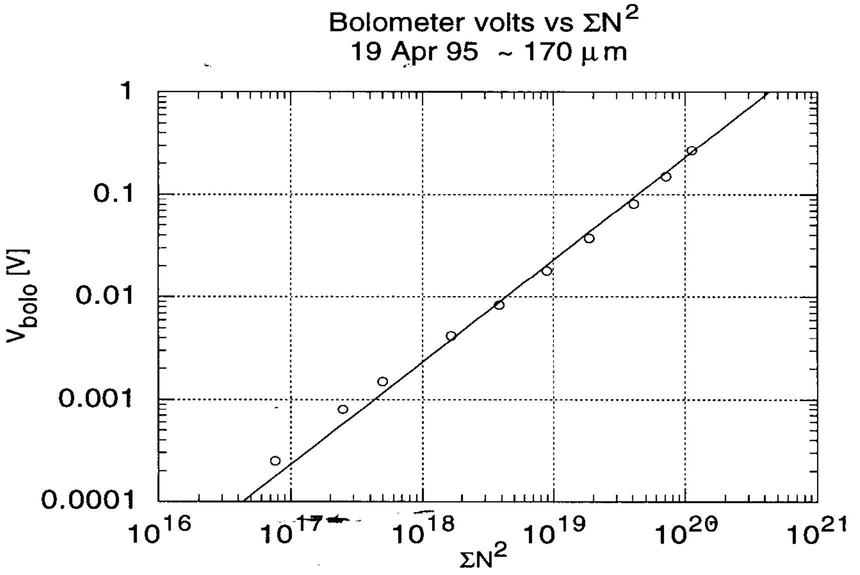

Figure 5.1: Bolometer voltage vs charge squared at ≈ 170 μm. The circles are the measurement, the line is a fit line of slope one, demonstrating the superradiance of the radiation.

energy that correspond to a particular position in the bunch. With the undulator radiation it was found that the high-energy scraper, which was normally not used, could produce a slow and relatively uniform change in current across the macropulse with a similar slow and steady change in the radiated energy. Reducing the current with the high energy scraper, the radiated energy tracked the sum of particles squared very linearly over three orders of magnitude in the bolometer voltage (volts to millivolts) as shown in Fig. 5.1. As usual in this thesis the sum of particles squared, $\sum N_e^2$, is taken over each microbunch as

$$\sum N_e^2 = \sum_{j=1}^{N_{mb}} N_{ej}^2,$$

where N_{mb} is the number of microbunches in the macropulse and N_{ej} is the number of particles in the jth microbunch.

In addition to the above measurement, superradiance is indicated by the amount

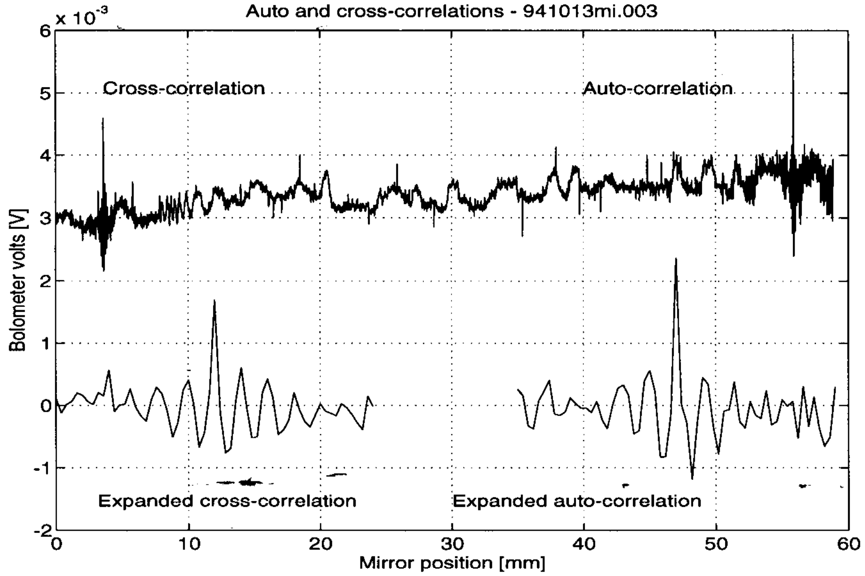

Figure 5.2: Measured auto and cross correlations demonstrating coherence of the radiation. This was one of the first measurements made with the superradiant undulator radiation, and required ~2 hours to complete. The stability of the radiation has been greatly improved since then, due to installation of a high-voltage regulator, temperature regulator for the rf gun, and active feedback directly stabilizing the current pulse out of the gun by adjustment of the thermionic cathode heating.

of energy in the radiation. The total incoherent radiation in the forward direction expected for the beam parameters of Fig. 5.1 ($K = 3.1, \gamma = 36, \sum N_e = 5.9 \times 10^{11}$) is given by Eq. (2.12) to be 13 nJ/sr which corresponds to 0.14 pJ into the 1×10^{-5} sr acceptance of the bolometer, or equivalently 0.26 nV of bolometer voltage. The measured 0.269 V is thus nine orders of magnitude greater than is expected from the incoherent radiation.

Additionally, since superradiant emission is by definition coherent, it should be possible to generate interference patterns of the radiation from one microbunch with the radiation from another, and this is shown in Fig. 5.2. In the figure, the autocorrelation refers to the interference of radiation from each microbunch with itself,

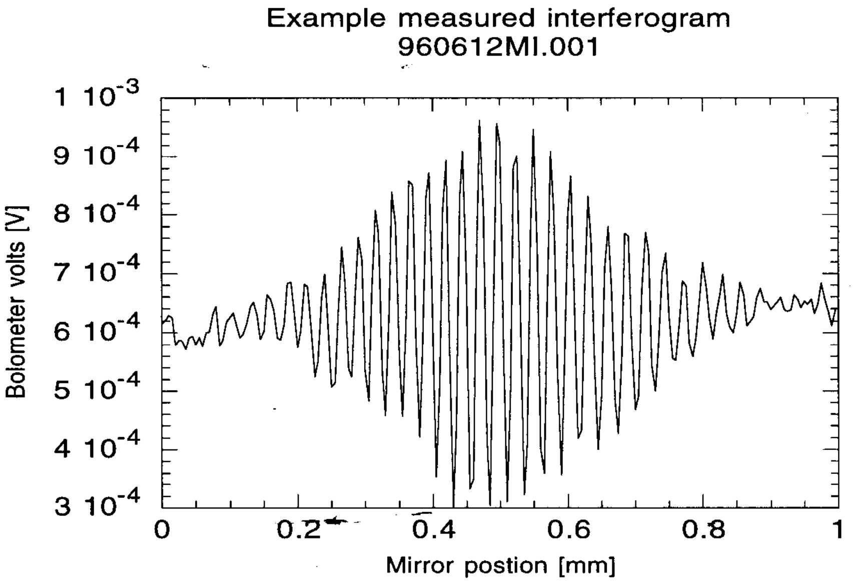

Figure 5.3: Example measured interferogram of 52 μm radiation.

and the cross-correlation is the interference of the radiation from each microbunch with the radiation from the adjacent bunch in the macropulse. The beamline was not fully optimized at the time the data was taken and there was drift (which has subsequently been greatly reduced) in the radiation signal, but even so one can clearly see that the cross-correlation exists and is basically the same as the autocorrelation, demonstrating that the radiation is coherent.

5.2 Energy Spectral Density

Potential users will be interested in the bandwidth of the undulator radiation, which in principle will not be less than $0.9/26 = 3.5\%$ FWHM from the 26-period undulator [1]. A typical interferogram and its corresponding spectrum are shown in

---

[1] For users interested in a *broadband* FIR source, work is progressing on a transition-radiation laser which is expected to produce a half-cycle of THz radiation at 10 MW peak power or greater [44].

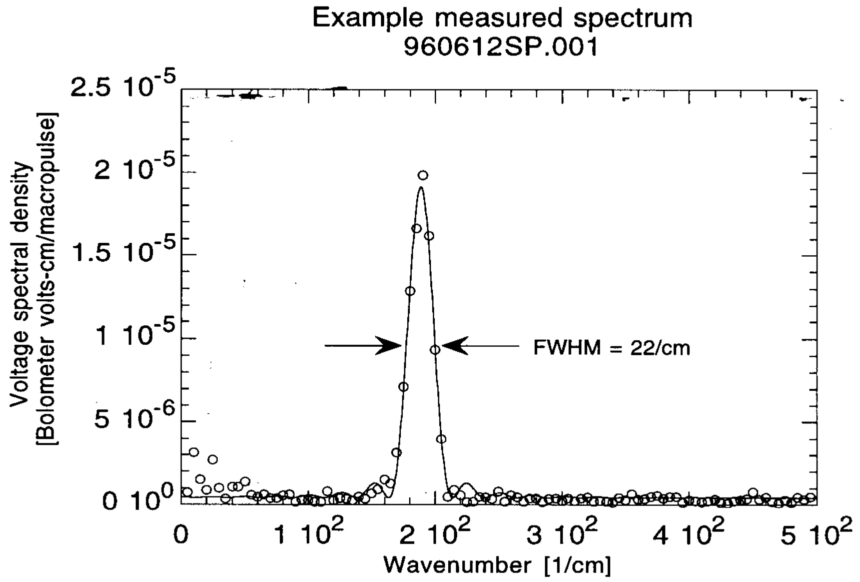

Figure 5.4: Example measured spectrum corresponding to the interferogram of Fig. 5.3. The circles are the measurement, the line is a fit of the $\sin^2 u/u^2$ function.

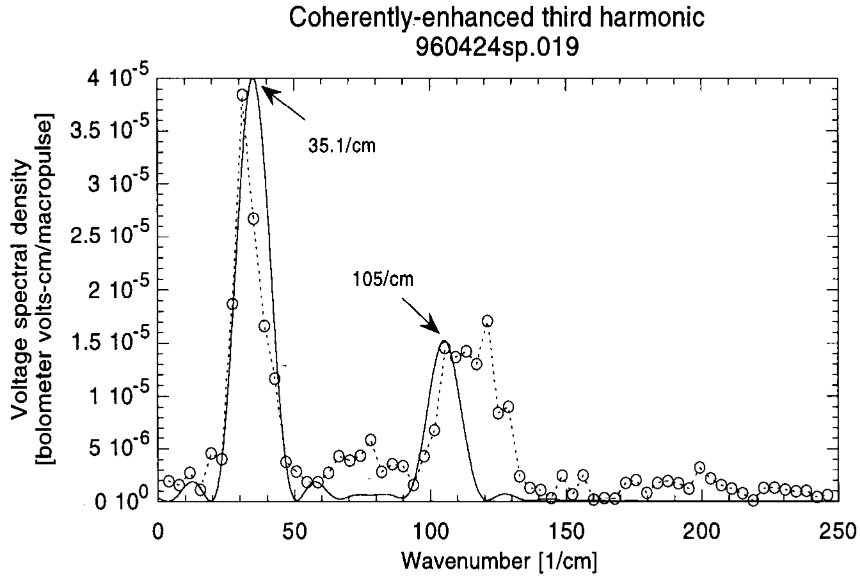

Figure 5.5: Coherent enhancement of the third harmonic. The circles connected by the dotted line are the measurement, the solid line is a fit of the fundamental plus third harmonic.

Figs. 5.3 and 5.4. The linewidth of the superradiant undulator radiation is broader than the theoretical minimum, for example 12% in Fig. 5.4. This is expected from the large energy variation across the electron beam macropulse, as shown in Fig. 4.6.

Figure 5.5 may be of interest to accelerator physicists as well as potential users: it shows coherent enhancement of undulator radiation at the third harmonic. The fundamental was tuned to a very long wavelength ($\sim 300\ \mu$m) in order to achieve this ($K = 3.2$).

5.2.1 Wavelength Tunability

One of the advantages of free-electron radiation sources is their tunability, and this is certainly true at SUNSHINE, where the superradiant undulator radiation is tunable over more than a factor of 5 in wavelength (from ~ 50 to $\sim 300\ \mu$m) merely

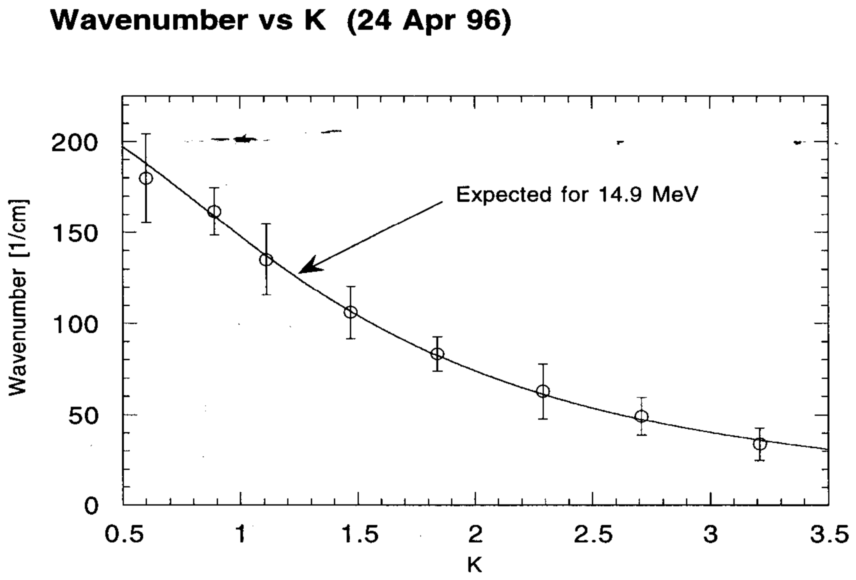

Figure 5.6: Wavenumber as a function of K. This data was taken with constant electron beam energy. The strength parameter K was changed by closing the undulator gap. The circles are the central wavenumbers, and the errorbars are the FWHM of the measurements.

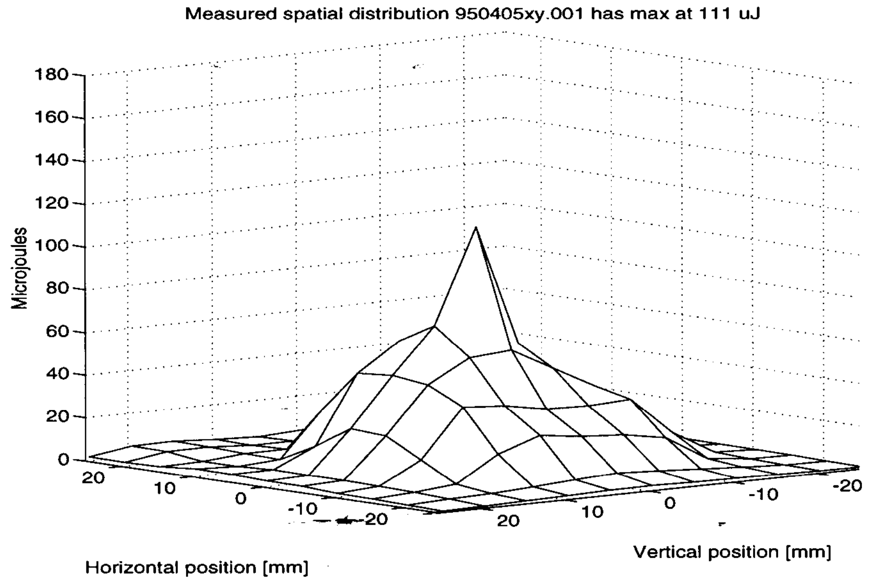

Figure 5.7: Spatial distribution at 170 μm. The distribution is measured 0.7 m from the undulator exit.

by changing the undulator gap, as shown in Fig. 5.6. Further tunability is possible by changing the electron beam energy.

5.3 Spatial Distribution

The spatial distribution of the superradiant undulator radiation was measured by (remotely) moving the pyroelectric detector across the radiation beam using a two-dimensional translation stage. From the downstream end of the undulator chamber, the radiation travelled 66 cm in vacuum, through a 1 mm HDPE window and then through 4 cm of air to reach the detector. The measured distribution when the beam was optimized for 170 μm radiation is shown in Fig. 5.7. This measurement corresponds to a total energy of 1.65 mJ in the macropulse; distributed over approximately 3000 microbunches, each of 26 cycles of 170 μm wavelength, it corresponds to 40 kW

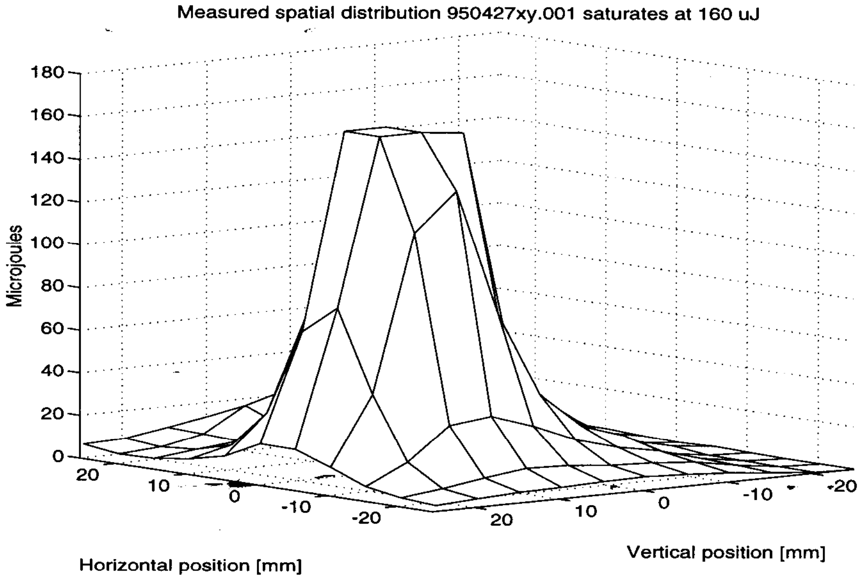

Figure 5.8: Saturated spatial distribution at 170 μm. The undulator chamber was effectively extended to the measurement point using light pipes to do this measurement. This can be compared directly with Fig. 5.7.

peak power averaged over all the microbunches.[2]

The highest measured power achieved was with a temporary setup in which a brass light pipe was used to effectively extend the undulator chamber to the HDPE window. The beam was set up as in Fig. 5.7 and a brass light pipe with 90 degree reflector was inserted into the undulator chamber and extended to the window where the distribution was measured. Vacuum difficulties led to abandoning this setup, but one measurement was completed as shown in Fig. 5.8. There are at least four points in which the electronics was completely saturated at 160 μJ, but even so 3.39 mJ of energy in the macropulse was measured, corresponding to over 80 kW of peak power, 3.2 kW average power over the 1.05 μs macropulse, and 102 mW averaged over all time (at 30 Hz repetition rate). These numbers would be higher if the amplifier had

---

[2] It has not yet become possible to measure the micropulse (radiated) energy directly at SUNSHINE; the macropulse energy is the measured quantity.

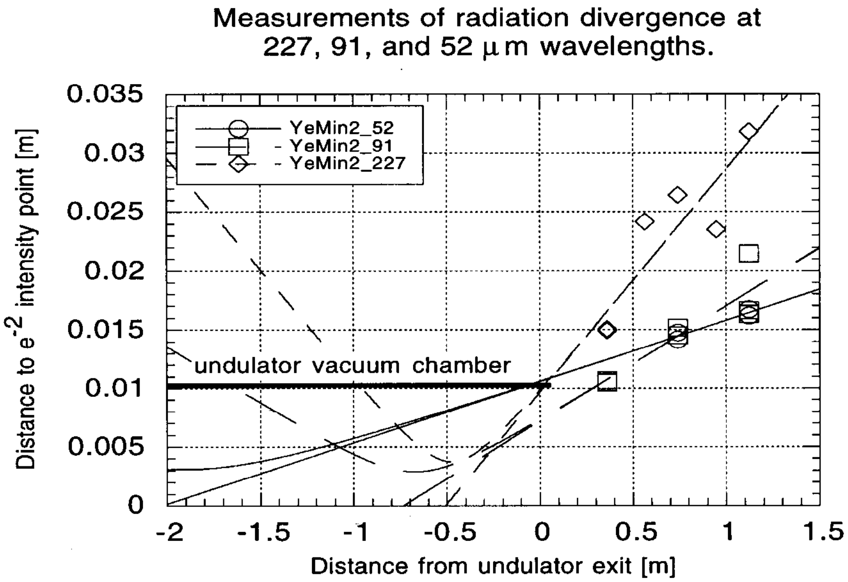

Figure 5.9: Measured angular divergence at 227, 91, and 52 μm. The symbols are measured radiation beam sizes defined as the distance from maximum intensity to $1/e^2$ of the maximum intensity. The lines are fits giving the angular divergences and waist positions. The bold line indicates the physical aperture of the undulator chamber.

not saturated.

At shorter wavelengths the spatial distribution is more sharply peaked, as shown in Fig. 5.10 taken at 55 μm wavelength. The full undulator (leftmost plot of the figure) produced 0.43 volts at the bolometer, which corresponds to 100 μJ. This was distributed over 2000 microbunches for a peak power of 10 kW over 26 cycles of radiation.

5.4 Angular Divergence

The angular divegence of the radiation exiting the undulator was measured by using an xyz translation stage (20) in Fig. 4.10. The spatial distribution was measured at several distances from the undulator, at several different radiation wavelengths.

K	wavelength [μm]	waist size [mm]	waist position [m]	Rayleigh length [m]	divergence [mrad]
0.6	52	3.1 ± 0.6	-1.91 ± 0.53	0.58 ± 0.23	5.2 ± 1.1
1.6	91	2.9 ± 0.6	-0.67 ± 0.32	0.29 ± 0.12	9.8 ± 2.2
2.8	227	3.8 ± 0.9	-0.48 ± 0.29	0.20 ± 0.09	19.0 ± 4.8

Table 5.1: Angular divergence of radiation. The waist position is measured from the downstream end of the undulator, where $z = 0$, and $z > 0$ in the radiation/beam direction. The values come from the fits shown in Fig. 5.9.

The pattern at larger distances z from the undulator was compared with that at the nearest location by doing a least-squares fit in which the near pattern was expanded in the x and y directions to match the far pattern. This uses the full information of the xy scan to determine the expansion.

The beam radius, defined as the distance from maximum intensity to $1/e^2$ of the maximum intensity, of the near data is scaled by the expansion factors from the fit to give the beam sizes as a function of distance, which can then be compared with the theoretical expansion equation for a Gaussian beam [6, page 665]:

$$W = W_0\sqrt{1 + z^2/z_R^2}, \tag{5.1}$$

where W_0 is the beam radius at the waist, defined as the distance from maximum intensity to $1/e^2$ of the maximum intensity, and

$$z_R = \pi W_0^2/\lambda \tag{5.2}$$

is the Rayleigh length, which is the distance from the location of the waist to the location where the Gaussian beam has expanded in area by a factor of two.

The measurements at 52 μm wavelength shown in Figs. 5.9 demonstrate a relatively small 5.2 ± 1.0 mrad divergence. As the wavelength increases by increasing K the angular divergence increases, becoming 9.8 ± 2.2 mrad at 91 μm, and 19.0 ± 4.8 mrad at 227 μm, as seen in Table 5.1.

5.4.1 Spatial Distribution vs. Undulator Length

Another way to try to measure the angular divergence is instead of moving the bolometer in z, move the undulator in z and do xy scans with the bolometer. Of course it would be impractical to physically move the undulator, but a steering magnet can be used to deflect the beam out of the undulator and this has a similar effect. Steering the beam out has the disadvantage of reducing the undulator length, and so the amplitude of the radiation source will changed as well as the distance. It would be expected though that the shape of the distribution would change, becoming broader as the undulator moves away from the detector. Suprisingly, this was not seen in the measurement.

The measurements of Fig. 5.10 taken at 55 μm show the spatial distribution of radiation versus undulator length. From the downstream end of the undulator chamber, the radiation travelled 29 cm in vacuum, through a 1 mm HDPE window and then through 18 cm of air to reach the detector. Undulator length was varied by deflecting the beam at the 8th, 15th, and 21st periods within the undulator using horizontal steering magnets.

The measured distribution is only slightly broader when the beam is deflected out at the 8th period as compared to propagating through all 26 periods. The FWHMs in the horizontal direction were 5.9, 6.5, 7.2, and 8.0 mm going from the full undulator (26-periods) through the 21,15, and 8-period long case, and the corresponding vertical FWHMs were 8.9, 10.5, 8.1, and 10.0 mm. While there is a trend in that the horizontal FWHM increased as the undulator 'moved away', a subsequent measurement did not reproduce this trend, but gave FWHMs of 8.2, 6.8 and 7.9 for 26, 9, and 5-period deflection locations. The shape of the measured distribution is basically unchanged as the beam is deflected out at different locations in the undulator. The main effect is just a change in amplitude of the measured distribution.

In the context of comparing measurements with theoretical expectations this result

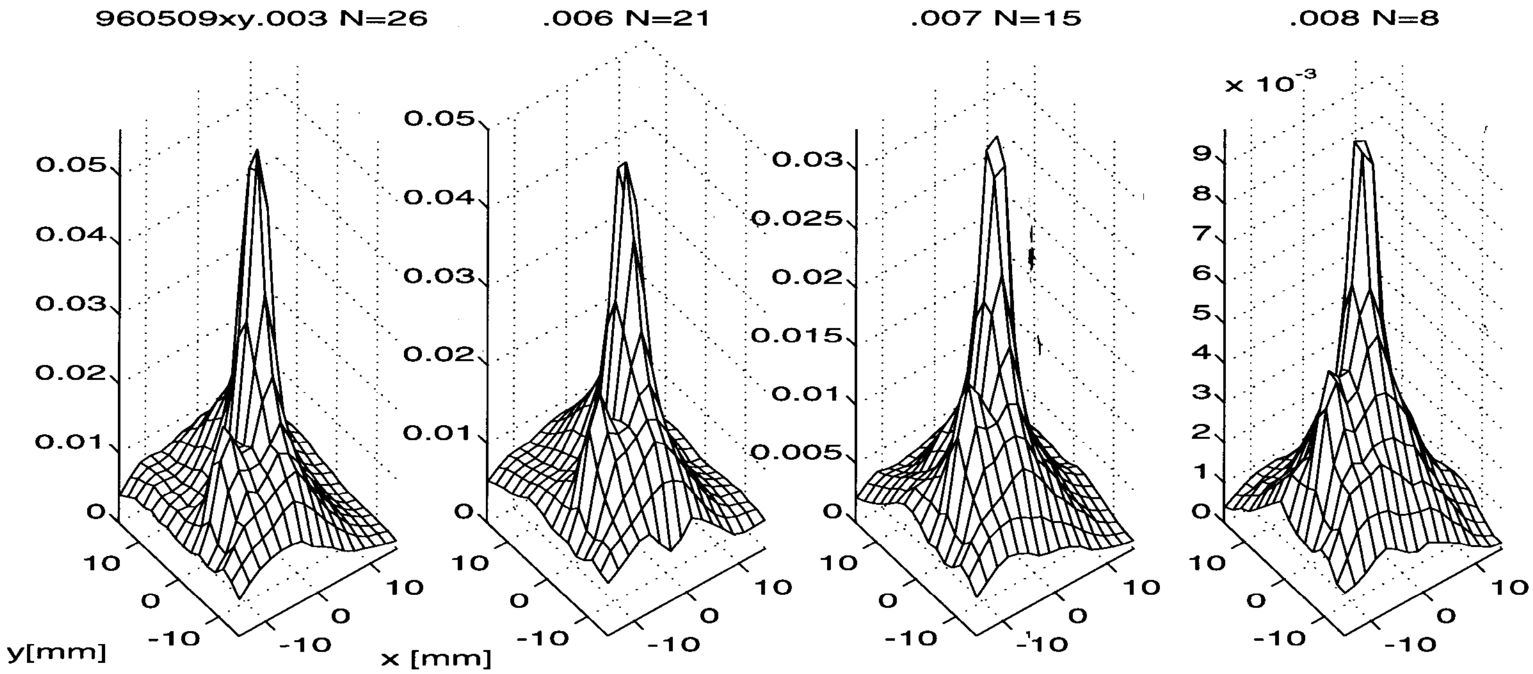

Figure 5.10: Measured spatial distribution as a function of undulator length. The units are bolometer volts per macropulse and can be divided by 4300 to convert to J/macropulse. The distribution is only slightly broader when the beam is dumped at the 8th period (rightmost plot) as compared to when the beam is propagating through all 26 periods (leftmost plot). Data taken 960509 at 55 μm wavelength.

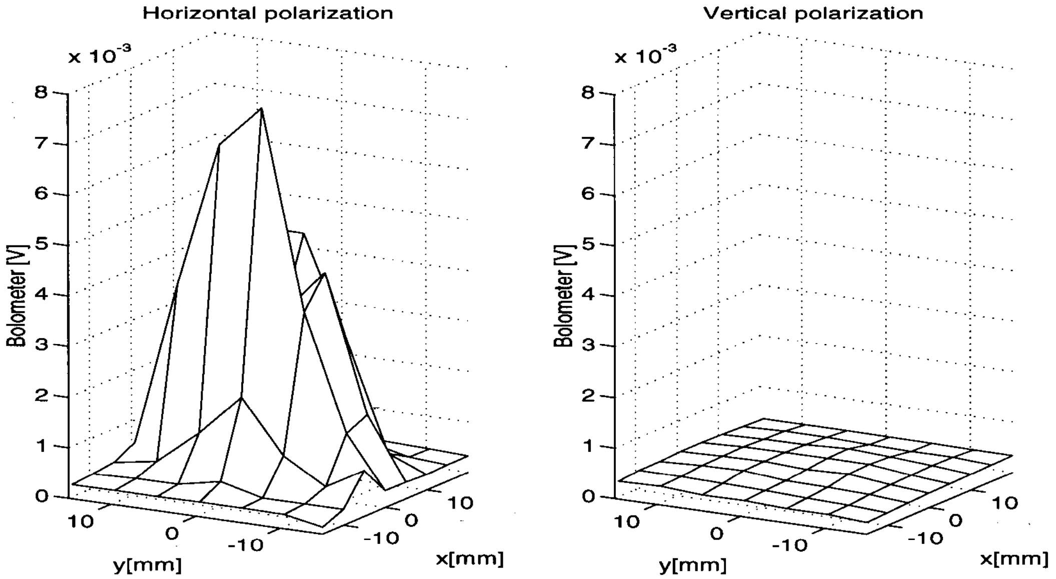

Figure 5.11: Horizontally and vertically polarized radiation components measured using a wire grid polarizer. The degree of polarization is greater than 90% at the peak.

is suprising, and will be refered to in a subsequent chapter. In the context of angular divergence measurements this result shows that the shape of the xy distribution cannot be used by itself to determine the angular divergence.

5.5 Polarization

The polarization of the superradiant undulator radiation was measured with a wire-grid polarizer manufactured by Graseby-Specac (Model IGP223). The polarizer consisted of 4 μm wire grid photo-lithed onto a polyethylene substrate. The spatial distribution was first measured with the wires oriented to pass the horizontal polarization, then measured again with the polarizer rotated 90 degrees. The results, after subtracting a uniform 300 μV background due to amplifier offset and stray ionizing radiation, are shown in Fig. 5.11. Figure 5.11 shows that the degree of horizontal (σ)

polarization, defined as $I_\sigma/(I_\pi + I_\sigma)$ where I_σ is the intensity of horizontally polarized radiation and I_π is the intensity of the vertically polarized radiation, is 95% where the beam is most intense. Overall, the measured polarization is 80%. This is not corrected for the 4% transmission (manufacturer data) of 'unwanted' radiation through the polarizer, compared to 80% transmission of 'wanted' radiation, which tends to reduce the measured polarization with respect to the actual polarization.

Chapter 6

Radiated Energy and Gain

In this chapter measurements of greater-than-linear growth of radiated energy as a function of undulator length are presented. The degree of superlinearity is used to characterize the 'gain' in a set of a dozen measurements. Gain lengths of five undulator periods are seen at 50 μm. A trend toward decreasing gain (longer gain length) with increasing radiated wavelength is seen.

Absolute measurements of forward-radiated energy show that at all wavelengths the forward energy is much greater than expected from superradiant undulator radiation alone. After correction for the efficiency of the Michelson interferometer, the measured energy per solid angle and the energy per solid angle expected from the single-pass FEL theory of Chapter 3 are compared absolutely in several of the gain measurements. It is found that the measured energy per solid angle versus undulator length, at 50 μm through 70 μm, is consistent with the gain expected from single-pass FEL theory. The larger-than-expected forward energy at 80 μm, and possibly at longer wavelengths, is *not* demonstrated to be the result of gain, but rather may be the result of waveguiding by the 1 cm radius vacuum chamber.

6.1 Gain Measurements

6.1.1 Method of Measurement

To measure gain, interferograms of the radiated field were recorded as the effective length of the undulator was varied. The bolometer voltage in the interferogram, which was proportional to the energy received in the interferometer, was observed to grow much greater than linearly with undulator length. In order to characterize this non-linearity the function

$$y(N) = m1 \times \left(e^{N/N_g} - 1\right) \tag{6.1}$$

was fit to the data. Here N is the length of the undulator measured in undulator periods, N_g is the gain length measured in undulator periods, and $m1$ is a fit parameter. The physical significance of the function $y(N)$ is that for $N \gg N_g$ it becomes a pure exponential, as expected from single-pass FEL theory, and for $N \ll N_g$ it becomes linear, also as expected. Thus, Equation (6.1) is an approximation of the complete single-pass FEL theory discussed in Chapter 3. The complete theory is compared with measurements in Sec. 6.3.

6.1.1.1 Variation of Undulator Length

Effective undulator length was varied in two ways:

1) In measurements from 1995, ferromagnetic plates were placed between the undulator and the vacuum chamber, thus ‘shorting out’ the field of the undulator’s permanent magnets. This method had the disadvantage of requiring that the electron beam be turned off to allow access to the undulator.

2) In measurements from 1996, the electron beam was steered out of the vacuum chamber as described in Chapter 4.

6.1.1.2 Use of Michelson Interferometer

Michelson interferometry was used to measure the undulator radiation. By fitting a $\frac{\sin^2 u}{u^2}$ function about the radiated wavelength in the interferogram, background due to stray synchrotron, transition, or X-ray radiation was eliminated. These backgrounds were the result of steering the electron beam out of the vacuum chamber. They also occurred when using ferromagnetic shorting plates because nonuniform residual fields, from non-ideal shorting, missteered the electron beam.

6.1.2 Gain Data

The measured bolometer voltages as a function of undulator length, fit by the function of Eq. 6.1, are shown in Figures 6.1, 6.2, and 6.3. Figures 6.1 and 6.2 are gain measurements made at around 50 μm. Figure 6.3 shows measurements at different undulator strengths, and therefore different wavelengths, and establishes a trend toward less gain at longer wavelengths.

Figures 6.1 and 6.2 show measurements made in 1995 as well as in 1996. The chronology deserves comment. The first measurement of gain was made in 1995, and reported in [45]. This was followed by a major change in the rf system which greatly increased the rf power in the gun. This produced macropulse currents of over 1 A at the gun and up to 0.5 A after the linac. It was discovered that

1) Measurable 50 μm radiation was unobtainable at the highest gun powers.

2) The measurement of gain was correlated with maximizing the radiated energy per number of electrons at the undulator.

By reproducing the earlier rf power levels and by maximizing the radiated energy per number of electrons, the 50 μm radiation and gain were reproduced.

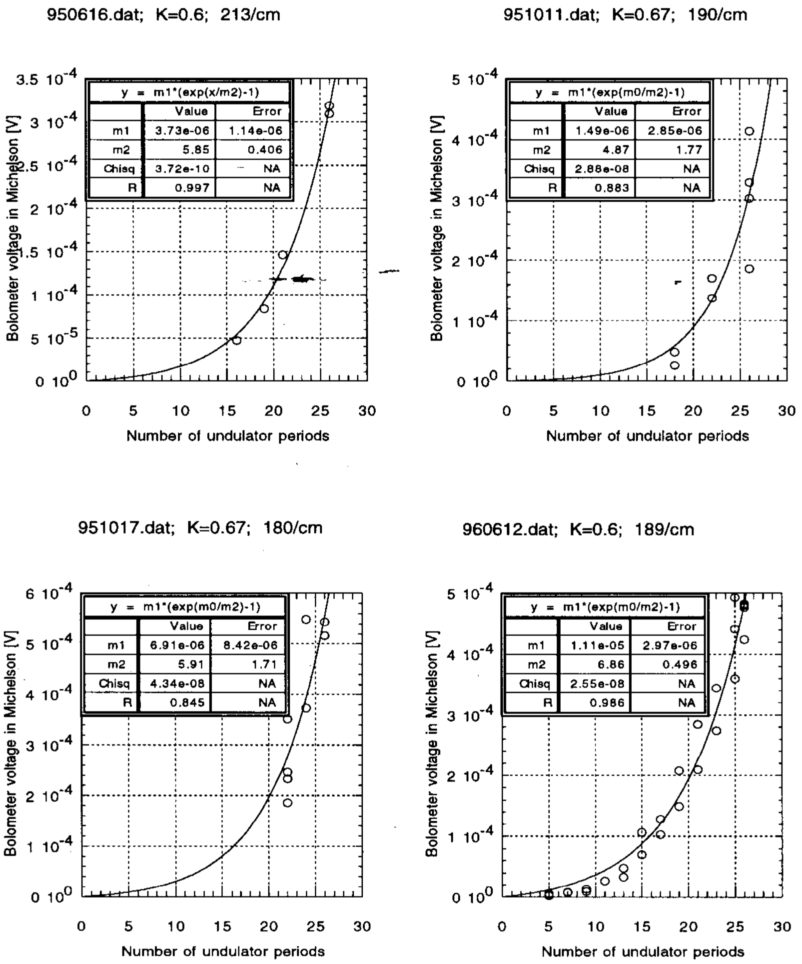

950616.dat; K=0.6; 213/cm

y = m1*(exp(x/m2)-1)		
	Value	Error
m1	3.73e-06	1.14e-06
m2	5.85	0.406
Chisq	3.72e-10	NA
R	0.997	NA

951011.dat; K=0.67; 190/cm

y = m1*(exp(m0/m2)-1)		
	Value	Error
m1	1.49e-06	2.85e-06
m2	4.87	1.77
Chisq	2.88e-08	NA
R	0.883	NA

951017.dat; K=0.67; 180/cm

y = m1*(exp(m0/m2)-1)		
	Value	Error
m1	6.91e-06	8.42e-06
m2	5.91	1.71
Chisq	4.34e-08	NA
R	0.845	NA

960612.dat; K=0.6; 189/cm

y = m1*(exp(m0/m2)-1)		
	Value	Error
m1	1.11e-05	2.97e-06
m2	6.86	0.496
Chisq	2.55e-08	NA
R	0.986	NA

Figure 6.1: Gain measurements at short wavelengths (1 of 2). The dates of the measurements and wavelengths are indicated in the graph titles. The gain length in units of undulator periods is the quantity m2 in the equation tables of the graphs.

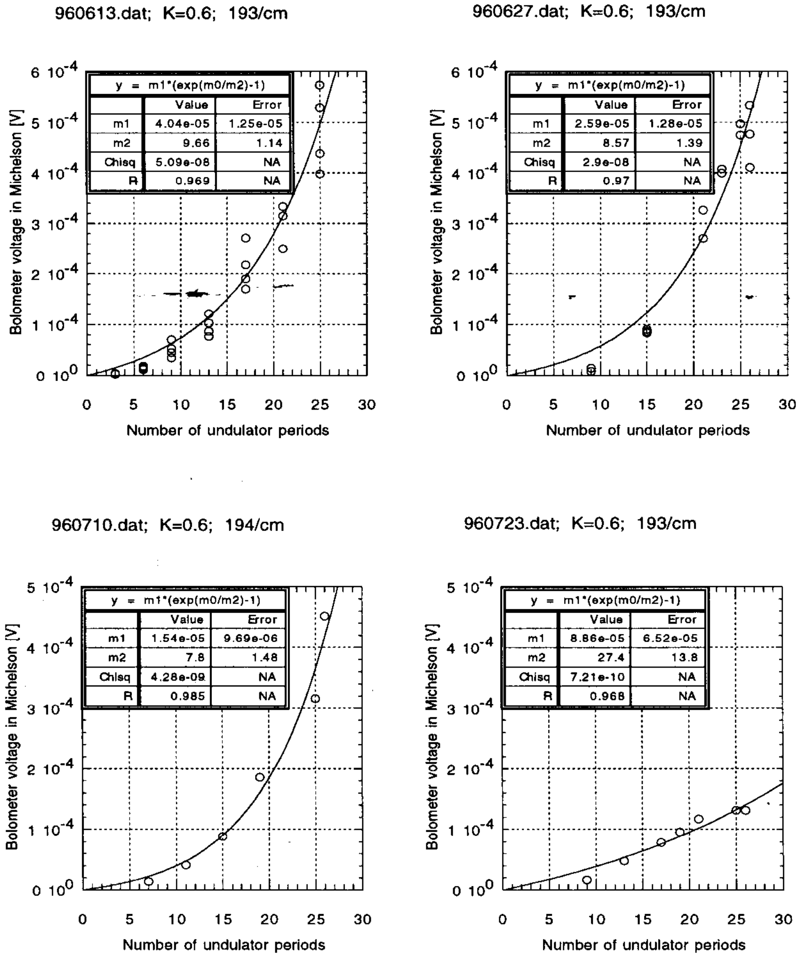

960613.dat; K=0.6; 193/cm

y = m1*(exp(m0/m2)-1)		
	Value	Error
m1	4.04e-05	1.25e-05
m2	9.66	1.14
Chisq	5.09e-08	NA
R	0.969	NA

960627.dat; K=0.6; 193/cm

y = m1*(exp(m0/m2)-1)		
	Value	Error
m1	2.59e-05	1.28e-05
m2	8.57	1.39
Chisq	2.9e-08	NA
R	0.97	NA

960710.dat; K=0.6; 194/cm

y = m1*(exp(m0/m2)-1)		
	Value	Error
m1	1.54e-05	9.69e-06
m2	7.8	1.48
Chisq	4.28e-09	NA
R	0.985	NA

960723.dat; K=0.6; 193/cm

y = m1*(exp(m0/m2)-1)		
	Value	Error
m1	8.86e-05	6.52e-05
m2	27.4	13.8
Chisq	7.21e-10	NA
R	0.968	NA

Figure 6.2: Gain measurements at short wavelengths (2 of 2). The dates of the measurements and wavelengths are indicated in the graph titles. The gain length in units of undulator periods is the quantity m2 in the equation tables of the graphs. The graph in the lower right-hand corner is the condition before optimization.

By the end of 1995, the gun cathode had deteriorated with age, and eventually the cathode had to be replaced. The new cathode became operational and stable in May 1996, when measurements resumed.

A summary of the gain measurements of Figs. 6.1 through 6.3 appears in Fig. 6.4. The trend is toward lower gain at longer wavelengths. Gain measurements at wavelengths longer than 80 μm were not done because of inadequate clearance between the vacuum chamber and the undulator magnets which caused difficulties in moving the steering magnet and in removing ferromagnetic shorting plates.

6.2 Absolute Measurements of Radiated Energy

Absolute measurements of radiated energy were usually made with the coated bolometer, whose calibration is reported in Chapter 4 and repeated here for convenience:

$$(R_V)_{170\mu\mathrm{m}} = 1.9 \pm 0.1 \ [\mathrm{V/mJ}],$$

and

$$(R_V)_{cc,50\mu\mathrm{m}} = 4.3 \pm 0.3 \ [\mathrm{V/mJ}].$$

The detector radius was 2.5 mm. The detector could be left stationary or could be scanned transversely across the FIR beam (an 'xy-scan'). Alternatively, the FIR beam could be focussed into the detector.

To calculate the expected total energy, the solid angle acceptance of the detector must be defined. For a bolometer of radius r_b at distance z from the end of an undulator of length L, the average solid angle accepted is

$$< \mathrm{d}\Omega >= \pi r_b^2 \left\langle \frac{1}{s^2} \right\rangle, \tag{6.2}$$

where

$$\left\langle \frac{1}{s^2} \right\rangle = \frac{1}{L} \int_z^{z+L} \frac{1}{s^2} \mathrm{d}s = \frac{1}{\mathrm{z}(\mathrm{z}+L)}. \tag{6.3}$$

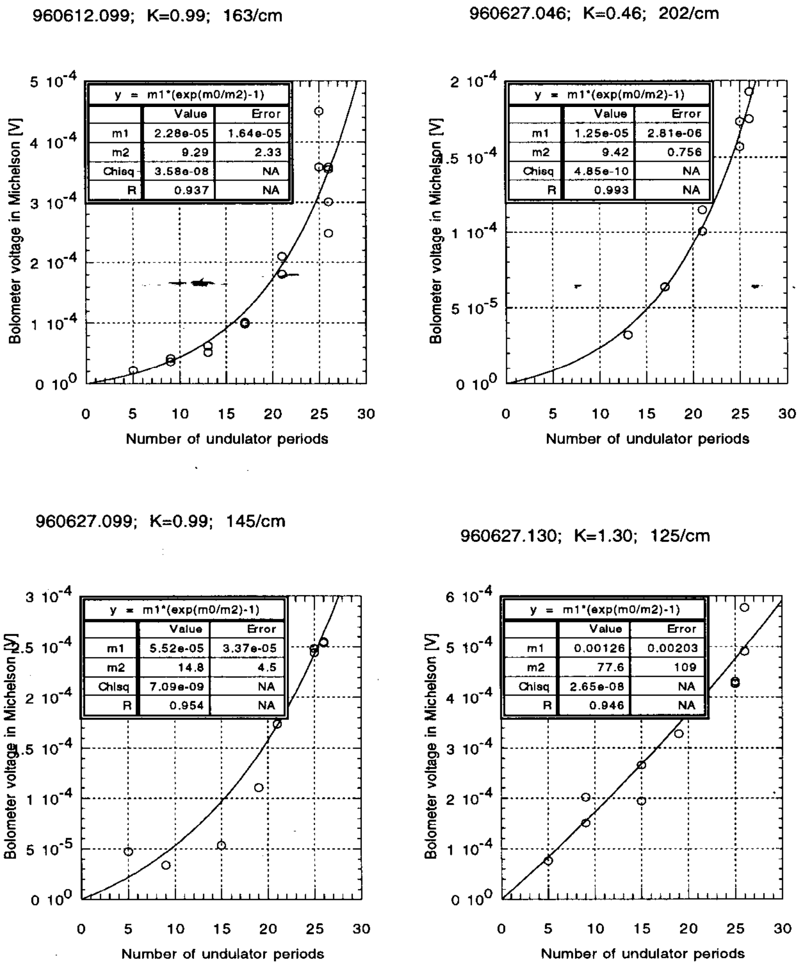

Figure 6.3: Gain measurements at different wavelengths. The dates of the measurements and wavelengths are indicated in the graph titles. The gain length in units of undulator periods is the quantity m2 in the equation tables of the graphs.

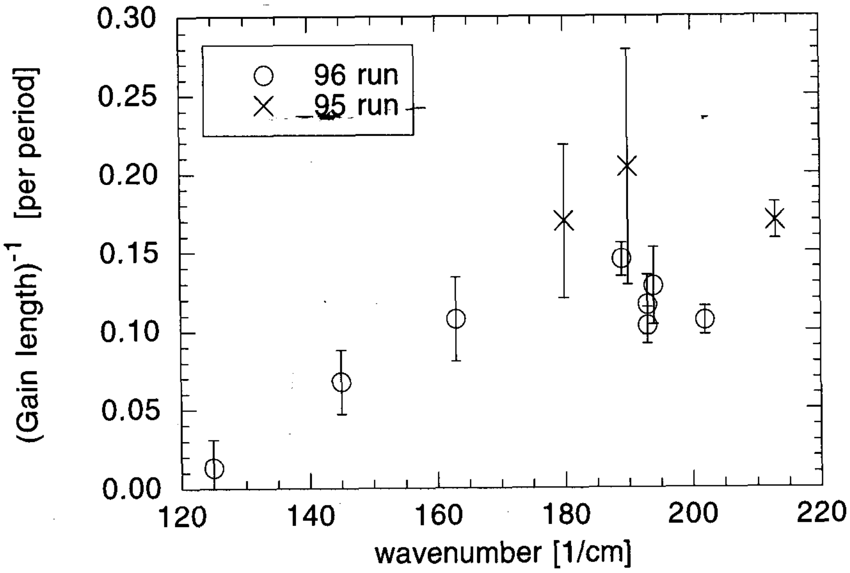

Figure 6.4: Summary of gain measurements. The fit gain coefficient, defined as the reciprocal of the gain length, is plotted as a function of the radiated wavenumber. The crosses indicate measurements from 1995, the circles are from 1996. The errors from the gain length fits give the error bars.

In this section, $z = 0$ at the undulator exit, and z increases in the direction of the radiation.

6.2.1 Total Energy Collected at 52 μm

When optimized, the measured radiated energy exceeded that expected from superradiance without gain. The total radiated energy at the window 0.3 m after the undulator exit measured by xy scans was 41 μJ. Collected by a focussing paraboloid, it measured 37 μJ. The conditions for these measurements were $K = 0.6$, $\gamma = 29$, and $\sum N_e^2 = 5.3 \times 10^{19}$. These measured energies can be compared to the expected superradiant radiation (with no gain) by multiplying the appropriate entries of Table 2.1 by $\sum N_e^2 = 5.3 \times 10^{19}$. The window has an acceptance of

$$< d\Omega >= \pi(0.016)^2 \frac{1}{(0.3)(2.3)} = \pi\theta_a^2,$$

so the acceptance angle $\theta_a = 19.3$ mrad is $0.6/\gamma$, and thus 16 μJ is expected, in the absence of gain. The measured 37–41 μJ within this 19.3 mrad acceptance is thus 2–3 times greater than expected. The measured energy into a smaller acceptance of $\theta_a = 2$ mrad is about 10 times greater than expected, as shown in the following subsection.

6.2.2 Energy in the Forward Direction

To eliminate possible geometric errors and to take advantage of the simple formula Eq. (2.12), in this subsection the radiation measurements discussed are confined to solid angles of the order of 10^{-5} sr, which corresponds to an opening angle of about 2 mrad. This allows straightforward calculation of the expected superradiance via Eq. (3.21), with the form factor of Eq. 4.7, and allows comparison with the single-pass FEL theory of Chapter 3.

K	expect wvnum 1/cm	meas wvnum 1/cm	half width 1/cm	one electron J/sr	multiplied by formfactor J/sr	expect μJ	meas μJ	ratio of meas to expect
0.46	202.3	202	29	1.073e-19	4.644e-22	0.29	2.6	9
0.60	189.6	192	22	1.457e-19	7.177e-22	0.44	5.6	13
0.99	150.2	146	26	1.774e-19	1.393e-21	0.86	9.1	11
1.30	121.3	129	27	1.48e-19	1.781e-21	1.09	9.8	9

Table 6.1: Forward energy measurements taken 4.3 m from the undulator exit by xy scans of a 1 cm radius window. The parameters for the expected energy calculation are $\gamma = 29.35$, $\sum N_e^2 = 5.3 \times 10^{19}$, and the solid angle acceptance of the window is $d\Omega_{acc} = \pi(0.01)^2/(4.3 \times 6.3) = 1.16 \times 10^{-5}$ sr. The expected undulator radiation per solid angle per electron from Eq. 2.12 is multiplied by the form factor from Eq. 4.7 to give the column labelled 'multiplied by formfactor', which in turn is multiplied by $\sum N_e^2$ and by $d\Omega_{acc}$ to get the expected energy. The measured energy is the measured bolometer voltage divided by the 4.3 V/mJ bolometer responsivity. Data taken 960627.

Spatial scans at the 1 cm radius window 4.3 m from the undulator exit were made at a set of several different wavelengths. The results are presented in Table 6.1 and show consistently that the detected energy is an order of magnitude larger than can be explained by coherently-enhanced undulator radiation.

Similar forward energy measurements made at a set of several different wavelengths in an earlier stage of the project are presented in Table 6.2 and plotted in Fig. 6.5 and show a detected energy consistently over twenty times larger than can be explained by coherently-enhanced undulator radiation alone. The decrease in radiated energy reported in Table 6.1 with respect to Table 6.2 is related to the replacement of the cathode of the rf gun. Differences in the cathode appear to have degraded the electron beam quality.

K	wvnum 1/cm	BoloResp V/J	meas J	expect J	meas/expect
6.020e-01	1.771e+02	4.074e+03	9.205e-06	3.416e-07	27
8.900e-01	1.498e+02	3.568e+03	1.359e-05	6.031e-07	24
1.050e+00	1.348e+02	3.289e+03	1.550e-05	7.391e-07	22
1.240e+00	1.182e+02	2.982e+03	1.794e-05	8.841e-07	22
1.470e+00	1.005e+02	2.653e+03	2.790e-05	1.032e-06	31
1.740e+00	8.320e+01	2.331e+03	3.668e-05	1.168e-06	37
2.050e+00	6.744e+01	2.038e+03	4.661e-05	1.281e-06	45
2.470e+00	5.163e+01	1.745e+03	4.385e-05	1.378e-06	40
2.710e+00	4.476e+01	1.617e+03	4.298e-05	1.415e-06	39
3.030e+00	3.741e+01	1.480e+03	3.208e-05	1.450e-06	29
3.230e+00	3.364e+01	1.411e+03	2.659e-05	1.465e-06	24

Table 6.2: Forward energy measurements taken 0.7 m from the undulator exit by 2.5 mm radius bolometer. The parameters for the expected energy calculation are $\gamma = 28.4$, $\sum N_e^2 = 4.5 \times 10^{19}$, and the solid angle acceptance of the bolometer is $d\Omega_{acc} = \pi(0.0025)^2/(0.7 \times 2.7) = 1.04 \times 10^{-5}$ sr. The expected undulator radiation per solid angle per electron from Eq. 2.12 including the fundamental and third and fifth harmonics for bunches coherently-enhanced by the form factor of Eq. 4.7 is multiplied by $\sum N_e^2$ and by $d\Omega_{acc}$ to get the expected energy. The coated bolometer responsivity in the third column is a linear fit of the responsivity measured at 170 μm and 50 μm. Data taken 950419.

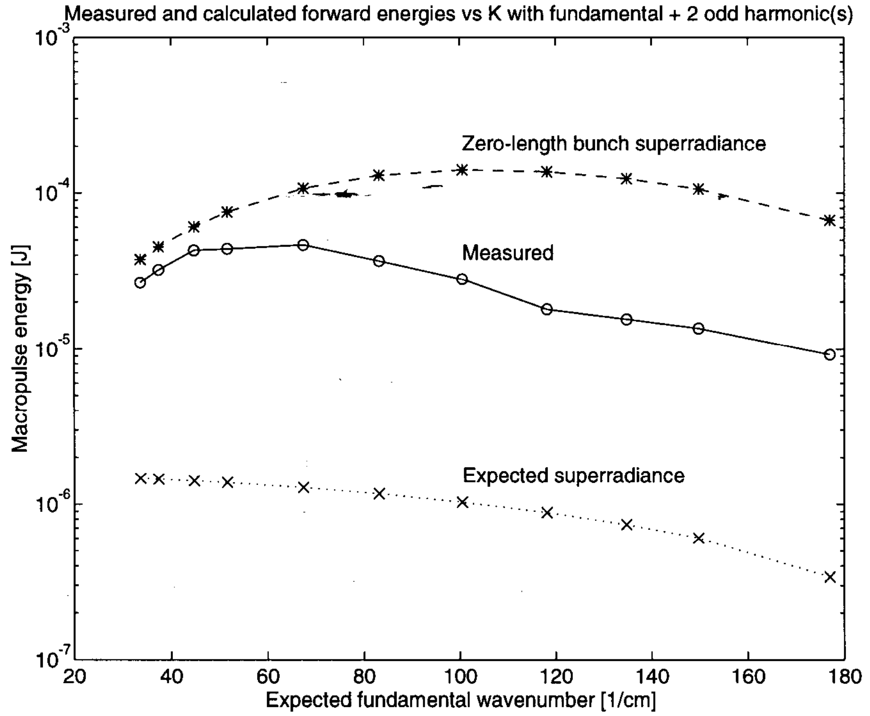

Figure 6.5: Plot of the forward energy vs K measurements listed in Table 6.2; see Table 6.2 for a description of the calculation. The circles are the measurement, the 'x'-es are expected superradiance, and the asterisks are the calculated radiation from zero-length bunches.

6.3 Absolute Gain Measurement

The Michelson interferometer was used to measure the radiated energy since it provided noise immunity. Undulator radiation was distinguished by fitting a $\frac{\sin^2 u}{u^2}$ function to the measured spectrum, as shown for example in Fig. 5.4. The measured bolometer voltage was the integrated voltage of the $\frac{\sin^2 u}{u^2}$ fit. The measured energy was the bolometer voltage divided by the responsivity of the uncoated detector (2.5 V/mJ at 50 μm).

To compare the measured energy with the energy per solid angle predicted by theory, the measured energy from the interferogram was divided by the following correction factors:

1) beam splitter efficiency at the fundamental wavelength from Fig. 4.12,

2) average atmospheric absorption in the undulator radiation band from Fig. 7.6,

3) 75 % HDPE window transmission, and

4) solid angle with respect to beam exit from undulator from Eq. (6.3).

With these corrections the measurements were compared with the single-pass FEL theory discussed in Chapter 3. The parameters varied in the fits were

1) ρ, the variation of which corresponds physically to varying the particle density by changing the bunch radius, and

2) the relative energy chirp dE (assumed to occur across a 240 μm distance).

These parameters were varied to minimize the squared error of the theoretical prediction with respect to the corrected Michelson data. All microbunches were assumed to contribute equally at the rms current value, even though there is reason to believe many of the microbunches did not contribute, as seen in Fig. 7.4.

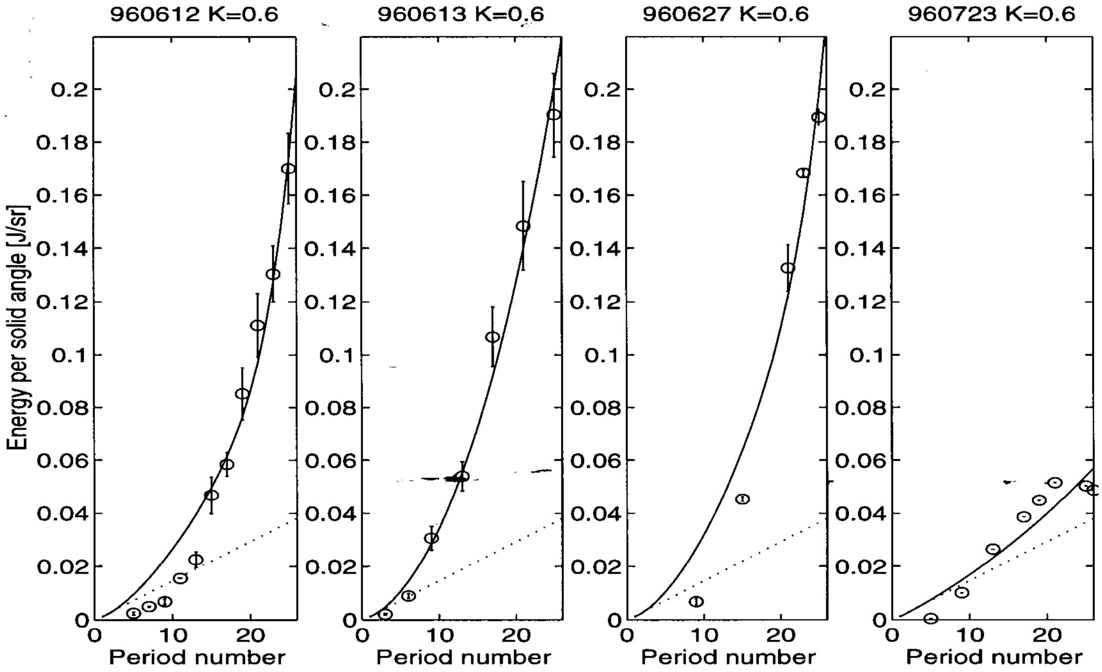

Figure 6.6: Energy per solid angle vs undulator length at $K = 0.6$. The circles are the measurements, the solid line is a theoretical SASE fit, and the dashed lines are calculated superradiant undulator radiation as discussed in the text. The first three plots are the result of optimizing the radiated energy. The fourth graph is the result of setting up the electron beam without optimizing the radiated energy and approaches the expected linear behavior in the absence of gain.

A summary of the results of this comparison for several data sets at different wavelengths is shown in Table 6.3. At 52 μm the fit ρ parameter corresponds to the ρ parameter that would be expected from a 180 μm-long bunch of radius 0.8 mm, and at 67 μm the fit corresponds to a 180 μm-long bunch of radius 1.2 mm. These radii are close to what is expected from the measurements of Chapter 4. For a Gaussian beam with a $1/e^2$ radius W, a uniform radial distribution with the same peak charge density and same total charge can be defined with an effective radius $W_{eff} = W/\sqrt{2}$, so the the 1 mm $1/e^2$ radius beam of Chapter 4 corresponds to an effective radius of 0.7 mm.

date	K	λ_r [μm]	dE	ρ	N_g
960612	0.6	53	0.0134 ± 0.001	$(9.84 \pm 0.238) \times 10^{-3}$	4.67 ± 0.11
960613	0.6	53	0.0175 ± 0.006	$(6.16 \pm 5.67) \times 10^{-3}$	7.46 ± 6.87
960627	0.6	53	0.0172 ± 0.001	$(9.08 \pm 0.479) \times 10^{-3}$	5.06 ± 0.27
960612	0.99	67	0.0000 ± 0.004	$(10.9 \pm 0.214) \times 10^{-3}$	4.22 ± 0.08
960627	0.99	67	0.0000 ± 0.030	$(9.86 \pm 0.550) \times 10^{-3}$	4.66 ± 0.26

Table 6.3: Gain length absolute measurements. This table summarizes the theoretical fits shown in Figures 6.6 and 6.7 in terms of the energy chirp dE and the ρ parameter, which were the only variables in the fits. The ρ parameter is related to the gain length N_g listed in the table by $N_g = 1/(4\pi\sqrt{3}\rho)$.

The measured energy and theoretical fits for the 52 μm radiation are shown in Fig. 6.6. The first three plots show data resulting from experimentally optimizing the radiated energy; the fourth graph is the result of setting up the electron beam without optimizing the radiated energy and approaches the expected linear behavior in the absence of gain. This illustrates that the observed gain is a result of optimizing the total radiated energy, and experimentally verifies the linear energy-vs-length dependence expected from short-bunch superradiance.

Regardless of theory, this experiment has observed self amplification which is the cause of a factor of four increase in detected radiation over superradiance as shown in Fig. 6.6. This factor of four is less than the factor of 13 reported in Table 6.1. It is possible that in addition to the factor of four from the gain there is a factor of three enhancement due to guiding of the radiation. This factor of three does not appear in Fig. 6.6 because the Michelson is only 1/3 as efficient as expected at 50 μm, as discussed in Section 7.3.3.

6.4 Conclusions

From the gain and forward energy measurements described in this chapter, the following conclusions can be drawn:

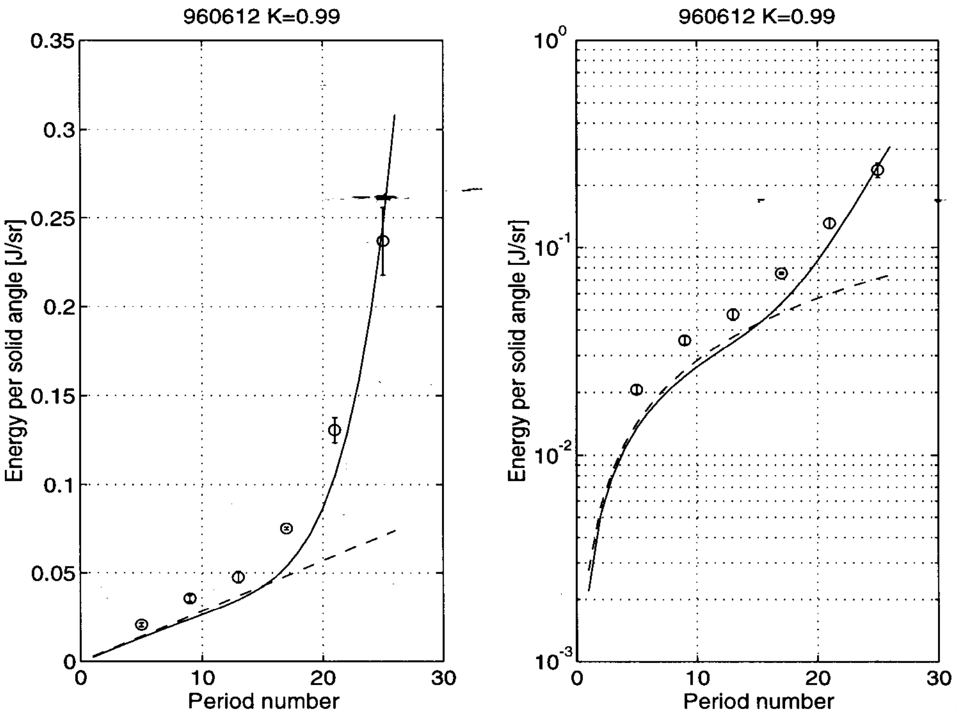

Figure 6.7: Energy per solid angle vs. undulator length at $K = 0.99$. The circles are the measurements, the solid line is a theoretical SASE fit, and the dashed lines are calculated superradiant undulator radiation as discussed in the text. The first graph is in linear scale, the second is semilog.

1) The forward energy is more than expected from superradiant emission at all wavelengths—the radiation is an extremely bright FIR source.

2) At 50 μm through 70 μm wavelengths, the higher-than-expected forward energy is primarily the result of the gain predicted from single-pass FEL theory.

3) At 80 μm, and longer wavelengths if the trend shown in Fig. 6.4 continues, the higher-than-expected forward energy is *not* the result of the gain. At these wavelengths the higher-than-expected forward energy may be the result of waveguiding by the 1 cm radius vacuum chamber.

Chapter 7

Discussion of Measurements

In support of the conclusions of the previous chapter, complicating effects involving the details of the electron beam and instrumentation are discussed in the present chapter. Interesting features of the spatial distribution and divergence of the FIR radiation are discussed as well. Summarizing the points made in this chapter:

1) At $K = 0.6$ the bunch shortening/lengthening from energy spread is expected to change the coherent enhancement at the downstream end of the undulator by ±20%.

2) Energy chirp may increase the total energy emitted from the undulator by a factor of three due to its effect as a source term in single-pass FEL theory.

3) In order to match the measured energy spread, one must assume that only 40% of square of the macropulse charge is contributing to the measured undulator radiation.

4) At $K = 0.6$ the beam may be twice as wide horizontally when exiting the undulator (as compared to entering the undulator) causing a 26% increase in gain length at the exit.

5) At 50 μm, the Michelson measured efficiency is only one third of that expected from theory.

6) The measured radiation divergence is consistent with a Gaussian beam of 3 mm effective $1/e^2$ radius, which is larger than the measured 1 mm effective $1/e^2$ electron beam radius.

7) The radiation divergence increases with wavelength linearly with λ.

8) The spatial distribution of radiation is approximately radially symmetric. It does not exhibit a measurably larger horizontal divergence than vertical divergence, even when there is $\sim$ 100 mrad bending in the horizontal plane.

9) The spatial distribution of radiation measured at the downstream end of the undulator chamber does not change as the beam is steered out of the undulator.

Items 1, 2, 3, and 4 state that the effects of energy spread and beam size upon the SASE process are either relatively small, or actually help the process (item 2). Item 5 states that the Micheson underestimates the full amount of radiation by a factor of 1/3. Items 6, 7, 8, and 9 are consistent with guided radiation emerging as a diffraction pattern from the downstream end of the undulator chamber.

Although there is strong evidence of waveguiding, the analysis of these measurements in terms of waveguiding and/or optical guiding is not pursued in this thesis. The point of this thesis is to experimentally characterize the FIR source and the self-amplification. If there is sufficient interest in these results, it is hoped that the theory will be pursued by others in the FEL community.

7.1 Effect of the Electron Beam

The electron beam has properties not considered in the theory of Chapters 2 and 3. The electron beam is not mono-energetic, nor is it mono-directional: it has an energy spread and emittance.

7.1.1 Effect of Energy Spread

The electron beam energy spread within a micropulse is important in the determining the bunch/radiation dynamics, while the energy spread over the macropulse is less important and only broadens the observable spectrum (the detector system integrates the radiated energy over the entire macropulse).

To understand the effect of energy spread it is worthwhile to consider the sinusoidal trajectory described in Eq. (2.2). The path length through the undulator for an electron of energy γ and velocity $\beta = \sqrt{1 - 1/\gamma^2}$ is

$$s = \int_0^L \sqrt{1 + \left(\frac{\mathrm{d}x}{\mathrm{d}z}\right)^2} \mathrm{d}z = \int_0^L \sqrt{1 + \frac{K^2}{\gamma^2} \sin^2 \frac{2\pi z}{\lambda_0}} \mathrm{d}z, \tag{7.1}$$

which becomes

$$s \approx \int_0^L \left(1 + \frac{K^2}{2\gamma^2} \sin^2 \frac{2\pi z}{\lambda_0}\right) \mathrm{d}z = L\left(1 + \frac{K^2}{4\gamma^2}\right). \tag{7.2}$$

The transit time is

$$T = \frac{s}{c\beta} \approx \frac{s}{c}\left(1 + \frac{1}{2\gamma^2}\right) \approx \frac{L}{c}\left(1 + \frac{1}{2\gamma^2}\left(1 + \frac{K^2}{2}\right)\right). \tag{7.3}$$

To the same order of approximation the difference in transit times between particles of energy γ and $\gamma - \delta\gamma$ is

$$\frac{\delta T}{L/c} = \frac{1}{\gamma^2}\left(1 + \frac{K^2}{2}\right)\frac{\delta\gamma}{\gamma}. \tag{7.4}$$

Equation (7.4) describes the bunch lengthening δT due to a fractional energy spread $\frac{\delta\gamma}{\gamma}$. Evaluating it for the SUNSHINE conditions, $\gamma = 29.35$, $L = 2.0$, $K = 0.6$, with

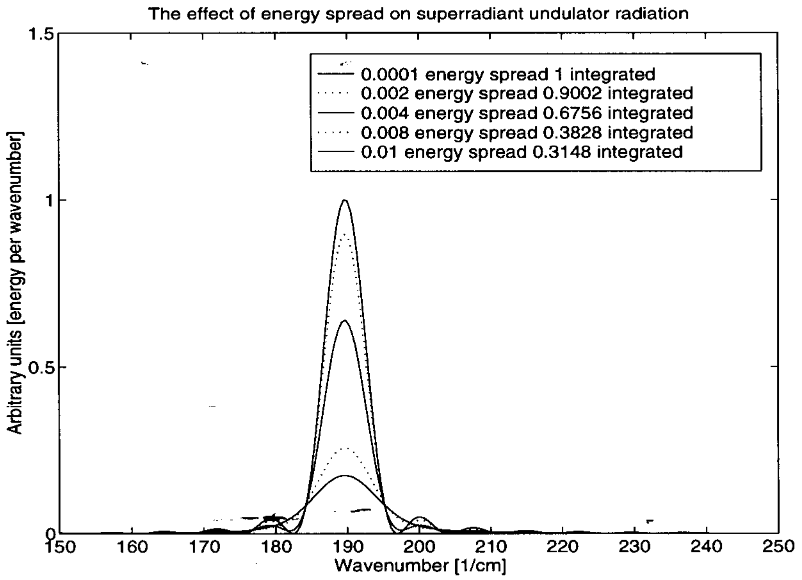

Figure 7.1: Calculated effect of micropulse energy spread on superradiant radiation. Energy spectral density per solid angle for infinitesimally short bunches entering the undulator with Gaussian rms energy spreads of 0.01, 0.2, 0.4, 0.8, and 1%

$\frac{\delta\gamma}{\gamma} = 0.01$, gives $\delta T = 77$ fs which is negligible in comparison to the ≈ 600 fs bunch length. However for large K values the bunch lengthening (or compression) due to energy spread (or slew) can be quite large. For example if $\gamma = 29.35$, $K = 3.2$, and $\frac{\delta\gamma}{\gamma} = 0.01$, then $\delta T = 474$ fs is of the order of the bunch length itself.

7.1.1.1 Effect on Superradiance

The effect of micropulse energy spread on the emitted superradiant radiation can be approximated by considering an infinitesimally short bunch with a Gaussian energy spread entering a 26-period undulator. Each electron will radiate 26 oscillations at the fundamental frequency determined by its energy. At first all the particles radiate in phase, but because they radiate at slightly different frequencies, destructive interference soon occurs—this is analagous to the way a delta function can be built out of sine waves. This causes line-broadening, but also reduces the amplitude of the

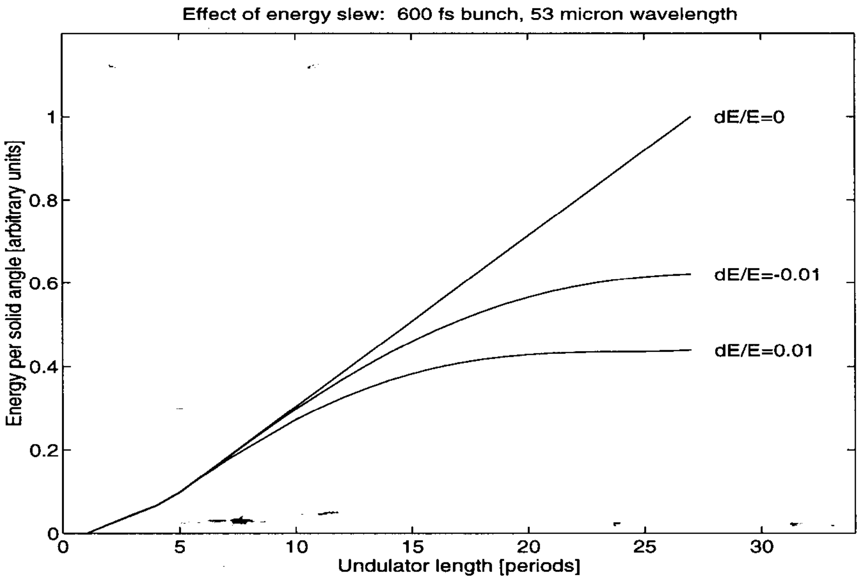

Figure 7.2: Calculated effect of energy slew on superradiant undulator radiation. The bunch is of length 180 μm and energy $\gamma_0 = 29.35$. The wiggler is at strength $K = 0.6$. The energy slew dE/E occurs over the length L of the bunch. A positive slew corresponds to greater energy particles at later times. Reductions to 62% and 44% of the mono-energetic case occur due to the 1% slew.

coherently-enhanced radiation. As shown in Fig. 7.1, a 1% rms energy spread reduces the coherent-enhancement to 30% of the ideal value. This can be understood as a consequence of the reduced form factor of the initially zero-length bunch due to the bunch-lengthening described by Eq. (7.4).

Micropulse energy chirp can have a helpful or detrimental effect on superradiant undulator radiation depending on whether it shortens or lengthens the bunch. For a rectangular bunch of 600 fs (= 180 μm) length radiating at 52 μm, the form factor is near a local maximum, so energy chirp of either sign is detrimental—as shown in Fig. 7.2 a ±1% energy chirp over the length of the bunch reduces the superradiant emission to about 50% of the mono-energetic case.

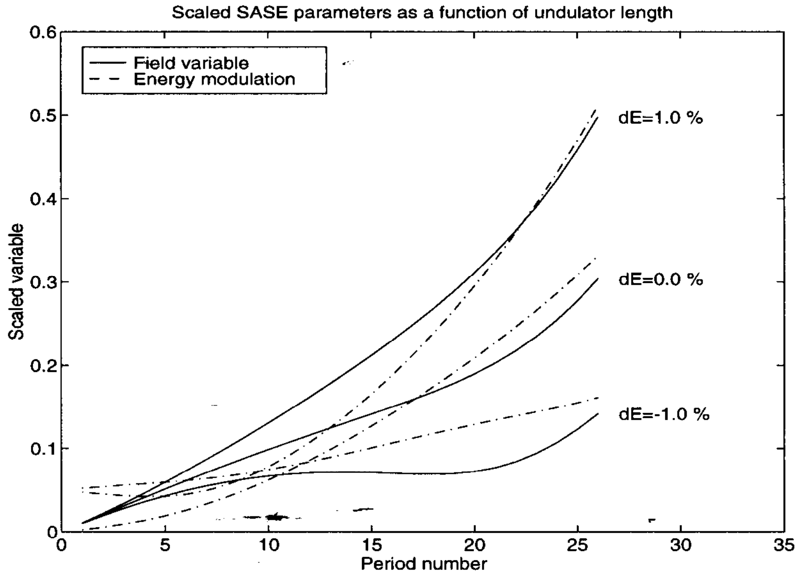

Figure 7.3: Calculated effect of energy slew on magnitude of SASE parameters X (field) and Z (energy modulation). The bunch is of length 180 μm and radius 1 mm and contains 2×10^8 electrons of energy $\gamma_0 = 29.35$. The wiggler is at strength $K = 0.6$ and has 26 periods each of length $\lambda_0 = 0.077$ m. The energy slew of magnitude dE occurs over the length L of the bunch.

The measured form factor of the beam is proportional to the square of the wavelength over the bunch length and has a smoother roll off than that of a pure rectangular pulse. Therefore changes of less than 50% in the radiated energy are expected. An energy chirp of 1% producing a 77 fs change in a bunch with an effective length of 800 fs and a form factor given by Eq. 4.7 will produce a $2 \times 77/800 = 0.2 = 20\%$ increase or decrease in the form factor, and therefore in the radiated energy.

7.1.1.2 Effect on SASE

There are two effects of micropulse energy spread on the SASE process. First, random energy spread reduces the efficiency of the SASE process, and can inhibit it completely when the rms energy spread is of the order of the Pierce parameter ρ [23, page 63]. Secondly, non-random energy spread, *ie* energy modulation, can actually help the

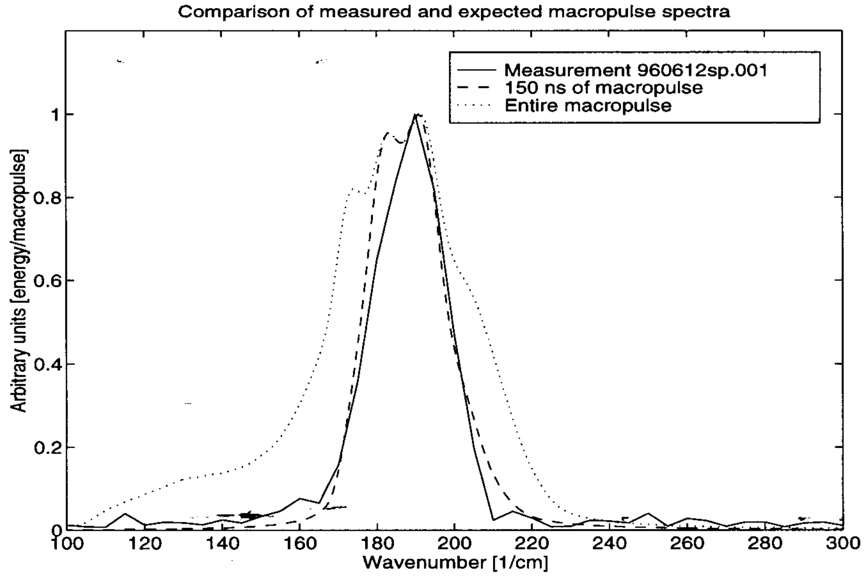

Figure 7.4: Effect of macropulse energy spread on the observable spectrum

SASE process [46], by way of the Z_0 source term in Eq. (3.8). As shown in Fig. 7.3, a one percent energy chirp over the length of the microbunch can result in a factor of 5/3 increase in the field variable, and thus a factor of 3 in the energy. This is in contrast to the superradiant calculation discussed in the previous subsection, where the energy chirp reduced the superradiant energy under the same conditions.

7.1.2 Expected Effect of Measured Energy Spread

The energy variation over the macropulse is large, as shown in Fig. 4.6. In fact the measured radiation spectrum, as shown in Fig. 5.4, is narrower than would be expected if the entire electron beam macropulse were contributing. A 150 ns time-slice of the macropulse (leading up to and including the peak current) produces an expected spectrum matching the measured spectrum shown in Fig. 7.4. This time slice contains 39% of the total $\sum N_e^2$ over the macropulse. This shows that perhaps only half of the macropulse is contributing to the 52 μm radiation.

In computing the expected spectrum, each micropulse within the macropulse is weighted by the square of its charge, because each micropulse is expected to radiate proportional to the square of its charge. The average, again weighted by the square of the current, measured micropulse energy spread is 0.9% rms over the 150 ns time-slice. This is enough spread to cause some effect in the coherent enhancement. From the previous section, a 1% energy chirp causes a 20% increase or decrease in the radiated energy at the end of the undulator, but causes a factor of three increase in SASE.

If the the measured energy spread were purely random, theory predicts self-amplification will not occur. Since self-amplification is seen, theory predicts the measured energy spread is mostly correlated: 'slewed' or 'chirped' rather than random, and therefore helps the SASE process, as shown in Fig. 7.3. It is not possible to tell from direct measurements whether the micropulse energy spread is correlated or uncorrelated.

7.1.3 Electron Beam Size

As discussed in Sec. 4.2.4, TRANSPORT gives an average $1/e^2$ beam radius of 1 mm in the undulator.

7.1.3.1 Effect on Superradiance

The beam size does not cause line-broadening of the frequency spectrum due to electrons at different positions experiencing different undulator strengths, because from Eq. (4.2), the field at the edge of the beam,

$$B_y \propto \cosh(k_0 y_{max}) = \cosh(2\pi \times 0.001/0.077) = 1.003,$$

is clearly negligibly close to the field at the center ($y = 0$). A *large* offset of the electron beam within the undulator can cause some effect. For example a 5 mm offset increases the B_y field by 8%, which for $K = 0.6$ translates to a 3% shift in radiated wavelength.

The three-dimensional form factor discussed in Chapter 2 includes the effect of the beam size on superradiance, which is basically that smaller transverse size means more off-axis coherent radiation. This is analagous to Fraunhofer diffraction from the electron bunch. (As mentioned in Chapter 2, that mathematics of Fraunhofer diffraction is identical to the mathematics of the form factor.)

7.1.3.2 Effect on SASE

The primary effect of beam size on SASE is through the charge density: the higher the charge density, the greater the self amplification. This can be seen from the dependence $\rho \propto n_e^{1/3}$ where ρ and the number density n_e are defined in Table 3.1. The gain length $N_g \propto 1/\rho$ then gives $N_g \propto n_e^{-1/3}$, so larger n_e means shorter gain length. The beam sizes, measured on phosphor screens (15) and (23) in Fig. 4.10, were 2.9 mm horizontal and 2.5 mm vertical full width before the undulator (at (15) in Fig. 4.10), and 4.5 mm horizontal and 1.9 mm vertical full width after the undulator (at (23) in Fig. 4.10). From these measurements, and from the TRANSPORT model shown in Figs. 4.8 and 4.9, the beam is approximately constant in vertical size but is twice as wide horizontally exiting the undulator as compared to entering. Thus the gain length is expected to be $2^{1/3} - 1 = 26\%$ longer at the exit than at the entrance of the undulator.

Another effect is that in SASE theory the diffraction of the radiation from the finite source size, in this case the size of the electron beam, is expected to cause a reduction in gain. The radiation divergence at 52 μm from a uniform 1 mm radius source is expected from the first zero of $J_1(u)/u$ to be

$$\theta_{div} = 0.61\lambda/r_{max} = 32 \text{ mrad},$$

and from a $W_0 = 1$ mm $1/e^2$-radius waist of a Gaussian beam

$$\theta_{div} = \frac{W_0}{z_R} = \frac{\lambda}{\pi W_0} = 17 \text{ mrad}.$$

However, the measurements of Table 5.1 indicate the angular divergence of the radiation is 5 mrad at 52 μm, which implies a 3 mm radius source size. This is significantly larger than the 1 mm radius electron beam, and significantly reduces diffraction effects.

To explain this discrepancy in radiation source size with respect to electron beam size, one can argue that there may be waveguiding by the undulator chamber or optical guiding by the electron beam.

7.1.4 Electron Beam Divergence

The TRANSPORT-modeled average angular spreads of the electron beam within the undulator are $\sigma_{x'} = \sigma_{y'} = 0.5$ mrad. This angular divergence does not broaden the radiation pattern significantly, and its effect on superradiant emission and SASE is therefore ignored.

7.2 Radiation Absorption

FIR radiation is partially absorbed by polyethylene windows and by water vapor in the atmosphere. The polyethylene windows used to separate the vacuum required for the electron beam from the atmosphere have (intensity) transmissions of from 75% at 50 μm to 90% at 200 μm, according to the manufacturer.

A practical model known as HITRAN [47] is used to compute the effect of atmospheric humidity via the commercial code HITRAN-PC [48]. The transmission at the wavenumbers of interest is plotted in Fig. 7.5 which shows that the absorption due to

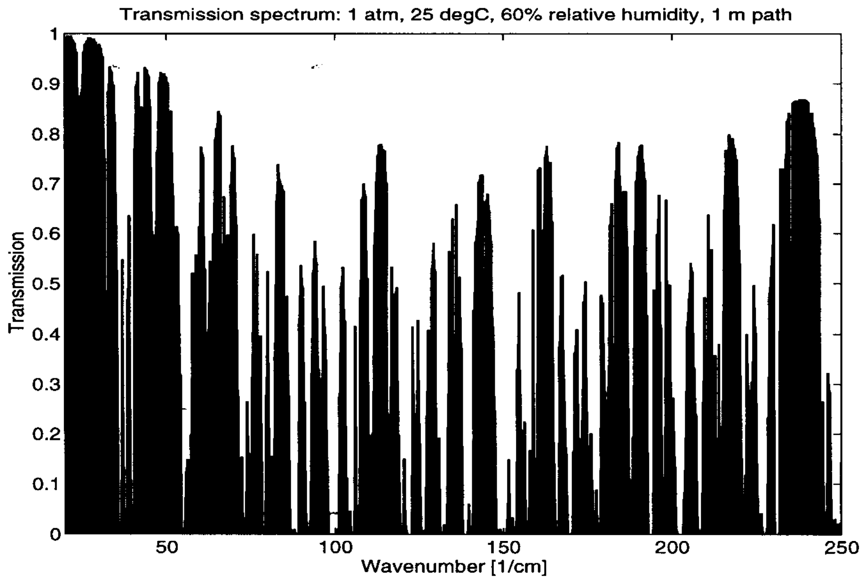

Figure 7.5: The effect of humidity as calculated from HITRAN. The energy transmission for wavenumbers 20/cm through 250/cm is shown. The parameters of the HITRAN run are 1 m path length, 25 deg C, 1 atm pressure, and 0.012 atm H_2O vapor pressure corresponding to 60% relative humidity.

water vapor can be quite severe. Energy measurements must be corrected to account for this.

For a one-meter path length and 60% relative humidity the transmission averages 30% over the 100-200/cm wavenumber range. In order to see the overall transmission, Figure 7.6 shows the mathematically smoothed transmission spectrum for several different path lengths. The smoothed spectrum is used to correct the energy measured by the Michelson interferometer.

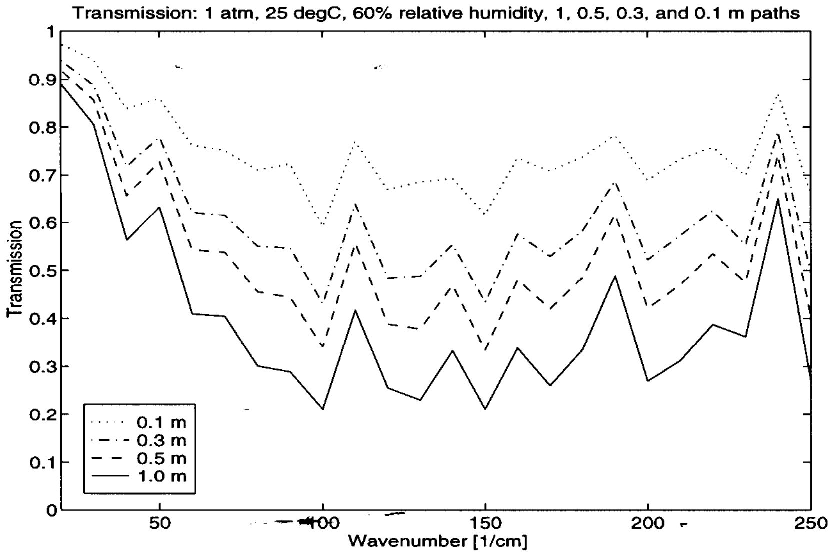

Figure 7.6: Atmospheric absorption through 0.1, 0.3, 0.5, and 1 m path lengths. The other parameters are identical to Fig. 7.5. The transmission spectrum has been mathematically smoothed to illustrate the overall effect of atmospheric absorption.

7.3 Radiation Spatial Distribution and Divergence

7.3.1 Spatial Distribution at 52 μm

The measured spatial distribution at 52 μm in Fig. 7.7 illustrates a typical distribution and its Gaussian approximation. The measured distribution is approximately Gaussian, but is somewhat sharper than the Gaussian, in Fig. 7.7 having 24% greater amplitude than the fit Gaussian. As shown in Fig. 5.9 and Table 5.1 and discussed below the size-vs-distance behavior of the distribution is consistent with a Gaussian beam which fills the undulator chamber at exit.

7.3.2 Angular Divergence

The measurements of the 227, 91, and 52 μm radiation as shown in Fig. 5.9 and Table 5.1 demonstrate that the angular divergence increases linearly with the radiation

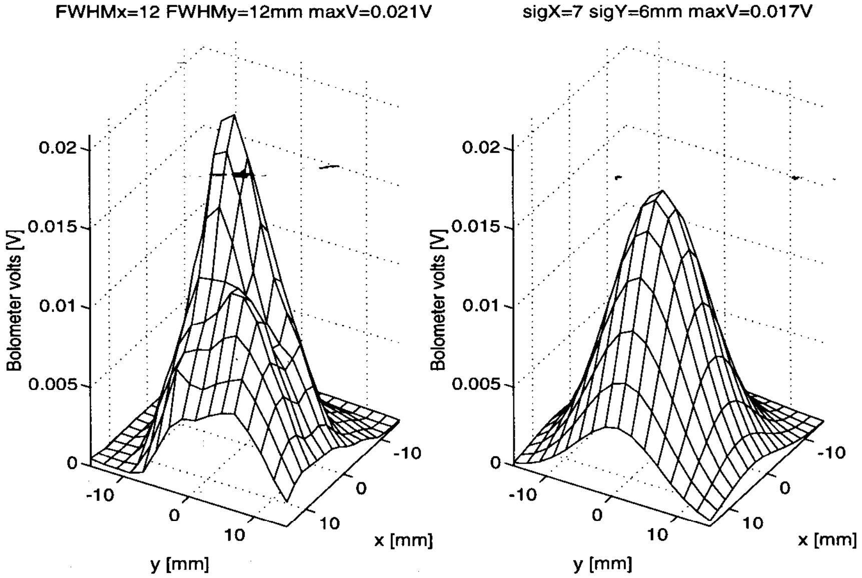

Figure 7.7: Leftmost plot is measured (960612) spatial distribution at 52 μm taken 0.32 m from undulator exit. A 600 μV uniform background has been subtracted from the measured data. The maximum bolometer voltage is 21 mV and the integrated voltage over the entire measurement, when corrected for the overcounting due to 2 mm steps of a 5 mm aperture, is 176 mV which corresponds to 41 μJ. The FWHM measured is 12 mm. The rightmost plot shows a least-squares fit of a Gaussian to the measurement.

wavelength, as would be expected from a diffraction-limited source. The angular divergence does not increase as $\sqrt{\lambda}$, as would be expected for the quasi-monochromatic 'central cone' of Eq. (2.19).

The measurements shown in Fig. 5.9 are for the vertical dimension, which is perpendicular to the wiggle plane, so one would not expect broadening from increasing K. In the horizontal plane the measurements are basically the same: the measured spatial distributions are approximately radially symmetric, as shown in Figs. 5.7, 5.10, and Fig. 7.7, for example. Overall the measurements suggest that a Gaussian beam filling the undulator chamber is a reasonable approximation of the spatial characteristics of the radiation.

In Fig. 5.9 the beam size measurement nearest the undulator for the 52 μm radiation (approximately the same as that shown in Fig. 7.7) is not included. If included, the measurements showed the shape of the distribution could be modelled as a Gaussian beam expanding with 2 mrad divergence from a waist some 5.7 m usptream of the undulator. However there was an obvious problem in that the size of the modelled beam would be larger than the inner radius of the undulator chamber.

One possible cause of this effect is the structure of the mirror used to reflect the radiation. The mirror consists of a circular 'drumhead' of Al foil, 43 mm in diameter. The drumhead tension is provided by a 4-mm-thick ring surrounding the drumhead foil. The ring contains sharp edges which can scatter incident radiation. Near to the mirror a beam reflected from the ring structure may resemble the incident beam, with some broadening. Further from the mirror the scattered radiation diverges and forms a low level background about the remaining core of the beam. The net result is that the core of the beam looks larger near the mirror and appears to get smaller further from the mirror. Thus the core of the beam appears less divergent, and may even appear slightly convergent depending on the degree of scattering.

To get around this problem the 52 μm radiation data taken nearest the mirror was ignored. The 91 μm and 227 μm measurements were sensible without the preceding correction, possibly because these longer wavelengths do not 'see' the sharp edges. The near data was included in the fits for these wavelengths as shown in Fig. 5.9.

In order to independently verify the divergence measured for the 52 μm radiation, energy measurements at different locations were done. Spatial distribution measurements of a total energy of 41 μJ at the window 0.3 m from the undulator compare to 5.6 μJ at a 1 cm radius window 4.3 m from the undulator, and total energies collected by paraboloids at the same two locations are 37 μJ and 3.9 μJ respectively.

Using the Gaussian beam model

$$I(r) = I_0 e^{-\frac{2r^2}{W^2}}, \tag{7.5}$$

where I_0 is the peak radiation intensity in [W/m^2], the power within a radial distance r_{max} is

$$P = P_{tot}\left[1 - e^{-\frac{2r_{max}^2}{W^2}}\right], \tag{7.6}$$

where P_{tot} is the total power in the radiation beam. With a −1.91 m source location and 0.58 m Rayleigh length, Eq. (5.1) predicts a 12 mm beam radius at 0.3 m, and a 33 mm beam radius W at 4.3 m. Within the $r = 10$ mm window radius at those locations 97% and 17%, respectively, of the total beam energy are expected. Thus at 4.3 m 17% of the energy measured at 0.3 m should be detected. This compares to the 11% measured with the paraboloids and 14% measured by xy scans.

To eliminate this discrepancy and match the 14% measured by xy scans, a 36.9 mm radiation beam radius is needed at 4.3 m. This corresponds to a source radius of 2.8 mm, and thus a 0.47 m Rayleigh length. This is not significantly different from the 3.1 ± 0.6 mm radius and 0.58 ± 0.23 m Rayleigh length of Table 5.1. Thus the energy measurement confirms, within errors, the result of the divergence measurement.

7.3.3 Experimental Measurement of Michelson Efficiency

The preceding measurements can be compared to the 165 nJ detected under the same conditions by the Michelson after the dump. This requires making corrections for the acceptance, beam-splitter efficiency, and atmospheric absorption of the Michelson. The Michelson acceptance is determined by a 1 cm HDPE window, at 2.1 m from the undulator exit, where a beam width of 2.2 cm is expected, and hence 34% of the radiation beam energy should be accepted. The beam-splitter efficiency is 7% and the atmospheric absorption is 60% so 1.4% of the total energy, that is 518 nJ of 37 μJ, is expected at the detector. This is greater than the 165 nJ detected, which may be partially due to a misalignment in the Michelson.

There is about 240 nJ in the DC component of the Michelson interferogram compared to 165 nJ in the undulator radiation (integrated energy spectral density), which may mean that some of the incident radiation is not interfering at the detector. In the ideal case the DC component of the interferogram should equal the sum of the harmonic components (see Eq. (4.18)), however if the beam spots from the two arms of the interferometer are offset at the detector, then the harmonic components are reduced while the DC component of the interferogram remains the same. More commonly, if there is an angular error then rather than a uniform spot, fringes will appear. As the scan progresses the bright fringes exchange positions with dark fringes and so do not contribute to the harmonic component of the interferogram; the detected interference is dominated by the amount of the central spot that is imaged to the detector. This may be happening to some extent in the Michelson, and would explain why the DC voltage level in the interferogram is greater than the integrated voltage in the spectrum. It would also help explain why the detected energy is smaller than expected from comparison with the paraboloids and xy scans.

Whatever the reason, these measurements show that the energy in the interferogram is only a third of what is expected, after correction for beam-splitter efficiency and atmospheric absorption. Therefore the efficiency of the Michelson is a factor of three less than expected.

7.4 Magnitude of Radiated Energy

The total energy at 52 μm (and all other wavelengths) was found to be greater than expected from coherent enhancement alone. To explain the discrepancy at 52 μm as due to collection of large-angle radiation and match the measured 41 μJ, the xy scan must collect angles out to $2.1/\gamma = 70$ mrad, which is a 9 cm radius at the scan location (with respect to the undulator midpoint). This is certainly not in any way consistent with the either 1.6 cm radius of the HDPE window or the 3 cm full travel of the scan. Of course, the angular divergence measurements discussed in the previous section directly show that such large-angle radiation is not contributing to the measurement. With the large acceptance provided by light pipes discussed in Chapter 5, see Figs. 5.7 and 5.8, it was shown that there can be substantial radiation at large angles, it was simply not collected with the setup of Fig 4.10.

7.4.1 Energy in the Forward Direction

A remarkable feature of the radiation measurements of Table 6.2 and Fig. 6.5 is that the measured energy at long wavelengths, if it is all at the fundamental frequency, is greater even than would be expected from a form-factor of one, the maximum possible. One factor reducing this discrepancy is that there is substantial coherently-enhanced radiation in the higher harmonics, especially the third harmonic—evidence of this is seen in Fig. 5.5.

Another effect that underestimates the expected radiation is that the calculation has assumed an average acceptance angle defined in Eq. (6.3), which is equivalent to assuming the radiation propagates as in free space, becoming spherical wavefronts after several Rayleigh lengths. If the radiation is being guided within the undulator chamber then Eq. (6.3) no longer applies and a better approximation is that the radiation is diverging from the undulator exit. Using the acceptance with respect to the undulator exit results in multiplying the expected and form-factor-one energies by a factor of $2.7/0.7 \approx 4$, after which the measured energy is less than the calculated form-factor-one energy, even ignoring the contribution of the third and higher harmonics.

Other evidence at long wavelengths pointing to guiding, and in particular waveguide modes, is that the measured spatial distribution is approximately symmetric, as shown in Fig. 5.7 for example. What is expected at a wiggler strength $K \approx 3$, as is the case in Fig. 5.7, is a distribution that is three times wider horizontally (*ie* in the wiggle plane) than vertically and this is not seen at all. The measured spatial distribution and the angular divergence measurements of Fig. 5.9 suggest that at long wavelengths the radiation is expanding as an approximately symmetric diffraction pattern from near the exit of the undulator.

At short wavelengths, the measurement of Fig. 5.10 showed that the spatial distribution of undulator radiation did not change as a function of undulator length. This is strong evidence of waveguiding even at short wavelengths.

7.5 Gain Measurements and Theory

The quantitative agreement with one-dimensional theory is suprising, as there are two main effects that would be expected to reduce the measured gain from that expected from the theory. One is the diffraction of the radiation away from the electron beam. The other is the forward slippage of the light away from the finite-length electron bunch, which reduces the time the light can interact with the electron beam. The diffraction effect is not too severe, since the measured Rayleigh length of 52 μm radiation is about 0.5 m, which means the spot doubles in area (and the intensity drops by 50%) every 0.5 m. This Rayleigh distance corresponds to about seven undulator periods hence seven radiation wavelengths and thus is longer than the slippage time for the light across the approximately four-wavelength-long bunch. Thus diffraction within a 'slippage time' is small, and the effect of slippage is expected to be greater than that of diffraction.

The gain degradation expected from slippage may be overcome by several factors. One is the unique properties of very-short bunches which are ignored in the slowly-varying-envelope approximation (SVEA) which is used in most, if not all, FEL theories. Theoretical studies suggest that including the terms dropped by the SVEA will result in an increase in the predicted gain [50].

Another factor which may overcome the losses due to slippage is the energy-time correlation in the SUNSHINE beam which acts as a source term in Eq. (3.8) [46]. As shown in Fig. 7.3 a 1% linear energy chirp over the bunch can result in almost tripling the radiated energy predicted by the theory. Possibly other coherent structure in the energy distribution is contributing to the measured gain.

Finally, if the radiation is propagating as high-order modes of the 1 cm radius vacuum chamber, slippage will be reduced due to the slower-than-c group velocity of such modes.

Chapter 8

Summary

This thesis has documented the operation and performance of a bright, pulsed FIR source of potential value to the scientific community. The source uses single-pass superradiant undulator radiation from sub-picosecond electron bunches. The brightness of this undulator radiation exceeds what is expected from coherent enhacement alone. This can be explained in the 50–70 μm range as mainly due to self-amplification as evidenced by the measured superlinear growth in radiation with undulator length. This is the first such measurement at wavelengths less than 600 μm.

8.1 A Bright Source

For reference, the measured radiation parameters of Table 1.3 are repeated here. As pointed out in Eq. (1.3), these parameters correspond to a peak brightness 10–12 orders of magnitude greater than that of a 2000 K blackbody.

Parameter	Value
Wavelength tunability	45 to 300 μm
Micropulse power	10–40 kW (50–200 μm)
Macropulse power	0.2–1.6 kW (50–200 μm)
Average power	3–50 mW (50–200 μm)
Angular divergence	5–20 mrad (50–200 μm)
Effective source size	3 mm $1/e^2$ radius
Polarization	80 % linear
Micropulse length	26 radiation wavelengths
Micropulse separation	350 ps
Macropulse length	0.7–1.1 μs (50–200 μm)
Macropulse repetition rate	4–30 Hz
Macropulse linewidth	12–20% FWHM

Table 8.1: Parameters of superradiant undulator radiation at SUNSHINE.

8.2 Observation of Self-Amplification

Regardless of the theory, self-amplification has been observed in this experiment, as shown in Fig. 6.6 for example. The self-amplification is correlated with a greater-than-expected superradiant power as calculated from the measured beam parameters, and can be repeatably generated operationally by maximizing the radiated energy normalized by the square of electron beam current.

8.3 Future Prospects: Another Undulator

The immediate extension of this thesis work is the installation of a second undulator, identical to the first, which is already underway. If the trend seen in Fig. 6.6 is maintained, then extrapolation of those fits will give the curves shown in Figs. 8.1, and thus an increase of a factor of 10–100 in the FIR power. A peak power of the order of 1 MW at 50 μm may be achievable.

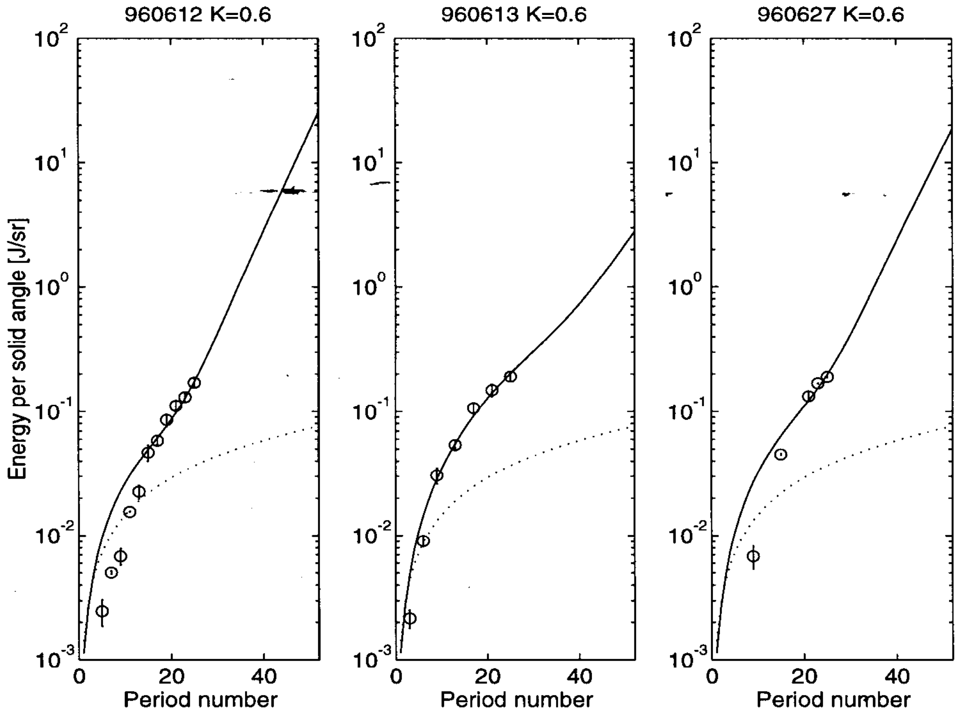

Figure 8.1: Measured energy vs undulator length at $K = 0.6$ and extrapolation to the case of two undulators. The circles are the measurements, the solid line is a theoretical SASE fit, and the dashed lines are calculated superradiant undulator radiation.

Bibliography

[1] Committee on Free Electron Lasers and Other Advanced Coherent Light Sources. *Free Electron Lasers and Other Advanced Sources of Light.* National Academy Press, Washington, D.C., 1994.

[2] H. Motz. Applications of the radiation from fast electron beams. *Journal of Applied Physics*, 22(5):527–535, 1951.

[3] P. Kung, D. Bocek, H.-C. Lihn, and H. Wiedemann. Generation and measurement of 50-fs (rms) electron pulses. *Physical Review Letters*, 73(7):967–970, 1994.

[4] T. J. Orzechowski et al. Microwave radiation from a high-gain free-electron laser amplifier. *Physical Review Letters*, 54(9):889–892, 1985.

[5] D. A. Kirkpatrick et al. A millimeter and submillimeter wavelength free-electron laser. *Physics of Fluids B*, 1(7):1511–1518, 1989.

[6] A. E. Siegman. *Lasers.* University Science Books, Mill Valley, California, 1986.

[7] G. W. Chantry. *Long-wave Optics.* Academic Press, London, 1984.

[8] G. Ramian. The new UCSB free-electron lasers. *Nuclear Instruments and Methods in Physics Research*, A318:225–229, 1992.

[9] K. Berryman and T.I. Smith. First lasing, capabilities, and flexibilty of FIREFLY. *Nuclear Instruments and Methods in Physics Research*, A375:6–9, 1996.

[10] D. Oepts, A. F. G. van der Meer, and P. W. van Amersfoort. The free-electron-laser user facility FELIX. *Infrared Physics and Technology*, 36(1):297–308, 1995.

[11] R. Bonifacio, C. Pelligrini, and L.M. Narducci. *Optics Communications*, 50:373, 1984.

[12] J. D. Jackson. *Classical Electrodynamics.* John Wiley and Sons, New York, 1975.

[13] D.F. Alferov, Yu. A. Bashmakov, and E.G. Bessonov. *Transl. Sov. Phys. Tech. Phys.*, 18:1336, 1974.

[14] S. Krinsky. Undulator for the 700 MeV VUV-ring. *Nuclear Instruments and Methods*, 172:73–76, 1980.

[15] A. Hofmann. Theory of synchrotron radiation. SSRL ACD-note 38, Stanford Synchrotron Radiation Laboratory, 1986.

[16] R. P. Feynman. *Lectures on Physics*, volume 1. Addison-Wesley, 1963.

[17] W. M. Lavender. Observation and analysis of x-ray undulator radiation from PEP. SSRL Report 89/02, Stanford Synchrotron Radiation Laboratory, 1989.

[18] W. M. Lavender. `polarization.c` and `g_k_dphi.c` programs. Unix-compilable C code, 1989.

[19] D. Vaughan et al. *X-Ray Data Booklet.* Lawrence Berkeley Laboratory, Berkeley, California, 1986.

[20] J. S. Nodvick and D. S. Saxon. *Physical Review*, 96:180, 1954.

[21] I. S. Gradshteyn and I. M. Ryzhik. *Tables of Integrals, Series, and Products.* Academic Press, New York, 1965.

[22] H.-C. Lihn. *Stimulated Coherent Transition Radiation.* PhD thesis, Stanford University, 1996.

[23] J. B. Murphy and C. Pellegrini. *Laser Handbook Volume 6*, chapter 2. North-Holland, Amsterdam, 1990.

[24] N.M. Kroll and W.A. McMullin. *Physical Review A*, 17:300, 1978.

[25] A. Gover and Z. Livni. *Optics Communications*, 26:375, 1978.

[26] I.B. Bernstein and J.L. Hirshfeld. *Physical Review A*, 20:1661, 1979.

[27] P. Sprangle, C.M. Tang, and W.M. Manheimer. *Physical Review A*, 21:302, 1980.

[28] C.C. Shih and A. Yariv. *IEEE Journal of Quantum Electronics*, QE-17:1387, 1981.

[29] G. Dattoli, A. Marino, A. Renieri, and F. Romanelli. *IEEE Journal of Quantum Electronics*, QE-17:1371, 1981.

[30] S. Krinsky. Intoduction to the theory of free electron lasers. In *AIP Conference Proceedings*, number 153, pages 1015–1043, 1985.

[31] K.-J. Kim. An analysis of self-amplified spontaneous emission. *Nuclear Instruments and Methods in Physics Research*, A250:396–403, 1986.

[32] E. T. Scharlemann. *Laser Handbook Volume 6*, chapter 9. North-Holland, Amsterdam, 1990.

[33] H. P. Freund and T. M. Antonsen. *Principles of Free-electron Lasers.* Chapman and Hall, New York, 1992.

[34] R. Bonifacio, C. Pelligrini, and L.M. Narducci. Slippage and superradiance in the high-gain FEL: Linear theory. *Optics Communications*, 68:369–374, 1988.

[35] R. Bonifacio, F. Casagrande, G. Cerchioni, L. De Salvo Souza, and P. Pierini. *High Gain, High Power Free Electron Lasers*, pages 35–94. Elsevier Science Publishers, 1989.

[36] M. Borland. A high-brightness thermionic microwave electron gun. SLAC Report 402, Stanford Linear Accelerator Center, 1991.

[37] P. Kung. *Generation and Characterization of Sub-picosecond Electron Bunches.* PhD thesis, Stanford University, 1996.

[38] H. Wiedemann, P. Kung, and H.-C. Lihn. *Nuclear Instruments and Methods in Physics Research*, A319:1, 1992.

[39] P. Kung, D. Bocek, H.-C. Lihn, and H. Wiedemann. High-intensity coherent FIR radiation from sub-picosecond electron bunches. In *Gas, Metal Vapor, and Free-Electron Lasers and Applications*, number 2118, page 191. SPIE, 1994.

[40] R. B. Neal et al. *The Stanford Two-mile Accelerator.* W. A. Benjamin, New York, 1968.

[41] K. Halbach. Physical and optical properties of rare earth cobalt magnets. *Nuclear Instruments and Methods in Physics Research*, 187:109–117, 1981.

[42] H.-C. Lihn, D. Bocek, P. Kung, C. Settakorn, and H. Wiedemann. Measurement of subpicosecond electron pulses. *Physical Review E*, 53(6):6413–6418, 1996.

[43] G. W. Chantry. *Submillimetre Spectroscopy.* Academic Press, New York, 1971.

[44] H.-C. Lihn, D. Bocek, M. Hernandez, P. Kung, C. Settakorn, and H. Wiedemann. Observation of stimulated transition radiation. *Physical Review Letters*, 76(22):4163–4166, 1996.

[45] D. Bocek, P. Kung, H.-C. Lihn, C. Settakorn, and H. Wiedemann. Observation of SASE at 47μm. *Nuclear Instruments and Methods in Physics Research*, A375:13–16, 1996.

[46] L.H. Yu. personal communication.

[47] L. S. Rothman et al. The HITRAN molecular database: editions of 1991 and 1992. *Journal of Quantitative Spectroscopy and Radiative Transfer*, 48:496–507, Nov.-Dec. 1992.

[48] Ontar Corporation. *USF HITRAN-PC Version 2.41.* 9 Village Way North Andover MA 01845.

[49] D. Bocek, M. Hernandez, H.-C. Lihn, P. Kung, C. Settakorn, and H. Wiedemann. Observation of coherent undulator radiation from sub-picosecond electron pulses. In *AIP Conference Proceedings*, number 367, pages 381–390, 1995.

[50] E. H. Haselhoff. Free-electron-laser model without the slowly-varying-envelope approximation. *Physical Review E*, 49(1):R47–R50, 1994.